Dynamic Simulation of Marine Risers with Vortex Induced Vibration

by

Ryan Stuart Nicoll
B.Eng in Mechanical Engineering, University of Victoria, 2004

A Thesis Submitted in Partial Fulfillment of the
Requirements for the Degree of
MASTER OF APPLIED SCIENCE
in the
Department of Mechanical Engineering.

Dynamic Simulation of Marine Risers with Vortex Induced Vibration

by

Ryan Stuart Nicoll
B.Eng in Mechanical Engineering, University of Victoria, 2004

Supervisory Committee

Dr. Bradley J. Buckham, Supervisor (Dept. of Mechanical Engineering, University of Victoria)

Dr. Afzal Suleman, Supervisor (Dept. of Mechanical Engineering, University of Victoria)

Dr. Peter Oshkai, Departmental Member (Dept. of Mechanical Engineering, University of Victoria)

Dr. Richard Dewey, External Examiner

Supervisory Committee

Dr. Bradley J. Buckham, Supervisor (Dept. of Mechanical Engineering, University of Victoria)

Dr. Afzal Suleman, Supervisor (Dept. of Mechanical Engineering, University of Victoria)

Dr. Peter Oshkai, Departmental Member (Dept. of Mechanical Engineering, University of Victoria)

Dr. Richard Dewey, External Examiner

Abstract

The purpose of the work described here is to analyse vortex induced vibration (VIV) effects on marine risers and unorthodox forms of suppression of this phenomenon, which can cause structural failure through metal fatigue. Two suppression methods are explored: flex joints and buoyancy modules. Flex joints, which act like a hinge at a point on the riser due to the large reduction in bending stiffness, can suppress higher modes of vibration from propagating along or appearing in the riser. Buoyancy modules, with their local 100% increase in riser diameter, can decorrelate vortex shedding along the span of the riser and reduce the resonant effect of VIV.

The numerical finite element cable model and rigid body model developed at the University of Victoria were modified and used as a foundation for the research. The modifications include an algorithm to estimate the forces due to ocean surface interaction with rigid bodies and a model to produce the appropriate VIV response in the numerical cable model. The resulting VIV model was calibrated and validated

with analytical, experimental, and numerical data available in the literature. In general, the model produces qualitative effects of VIV, including its self-starting and self-limiting nature, frequency lock-in, multi-mode response, and limited structural response on the order of one diameter.

A simulation of a testbed riser in a variety of ocean currents was generated to observe the effects of installing flex joints and buoyancy modules at various locations along the riser span. The performance of the testbed riser was gauged by comparing the time series of von Mises stress and the associated safety factor, n_s, from fatigue failure at many points along the span to an unmodified testbed riser.

The stress fluctuation was drastically reduced within the flex joints for all water currents studied, which greatly increases fatigue performance. Flex joints placed at the top of the testbed riser had less impact, as the stresses are dominated by the large and unavoidable tensions found there. Flex joints placed in the bottom region of the riser did not affect the n_s of the remaining riser span until very high modes of vibration were present. At these higher modes, some testbed riser configurations changed their vibration envelope and frequency, which indicates that a possible alternate and less damaging mode of vibration was induced. Flex joints therefore act effectively as a local patch against poor fatigue performance and placement of several flex joints does not negatively impact the behaviour of the rest of the riser in the cases examined. However, the explicit relationship between placement and spacing of flex joints with environment conditions remains unknown.

Buoyancy modules introduced spatial fluctuations in the entire n_s profile of the testbed riser, unlike flex joints. In addition, the buoyancy modules decreased n_s performance due to the hydrodynamic load concentrations induced by their large diameters. However, the 16% coverage case increased n_s elsewhere along the riser, though the 10% covered riser did not match this performance. Since in both cases the modules were evenly spaced along the riser, performance benefits from increased coverage implies a minimum coverage of 16% needed for significant improvement in

fatigue performance for devices of this type. This coverage requirement may apply to traditional VIV suppression devices such as helical strakes, since they decorrelate vortex shedding along the span of the riser albeit in a different manner than buoyancy modules. Finally, the buoyancy modules changed the stress oscillation frequency more than the flex joint cases from the unmodified riser. This is desirable since lowering the frequency of oscillation also increases the fatigue performance of the riser.

Table of Contents

List of Tables

List of Figures

Nomenclature

Re	Reynolds number
St	Strouhal number
E	Young's modulus $[\frac{N}{m^2}]$
I	riser area moment of inertia $[m^4]$
A	riser load-bearing cross-section area $[m^2]$
EI	flexural rigidity $[Nm^2]$
EA	axial rigidity $[N]$
GJ	torsional rigidity $[Nm^2]$
D	diameter of riser $[m]$
C_d	drag coefficient
C_{d0}	drag coefficient for static structure
L	total riser length $[m]$
L_u^i	element length $[m]$
T	riser tension $[N]$
N_i	cycles until fatigue failure induced by ocean current profile i
n_i	cycles loaded by ocean current profile i in lifetime of riser
S_u	ultimate material strength $[Pa]$
S'_u	modified ultimate material strength $[Pa]$
S_f	fatigue stress load $[Pa]$
S_l	low cycle stress limit $[Pa]$
S_e	high cycle stress limit $[Pa]$
a_s	fatigue life constant $[Pa]$
b_s	fatigue life constant
k_f	surface finish factor
k_s	size factor
k_r	reliability factor
κ	magnitude of riser curvature $[m^{-1}]$
$\hat{t}$	Frenet frame tangential unit vector
$\hat{n}$	Frenet frame normal unit vector
$\hat{b}$	Frenet frame binormal unit vector

$\hat{p_1}$	Riser local frame principal unit vector
$\hat{p_2}$	Riser local frame principal unit vector
$\hat{q}$	Riser local frame tangential unit vector
γ	Frenet frame geometric twist $[rad]$
α	Angle of twist between Frenet and local riser frame $[rad]$
α'	Spatial rate of change of twist angle α $[\frac{rad}{m}]$
$\mathbf{T}_{IH}$	transformation matrix from riser hydrodynamic frame to the inertial frame
$\mathbf{T}$	Spatial transformation matrix from body frame to inertial frame
$\mathbf{T}_1$	transformation matrix for any vector in rigid body frame to the inertial frame
$\mathbf{T}_2$	transformation matrix for Euler angles in rigid body frame to the inertial frame
ν	seawater kinematic viscosity $[\frac{m^2}{s}]$
ρ_w	water density $[\frac{kg}{m^3}]$
ρ_r	riser average density $[\frac{kg}{m^3}]$
ζ	sea surface height $[m]$
ω_w	ocean wave cyclical frequency $[\frac{rad}{s}]$
ω_s	vortex shedding frequency $[\frac{rad}{s}]$
$\boldsymbol{X}$	set of rigid body position and Euler angle orientation values
$\boldsymbol{X}_b$	set of rigid body velocity values expressed in terms of the body reference frame
u	rigid body velocity x-direction velocity $[\frac{m}{s}]$
v	rigid body velocity y-direction velocity $[\frac{m}{s}]$
w	rigid body velocity z-direction velocity $[\frac{m}{s}]$
p	rigid body velocity x-direction angular velocity $[\frac{rad}{s}]$
q	rigid body velocity y-direction angular velocity $[\frac{rad}{s}]$
r	rigid body velocity z-direction angular velocity $[\frac{rad}{s}]$
$\mathbf{M}$	rigid body mass matrix
m	rigid body mass
I_x, I_y, I_z	rigid body mass moment of inertia values $[kgm^2]$
I_{xy}, I_{yz}, I_{zx}	rigid body products of inertia $[kgm^2]$
$\mathbf{M}_A$	rigid body added mass matrix
$\boldsymbol{F}_B$	buoyancy vector $[N]$
$\boldsymbol{F}_D$	hydrodynamic drag vector $[N]$
$\boldsymbol{F}_C$	cable force $[N]$

H	ocean water wave height $[m]$
k	ocean water wave x-component wave number $[m^{-1}]$
l	ocean water wave y-component wave number $[m^{-1}]$
K_w	ocean water wave vector magnitude $[m^{-1}]$
ROV	Remotely Operated Vehicle
DNS	Direct Numerical Simulation
VIV	Vortex Induced Vibration
DOF	Degree of Freedom
DVM	Discrete Vortex Method

Acknowledgements

This thesis could not have been completed without the contributions of many others. Thanks first to my family for their generosity, love, and support. More specifically, my mom, dad and uncle, who took care early on in my life to instil the value of education and the virtue of hard work. To Brad and Afzal, thanks for providing this opportunity to learn and make a meaningful contribution to the University. To my fellow grad students and particularly my office mate Julio, thanks for the thoughtful discussions and feedback on the many problems I came across. Thanks to all my friends for all the good times we had while I tried to forget about research for a little while. Finally, thanks to Sara for your unconditional love and support. Your smile brings sunshine on the cloudiest day!

to my family

Chapter 1

Introduction

The fast pace and high social standards of developed nations have been established through the excessive consumption of energy, whether renewable or non-renewable [1]. As conventional energy supplies are drained, new technologies must be developed that allow us to process alternative sources, or access conventional sources in remote hostile locations. The complexity of these technologies and the uncertainties that surround their operation make it extremely expensive to develop them through field trials. Reliable design of complex dynamic systems is therefore in large part impossible without some degree of numerical analysis. While numerical models always require experimental validation, one important advantage is their economy: any number of virtual prototypes can be designed and analysed without fabricating physical objects. Examples are the numerical tools that have allowed oil, gas, and precious metal extraction to expand into harsh offshore regions in deep waters in the last half century. As the depth of operation increases, so does the need to understand and predict the mechanical system behaviour in order to ensure a reliable design. A crucial component to submerged resource extraction is the marine riser. General riser design considerations include stability of the surface platform, static strength considerations, and dynamic response to surface waves, ocean currents and vortex shedding. It

is the dynamic modelling that is the most challenging because the results of each dynamic effect can not necessarily be analysed separately and then superimposed to reconstitute the overall solution. Rather, a model of the entire system must be formulated to glean realistic and extensive knowledge on the coupling between the system degrees of freedom and the overall system motions that result.

1.1 Deep Water Resource Extraction

In the last 50 years, offshore resource extraction has encroached on deeper regions in the ocean. For instance, 1963 saw seabed penetrations occur as deep as 193 meters. By 1984 this had increased to 2120 meters [2]. An approximate relationship of depths reached from 1949 to the present is given by [3]:

$$depth \approx \frac{1}{540} N_y^{3.5} \tag{1.1}$$

for depth in meters after the number of years N_y after 1949. Equation (1.1) illustrates the accelerating expansion of marine resource extraction and it suggests risers at an average ocean depth of about 3700 m around the year 2013 [4]. Typical structures necessary for deep water resource extraction include a semisubmersible platform and resource transport barge, which are connected by risers to the wellheads below (see Figure 1.1, adapted from [5]).

A riser is merely a tube that is used to deliver slurry, including solids, fluids, gasses and mixtures of these materials, from the depths of the ocean and is also used as a physical conduit to transmit power to the drill bits used to breach the ocean bottom. As Figure 1.1 implies, risers can be attached to a barge directly, and a more detailed view can be seen in Figure 1.2 (adapted from [2]). Figure 1.2 showcases a rotatable turret on the barge, which helps alleviate any twist on the riser induced by barge motion.

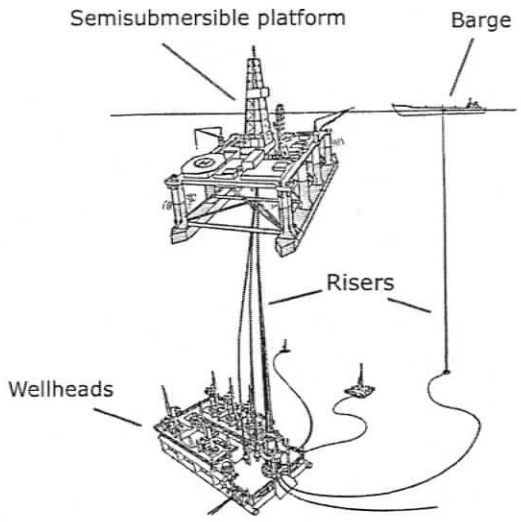

Figure 1.1: Deep water resource extraction [5]

Risers that reach depths of 2000 m easily reach aspect ratios $\frac{L}{D}$ on the order of 6000. Assuming an average human hair diameter of 99 μm [6], over 0.5 m length of hair is needed to match this aspect ratio. Due to the large exposed areas of structures like the semisubmersible platforms like in Figure 1.1 and high aspect ratio risers, it follows that the dominant disturbance forces will be hydrodynamic. A hydrodynamic phenomenon of great concern to design engineers is called vortex induced vibration (VIV).

1.2 Vortex Induced Vibration

When immersed blunt bodies move relative to a fluid, it is common to observe asymmetrically shed vortices in the wake. This phenomenon is observed in a wide range of fluids and length scales, with two examples seen in Figure 1.3.

The direction of relative velocity (the same direction the vortices convect) is referred to as the in-line direction, and the direction perpendicular to in-line is referred to as the cross-flow direction. The asymmetric periodic nature of the wake causes an

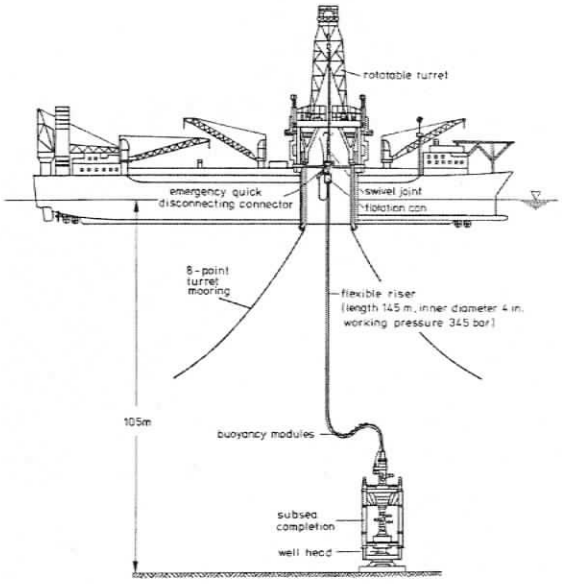

Figure 1.2: Deep water mining barge [2]

oscillating pressure field around the structure and can induce vibrations in both the cross-flow and in-line directions. This phenomenon can be observed in such structures like bridge cables and electrical lines in the atmosphere and oil and gas pipelines and risers in marine environments. As with most flow induced phenomena, this vortex shedding regime is characterised by the nondimensional Reynolds number Re:

$$Re = \frac{V_{rel} D}{\nu} \tag{1.2}$$

where D is the structure characteristic dimension, V_{rel} is the relative velocity of the structure with respect to the fluid, ν is the fluid kinematic viscosity, which is assumed to be constant at 1.8e-6 $\frac{m^2}{s}$ (the value at 0^oC). Vortex shedding regimes of circular cylinders of diameter D as a function of Re can be seen in Figure 1.4. The subcritical range $300 \leq Re \leq 3x10^5$ is studied in this work, which is the range in which many ocean risers operate. Figure 1.5 shows the Reynolds number for a variety of practical riser diameters and ocean currents and it is clearly illustrated that the

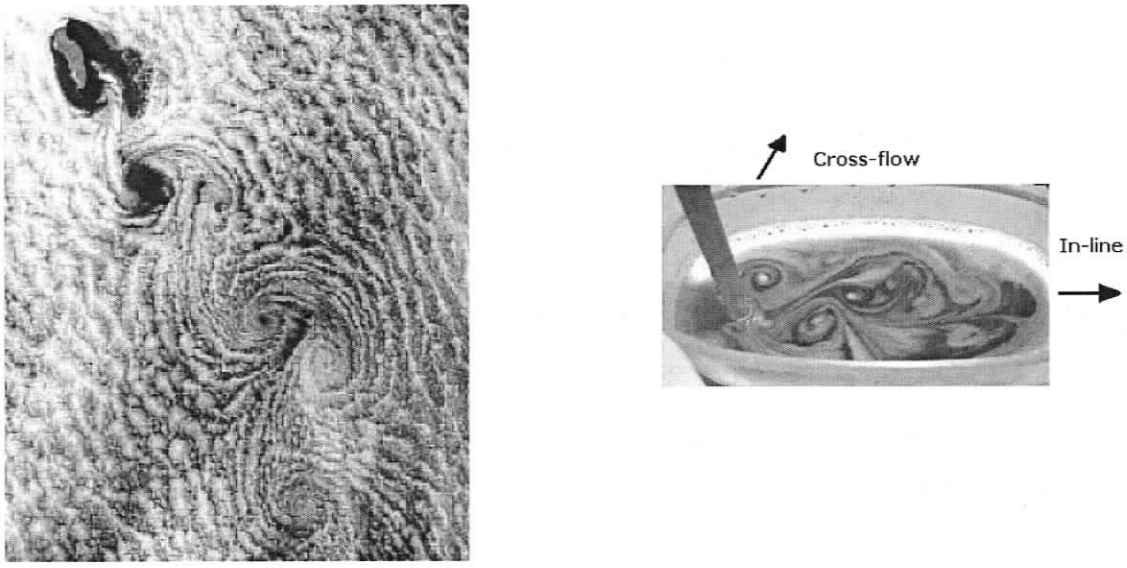

(a) (b)

Figure 1.3: Vortex shedding in (a) the atmosphere [7] and (b) water

subcritical region and hence vortex shedding is very difficult to avoid. The vortex shedding behaviour is further characterised by the dimensionless Strouhal number, which is approximately 0.2 in this subcritical range of Reynolds numbers [9, 10] (see Figure 1.6, from [9]):

$$S_t = \frac{f_s D}{V_{rel}} \tag{1.3}$$

where S_t is the Strouhal number and f_s is the vortex shedding frequency of a stationary blunt body. Since S_t is relatively constant in the subcritical region [9], equation (1.3) can be re-written in terms of the vortex shedding frequency:

$$f_s = 0.2\frac{V_{rel}}{D} \tag{1.4}$$

Equation (1.4) shows the shedding frequency should increase linearly with the

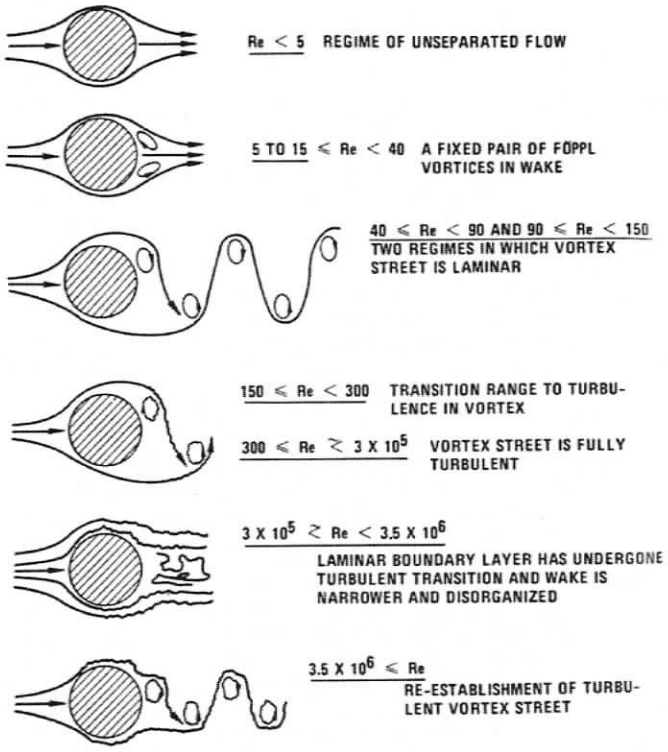

Figure 1.4: Vortex shedding regimes of smooth cylinders [8]

relative velocity V_{rel}. Another dimensionless parameter used to help characterise the response of the structure is the reduced velocity, V_r:

$$V_r = \frac{V_{rel}}{f_{ex} D} \tag{1.5}$$

where f_{ex} is the vibration frequency of the structure. Sometimes in the literature the first natural frequency of the structure, f_n, is used in place of f_{ex} to complete the nondimensional group V_r. In this work the excitation frequency is used because of the existence of many natural frequencies in the riser and the choice of which frequency to use is ambiguous. When the vortex shedding frequency nears one of the structure natural frequencies a resonant vibration develops. The vortex shedding frequency f_s and structure vibration frequency f_{ex} then reach a common vibration frequency, which is referred to as lock-in. Lock-in occurs because the structure motion feeds back

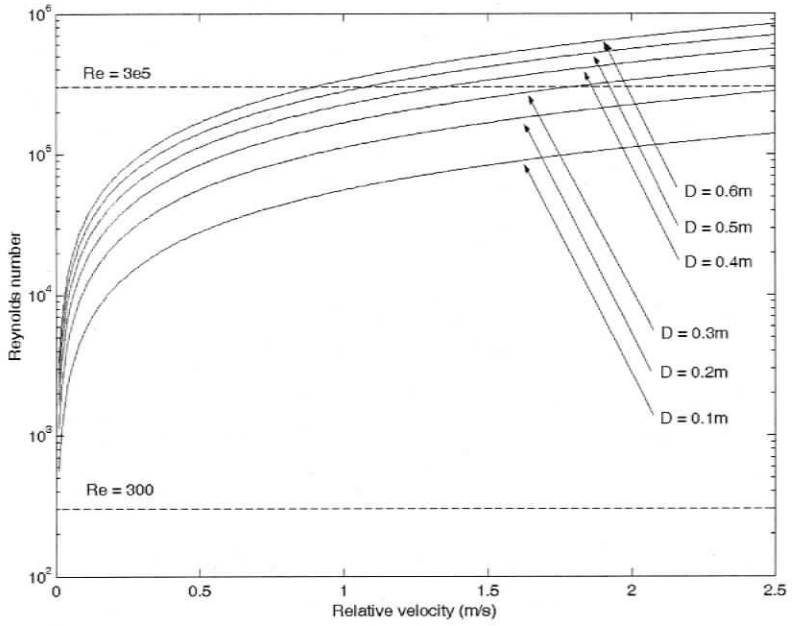

Figure 1.5: Reynolds number sensitivity for various riser diameters. The subcritical Reynolds number limits of 300 and 3e5 are shown in dashed lines. For a practical range of riser diameters and water velocities, the Reynolds number remains largely in the subcritical region, which shows that vortex shedding is difficult to avoid.

into the flow field which influences the shedding frequency. During lock-in, the vortex shedding frequency deviates from equation 1.4. Figure 1.7 illustrates this with the results of a classic 1-degree of freedom (DOF) experiment. An elastically supported rigid circular cylinder with natural frequency f_n was stimulated with fluid flow at V_{rel}. This classic experiment helped form the foundation for several nondimensional groups used to study VIV, including the reduced velocity, V_r, mentioned previously.

The top of Figure 1.7 shows the ratio of the vortex shedding frequency to the structure's first natural frequency $\frac{f_s}{f_n}$ as a function of the reduced velocity (defined with the 1 DOF structure's natural frequency). Lock-in is clearly illustrated as the ratio of frequencies maintains unity in the range $5 \leq V_r \leq 6$ after which lock-in is disrupted and the vortex shedding continues to follow the linear vortex shedding relationship described in equation (1.4). The bottom of Figure 1.7 shows the nondi-

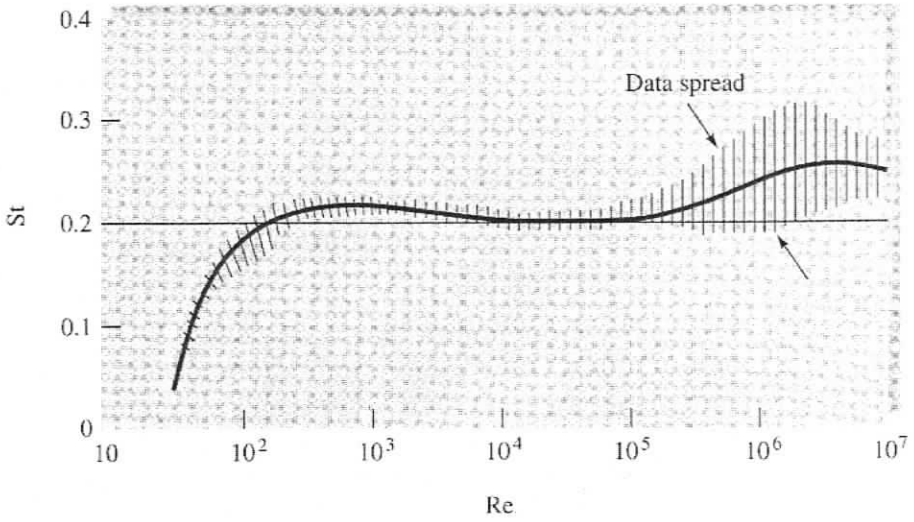

Figure 1.6: Circular cylinder Strouhal number dependence on Reynolds number [9]

mensionalised cylinder response amplitude $\frac{A_y}{D}$ as it reaches a maximum in the middle of the lock-in region.

Even though the vortex shedding frequency can lock-on to the structure natural frequency, structure response is limited and usually reaches a maximum of approximately $1D$ in fluids like water. This self-limiting nature is inherent of VIV since large structure motions disrupt the periodic vortex formation. Structural damping can also help significantly reduce the VIV response and an additional nondimensional parameter, the reduced damping δ_r, is often used to help quantify this:

$$\delta_r = \frac{2m^* (2\pi\zeta)}{\rho D^2} \tag{1.6}$$

where ζ is the equivalent 1 DOF system cross-flow direction structural damping ratio, ρ is fluid density, and m^* is the mass ratio:

$$m^* = \frac{\rho_s}{\rho} \tag{1.7}$$

where ρ_s is the density of the structure. The mass ratio indicates the ratio of the

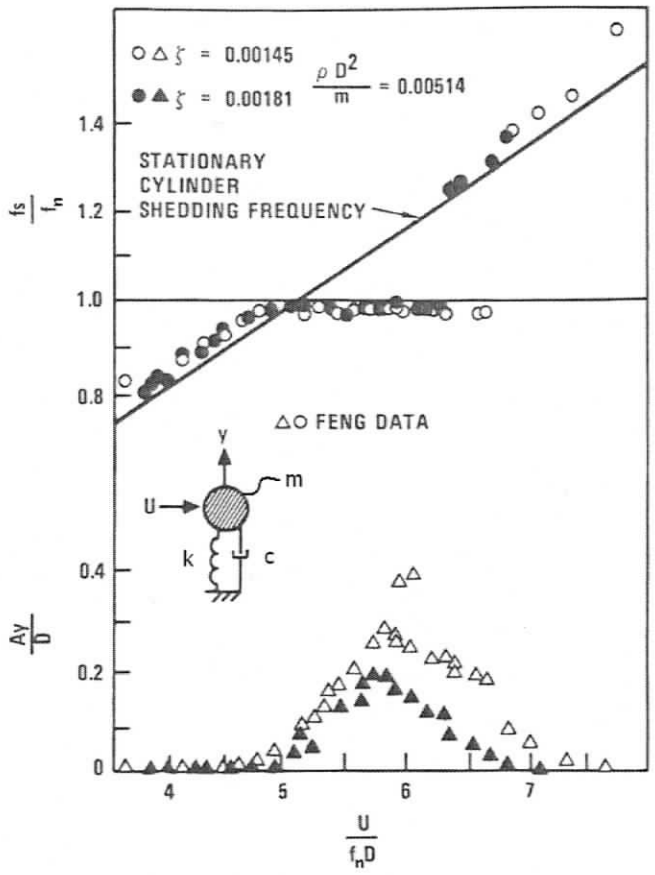

Figure 1.7: Rigid circular cylinder lock-in and response [11, 12]

structure mass to the displaced fluid mass. The reduced damping, δ_r, is also referred to as the response parameter or Scruton number. An alternative to reduced damping, δ_r, is the Skop-Griffin parameter S_G:

$$S_G = \pi^3 S_t^2 \delta_r \tag{1.8}$$

Both parameters serve a similar purpose and were independently established [13]. Both Figures 1.8 and 1.9 shows that as S_G or δ_r increases by increasing either or both the mass ratio, $m*$, and structural damping, ζ, the induced VIV response decreases. When these values decrease, the structural vibration amplitude limit of $1D$ is illustrated. The parameter γ referred to in Figure 1.9 is used to normalize the cross-flow

vibration mode shape which is inherently different for each experiment setup.

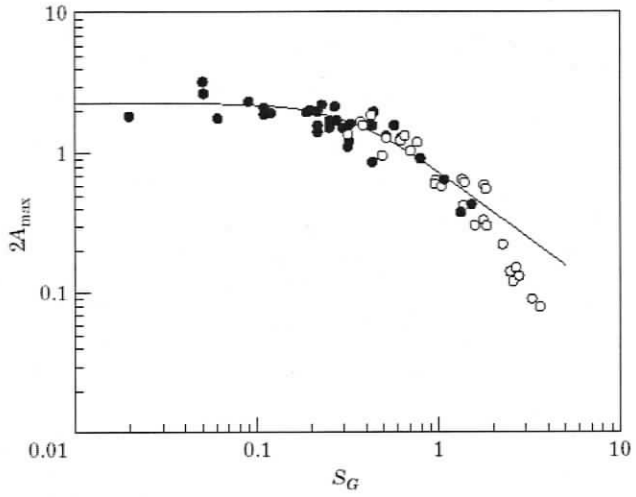

Figure 1.8: Structure response with Skop-Griffin parameter S_G [14]

The lock-in behaviour of VIV is of particular interest in ocean engineering. High aspect ratio risers can behave like taut strings and have an infinite number of natural frequencies for vortex shedding to lock on to. As such, VIV is very difficult to avoid and may not be adequately addressed through a static design analysis. Rather, countermeasures must be introduced to disturb the inevitable vortex shedding. Vortex induced vibration can induce curvature oscillations in the riser in both in-line and cross-flow directions. Of the two the cross-flow behaviour is the most significant due to the higher curvatures and frequencies induced. In addition, the mean cross-flow vibration amplitude has been connected to mean drag coefficient amplifications of over 100% of the nonvibrating structures [15–17]. Vortex induced vibration is a nonlinear fluid-structure interaction problem and it makes modelling and predicting both high and low frequency structure behaviour difficult. As pointed out repeatedly by Sarpkaya in [3], VIV can not be viewed as a high frequency motion superimposed on a bulk low-frequency mean motion.

If the riser vibration persists for extended periods of time, the cycling of bending stresses becomes the dominant concern in the mechanical design process as opposed to

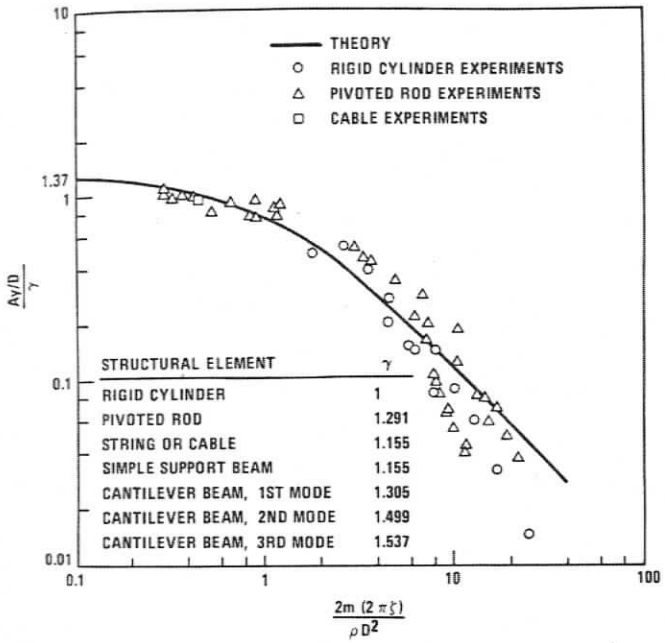

Figure 1.9: Various structure VIV response [12]

the quasi-static tensile stresses that are achieved through riser self-weight and current induced drag. Cyclical stresses can cause failure due to metal fatigue, even though the stress amplitudes are far less than that measured for the static loading. There are several different options available to suppress these damaging vibrations.

1.2.1 VIV Suppression and Mitigation

Vortex induced vibration can be suppressed with active or passive devices. Active VIV suppression devices are characterised from passive ones through the use of instrumentation, actuators, and control algorithms that interact with the structure. One example is riser vibration mode suppression, which is briefly mentioned in [13, 18, 19]. An active system is a significant engineering feat due to the required electrical infrastructure required along the full span of the riser and as a result will not be studied in the work presented.

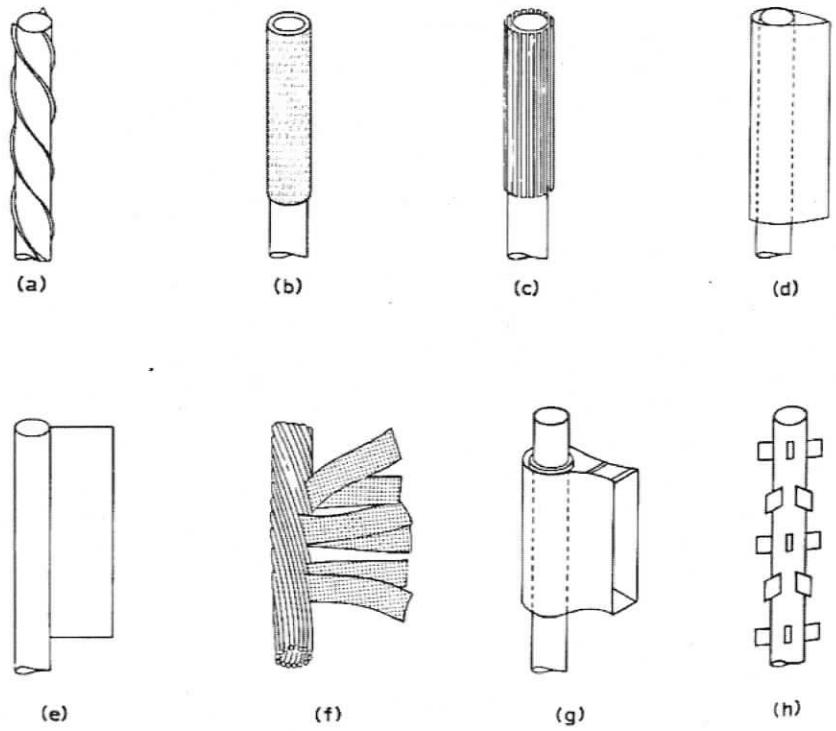

Figure 1.10: Passive VIV suppression devices: (a) helical strake; (b) porous shroud; (c) axial slats; (d) streamlined fairing; (e) flow splitter; (f) ribboned cable; (g) guiding vane; (h) spoiler plates [12]

Typically, VIV is suppressed by using passive devices that disrupt vortex shedding and are fixed to the outside of the riser. Figure 1.10 shows a variety of popular passive VIV suppression devices, many of which are actively being researched, such as the porous shroud discussed in [19]. Another type of passive device is a small (relative to the riser diameter) cylinder placed in the near wake region [20,21], which disrupts the wake of the larger cylinder and significantly attenuates vortex shedding. Such passive devices can require significant coverage of the riser which leads to lengthy installation time and significantly increased drag coefficient due to the geometric profile. An increased drag coefficient causes larger displacement of the riser in the face of ocean currents and increased hydrodynamic loads transmitted to the ship and wellhead. Alternative forms of passive suppression disrupt the properties of the riser structure along its span, which changes the natural frequency and disrupts lock-in over long spans of the riser. These methods include altering the structure tension or bending stiffness, which both contribute to the natural modes of vibration. In addition, some experiments with variable geometry, such as using stepped cylinders [22] or adding buoyancy modules [23] seem to provide favourable VIV suppression by preventing the vortex street from correlating along the span of the riser. In this work, the focus is on disrupting the link between vortex shedding and VIV rather than mitigating the vortex shedding directly. As mentioned in [3]:

> In fact, it may be more advantageous to predict and thereby to avoid the VIVs than to attempt to eliminate them. After all, the fluctuating lift will always be there, with or without VIV, and the pure circular cylinder will always be the preferred shape.

1.2.2 Flex Joints

A flex joint is a region of significantly lowered bending stiffness in the riser. Locally, that is within the flex joint, it is expected the alternating stress levels will be much

lower since flex joints act as a hinge and develop smaller internal bending moments. In addition, it is possible that the presence of these flex joints can provide more favourable modes of vibration in the riser and prevent propagation of lateral vibrations along the riser. For a slender beam with pinned supports under uniform tension T, the natural frequency of mode n is [24] (see derivation in Appendix A):

$$\omega_n = \frac{\pi^2}{l^2}\sqrt{\frac{n^4 EI}{\rho_s A} + \frac{n^2 T l^2}{\pi^2 \rho_s A}} \tag{1.9}$$

where E is Young's modulus or the modulus of elasticity, A is beam cross-section area, T is the constant tension value, ρ_s is beam material density and l is beam length. As tension approaches zero, the natural frequency becomes one of a flexible beam only. With zero flexural rigidity EI, the beam acts like a taut vibrating string under tension T. The mode shape is the distinct pattern the structure assumes during vibration. For the testbed riser system under static conditions, the top and bottom tension values are approximately $1.4e6N$ and $4.8e4N$, respectively. Evaluating equation (1.9) at the top and bottom reveals the approximate nature of the natural frequencies at these locations. The local natural frequencies can be seen in Figures 1.11 and 1.12 as a function of mode number n for the taught string ($EI = 0$), untensioned beam ($T = 0$), and for the tensioned beam. Clearly, the natural frequencies are dominated by the bending stiffness contribution after mode $n = 30$. In addition, equation (1.9) shows that the bending stiffness EI facilitates higher frequencies in the structure over the tension term near the bottom of the riser.

For a tensioned beam with pinned boundaries, the vibration mode shapes are given by:

$$\Phi(z) = \sin\left(\frac{nz\pi}{L}\right) \tag{1.10}$$

Equation (1.10) shows that higher modes (increasing n) will induce a more sinuous

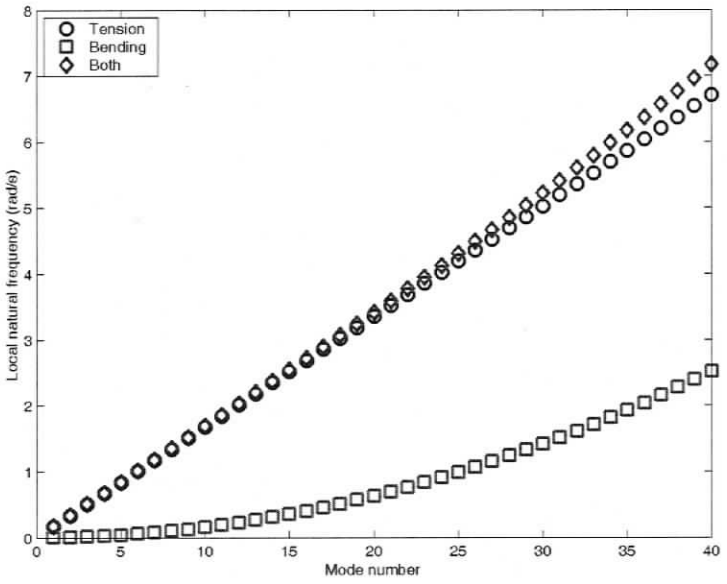

Figure 1.11: Local natural frequency properties at the riser top

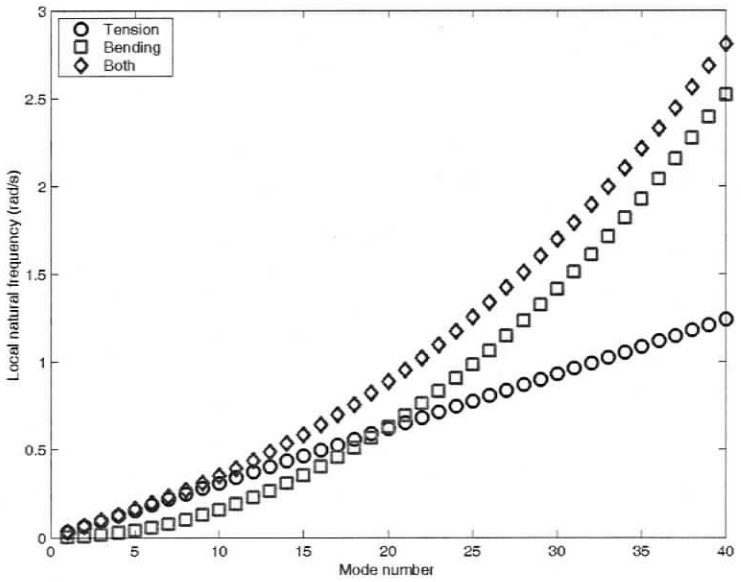

Figure 1.12: Local natural frequency properties at the riser bottom

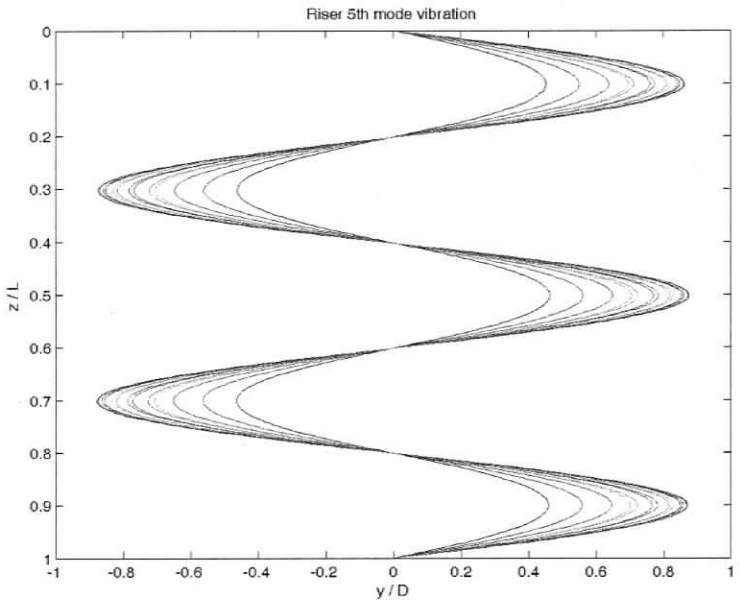

Figure 1.13: Riser vibrating in the fifth mode ($n = 5$). The vertical axis shows the distance along the riser nondimensionalised to the riser length L. Each line in the plot represents a sequential snapshot of the riser at a constant time interval.

shape and therefore larger curvatures. Snapshots of a simulated riser vibrating in the fifth mode can be seen in Figure 1.13. The vibration envelope, seen in 1.14 is the corresponding space swept out by the riser.

The introduction of flex joints may not have an effect near the top of the riser, where tension-dominated vibrations will take place. However flexural-dominated and high frequency vibrations could be mitigated with the use of flex joints near the bottom of a riser where the tension is significantly less and contributes less to the natural frequency given by equation (1.9). Higher modes of vibration can potentially incur more damage than lower modes for two reasons. Higher modes vibrate at higher frequencies – more damage is accumulated in a shorter time period. Also, higher modes of vibration mean larger curvatures are present in the structure – and higher curvatures mean larger internal bending moments and stresses. Since the testbed riser involves a large tension gradient, torsion, and complex distributed hydrodynamic

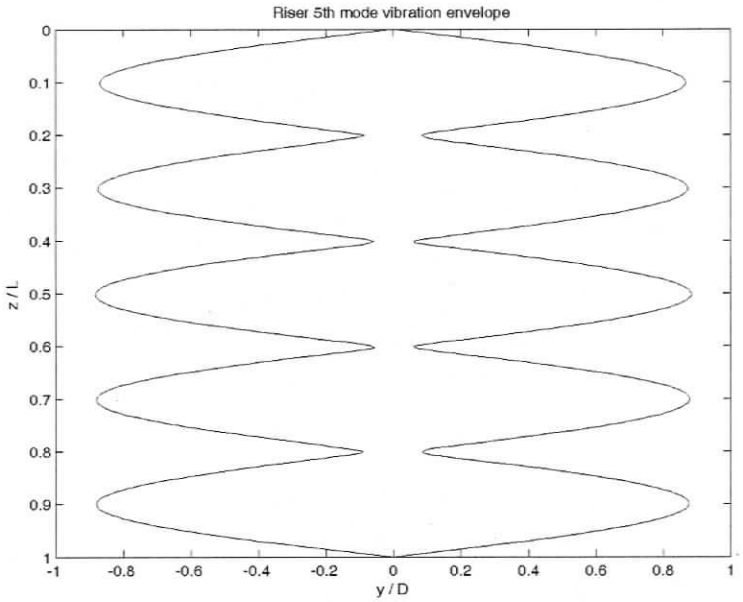

Figure 1.14: Vibration envelope of riser vibrating in the fifth mode ($n = 5$)

loadings, equation (1.9) only gives clues as to how the real system might behave. In addition, experiments in the literature do not have significantly varying tension along the riser and usually only use a unidirectional flow pattern. In order to further investigate the structural behaviour, a numerical VIV model is needed.

1.2.3 Modelling and Predicting VIV

Vortex induced vibration is a heavily researched problem and several important reviews of the research can be found in the literature [10, 13, 18, 25, 26]. Early research in the literature shows the development of simple numerical VIV models developed by the study of 1 DOF rigid cylinder experimental VIV (cross-flow) response. These 1 DOF experiments, which include results seen in Figure 1.7, also influenced nondimensional parameters used to study the phenomenon such as the reduced damping, δ_r. In the last decade, research has focused on flexible cylinder VIV response and various numerical models have been developed (see, for example, [27–29]).

There are several ways to model this phenomenon and the methods traverse a wide range of computational complexity and expense. The simplest models, usually referred to as wake oscillators, use an additional nonlinear differential equation to oscillate the lift coefficient of the structure. This then induces an oscillating lift force which results in an appropriate structural response. Generally, the steady state VIV produced by wake oscillators matches experiment results well, though transient effects (for example, initiation of VIV) are not guaranteed to be accurate. A more complicated VIV modelling method, referred to as vortex tracking or the discrete vortex method (DVM), establishes boundary layer separation points on the structure and evaluates the lift forces due to changing vorticity. The most complicated methods include full direct numerical simulation (DNS) of the fluid induced pressure field about the structure. Due to the large Reynolds number range for risers in an ocean environment and large aspect ratios, DNS is usually prohibitively computationally expensive, even when the calculations are confined to 2D slices of flow at discrete sections along the structure, although numerical experiments have been completed [16]. These methods can be either based in the time domain or the frequency domain and several prominent academic and commercial models are in continual development (see, for example, [27–29]). It should be noted that wake oscillators and DNS simulations have produced results of similar accuracy despite the drastically different modelling methods [17, 30]. Recent efforts in the study of VIV focus more on the dynamics of more complex slender structures like risers [31–34]. Because of computational economy for use in simulation based design and its overall simplicity, the wake oscillator was selected for use in this work.

1.3 Deep Sea Mining Problem Description

A deep water mining system can be seen in Figure 1.15. A robotic excavator located at the bottom extracts material and minerals from the sea floor and sends it along

a flexible connector hose. A dump valve, which serves as an interface between the riser and the connector hose, can be used to eject excess material back to the ocean floor. The riser then transports the slurry up to a surface vessel for storage and processing. Cellula Robotics, an engineering consulting company based in Vancouver, approached the University of Victoria to study the effects of flex joints in the riser as initial calculations had suggested flex joints could increase the fatigue life of the riser. The general dimensions of the testbed riser were fixed in order to facilitate the study of the structure and limit design variables. The structure parameters are provided in Appendix E.3 and summarised in Table 1.1. A description of the system model, and the assumptions applied, can be found in section 4.1.

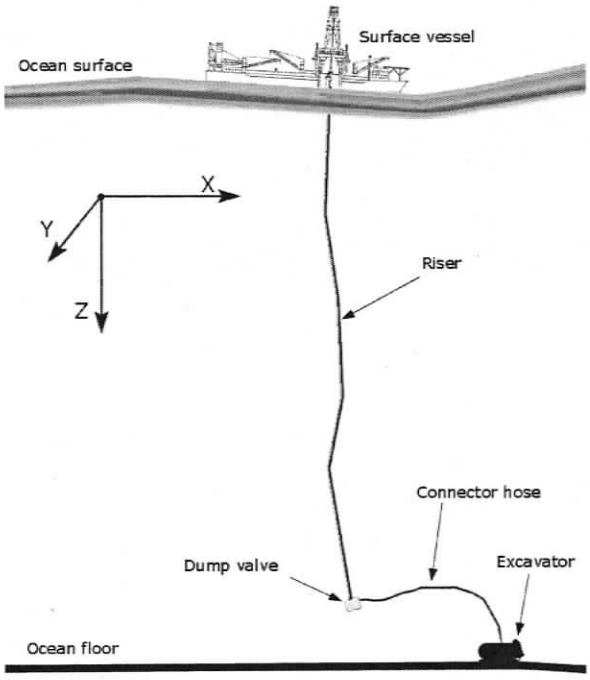

Figure 1.15: Deep water mining system. The excavator extracts material and minerals from the sea floor, which are transported up the connector hose, riser, and then to the surface vessel for storage, processing, and transport. The dump valve at the bottom of the riser serves to eject excess material back to the ocean floor.

Table 1.1: Structural values for testbed riser

Parameter	Value
Riser average density ρ_r	$1843\frac{kg}{m^3}$
Riser outer diameter D	$0.3302m$
Riser length L	$1600m$
Riser drag coefficient C_d	1.2
Riser axial stiffness	$2.53e9N$
Riser bending stiffness	$3.20e7Nm^2$
Riser torsional stiffness	$2.56e7Nm^2$
Barge length	$152m$
Barge width	$30.5m$
Barge height	$11.6m$
Barge operational mass	$29,000,000kg$
Dump valve mass	$9000kg$
Dump valve radius	$0.5m$
Water velocity	$0.1\frac{m}{s}$
Water profile	uniform

1.4 Objectives

The main objective of this research is to investigate the utility of manipulating the structural properties of the testbed riser to mitigate VIV effects. Additional objectives include showing the validity of the wake oscillator approach in a finite element riser structure, tuning and validating the formulation against published experimental data to yield a useful tool in riser design, adding kinematic calculations that allow the wake oscillator model to adapt to changing riser orientation or current profiles, and modelling the surface vessel to incorporate its effects on the riser.

Flex joints are introduced in various locations along the span of the riser. In addition to reducing fatigue effects at the location of placement, the flex joints may alter the mode of vibration of the riser and either disturb higher modes of vibration or trip lower modes of vibration with smaller curvatures. In addition, the use of buoyancy modules is explored, following developments in [22, 23]. Introducing significant diameter variations along the span of the riser prevents the vortex shedding to occur at a single frequency and so the structure response may be attenuated. These alternative

mitigation techniques offer some advantages over traditional suppression techniques: they could potentially consume less time to install and they also do not necessarily incur a large hydrodynamic drag penalty as they are only employed intermittently over the riser span.

In order to model the riser system, an existing simulation developed at the University of Victoria is modified and enhanced. This simulator has been used to analyse variable tension cables and rods [35–38] during operation of towed or remotely operated vehicles. Since DNS methods are too numerically intense to implement in a near realtime simulator [3, 16] a wake oscillator is used to model the VIV effects. The new VIV simulator is validated against experimental data to provide some assurance that the testbed riser simulation results are realistic. In addition, a local cross-flow coordinate direction is established in the simulator to establish an equivalent cross-flow deflection amplitude. This allows the simulator to be used as a more general tool for riser systems or towed vehicles for which the cross-flow direction is unknown a priori.

The surface vessel dynamics are modelled by evaluating the variable buoyancy of the ship. In this manner, dynamically controlled boundary conditions are used on the riser instead of a prescribed kinematic motion.

1.5 Overview

Chapter 2 introduces detail on metal fatigue theory and the theory that drives the key simulation components. The kinematic calculations used in modelling the system dynamics are presented in section 2.2. The rigid body and the variable buoyancy algorithm model used to model the surface vessel and dump valve is described in section 2.3.1. In section 2.3.2 the finite element riser model is introduced in addition to the discretisation of the hydrodynamic loads. The VIV modelling equations, which includes the wake oscillator governing equation, is revealed in section 2.3.3. Chapter 3 presents validation and calibration efforts. Specifically, validation and convergence

results of the variable buoyancy model can be seen in section 3.1 and validation of the VIV simulator are seen in 3.2. Finally, the testbed riser simulation results are contained in chapter 4. The results include a mesh sensitivity study in section 4.2, the flex joint results and analysis in section 4.3, and buoyancy module results and analysis in section 4.4.

1.6 Contributions

The principle contributions of this thesis are:

1. A simplified model of dynamic surface vessel motion due to ocean waves. The variable buoyancy algorithm provides more realistic alternative to applying prescribed motions at the boundaries of the riser without the computational expense and complexity of more involved computational fluid dynamics.

2. A wake oscillator with structural acceleration coupling is used to model vortex induced vibration. Flexible cylinder response to this particular wake oscillator model has only been predicted with constant tension risers with a travelling wave equation as in [34].

3. Tracking vibration amplitudes by dynamically evaluating the cross-flow direction axis and integrating the component of structural velocity in that direction through time. This allows the VIV simulator to be used with multidirectional water currents or structures which have significant deflections, such as towed or remotely operated vehicles.

4. Qualitative and quantitative analysis of the performance of flex joints in attenuating VIV response in a marine riser.

5. Qualitative and quantitative analysis of the performance of buoyancy modules in attenuating the VIV response in a marine riser.

Chapter 2

Theory

In this chapter, the core simulator components including a rigid body dynamics model needed to represent the dump valve and surface vessel and a finite element model needed to represent the riser are introduced. First, background on metal fatigue theory is introduced in section 2.1. Next, dynamic reference frames used to study the rigid body and local riser hydrodynamic effects are introduced in section 2.2. The rigid body model is presented in section 2.3.1. The rigid body dynamics model was first described in [39] and implemented and coupled to the finite element cable model in [40]. Section 2.3.1 discusses the variable buoyancy algorithm, which adds a dynamic forcing component due to ocean surface waves to the rigid body model. Finally, section 2.3.2 presents the finite element riser model and the discretisation of hydrodynamic forcing. The governing equations of the VIV model are revealed in section 2.3.3.

2.1 Structural Fatigue Failure

Structural fatigue failure can be induced when oscillating stresses are present in a structure. This occurs because the dynamic loads allow microfractures in the material

to grow and gradually undermine the strength of the structure until a catastrophic failure occurs. Fatigue failure can be difficult to detect or anticipate because the magnitude of the oscillating forces do not necessarily exceed the static yield strength, which is commonly used as an engineering design guideline.

Some materials, such as steel, exhibit a fatigue endurance limit: if the magnitude of the oscillatory von Mises stresses (see Appendix F) are under this endurance limit the material will not fail no matter how many load cycles are applied. Figure 2.1 shows the presence of the endurance limit from experiments performed on steel samples.

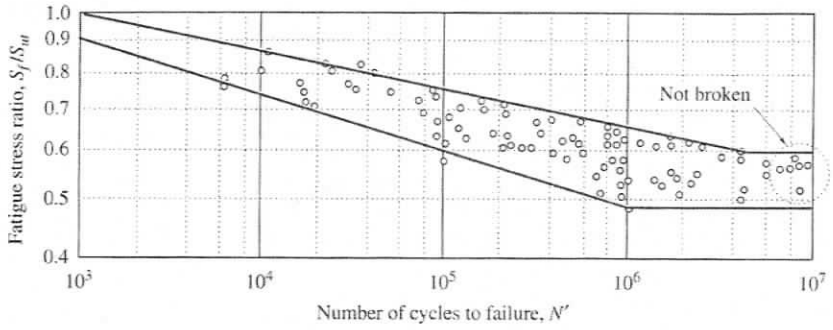

Figure 2.1: Fatigue endurance limit for steel [41]

If the magnitude of the oscillatory force is above the endurance limit, the number of cycles until failure can be determined from the formula which gives the relationship between low cycle (1000 cycles) and high cycle (1,000,000 cycles) fatigue [41], assuming a linear logarithmic relationship demonstrated by Figure 2.1:

$$N_i = \left(\frac{S_f}{a_s}\right)^{\frac{1}{b_s}} \tag{2.1}$$

where N_i is the number of cycles until failure, S_f is the von Mises stress amplitude, and a_s and b_s are constants that are evaluated at the low cycle and high cycle fatigue strength limits S_l and S_e, respectively:

$$b_s = -\frac{1}{3}\log\left(\frac{S_l}{S_e}\right) \tag{2.2}$$

$$a_s = \frac{(S_l)^2}{S_e} \tag{2.3}$$

The low and high cycle fatigue strengths for steel for axial loading are [41]:

$$S_l = 0.75S'_u \tag{2.4}$$

$$S_e = 0.45S'_u \tag{2.5}$$

where S'_u is the modified ultimate strength of the material. Note that if the von Mises stress amplitude is less than the high cycle fatigue strength limit, there will be no structural failure due to fatigue damage. The modified ultimate strength is linearly proportional to the ultimate strength of the material, S_u, and is dependent on several factors that are used to more accurately predict the fatigue limits. These factors include the surface finish factor, k_f, the size factor, k_s, and the reliability factor, k_r:

$$S'_u = k_f k_s k_r \left(S_u\right) \tag{2.6}$$

A rough surface finish on the structure will nucleate more microfractures and decrease the fatigue life of the part. The size factor accommodates the scale difference of the actual part from the parts used in the original experiments to evaluate the fatigue strength of a particular material. The surface finish factor is given by [41]:

$$k_f = eS_u^f \tag{2.7}$$

where e and f are coefficients that depend on the type of manufacturing method. For a forged steel part, the values are 272 MPa and -0.995 for e and f, respectively. The size factor for bending and torsion loadings is [41]:

$$k_s = 1.189D^{-0.112} \tag{2.8}$$

which can only be applied to the diameter range:

$$8mm \leq D \leq 250mm$$

However, for axial loading, $k_s = 1$. The reliability factor accounts for scatter in the experimentally obtained data from fatigue studies. For 99% probability of survival, the reliability factor is given as $k_r = 0.82$. Equations (2.1) through (2.8) allow the number of cycles until failure to be calculated given the nonzero-mean von Mises stress amplitude of S_f. Calculations of testbed riser fatigue parameters needed for these equations can be seen in Appendix B.

The VIV simulator can establish the von Mises stress profile in the testbed riser for individual ocean current profiles. However, it is unreasonable to assume that only a single or even a few ocean current profiles will be present during the lifetime of the riser because of the tidal and seasonal variations in the marine environment. An estimation of the life of the riser is only as accurate as the long-term knowledge of currents in the area of operation; the testbed riser response to many different current profiles must be found individually, and the damage is then accrued and quantified as each current profile comes to bear on the riser. For each profile, a cross section of the riser will undergo a new stress oscillation, the mean value and amplitude of which could change resulting in a different N_i value. Miner's rule predicts failure by considering how cycles due to each distinct stress oscillation contribute to failure [41]. According to Miner's rule, failure occurs if:

$$\sum \frac{n_i}{N_i} \geq 1 \tag{2.9}$$

where N_i is the number of cycles needed for fatigue failure due to the ith ocean current profile and n_i is the number of completely reversed von Mises stress cycles loaded by the ith ocean current profile through the life of the riser.

Calculation of the fatigue life of the testbed riser was not completed. In order to determine the fatigue life, the testbed riser response to many different current profiles must be found and the cumulative damage determined with Miner's rule. Information on long-term ocean current trends was limited and thus limits the reliability of the results. Instead, the safety factor guarding against fatigue or yield failure is calculated with the use of a modified Goodman diagram seen in Figure 2.2. On the modified Goodman diagram, the mean stress is given along the horizontal axis and the total fluctuation in stress is plotted on the horizontal axis. Lines ABCDE are defined by the magnitudes of Se, Sy, and S'_u and give the allowable stress envelope the structure may endure without fatigue or yield failure. For example, a mean stress at point L seen in Figure 2.2 on the mean stress line will allow a maximum stress amplitude up to point N before fatigue failure will ensue. Lines AB and DE are equidistant to the mean stress line as are the yield lines BC and CD.

The equation for fatigue failure governed by line AB in Figure 2.2 is:

$$\sigma_{max} + \sigma_m \left(\frac{S_e}{S_u} - 1 \right) = \frac{S_e}{n_s} \tag{2.10}$$

where σ_{max} is the maximum of the oscillating von Mises stress (described in Appendix F), σ_m is the mean of the oscillating von Mises stress, and n_s is the safety factor. Note that line AB (or DE) is only valid for the mean stress range:

$$0 \leq \sigma_m \leq \frac{S_y - S_e}{1 - \frac{S_e}{S_u}} \tag{2.11}$$

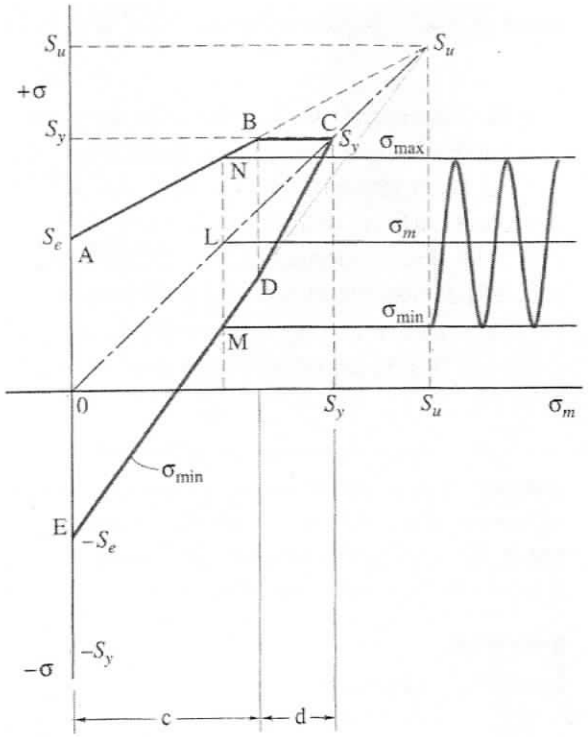

Figure 2.2: Modified Goodman diagram, adapted from [41]. Only the unmodified ultimate, S_u, yield, S_y, and endurance limit strengths, S_e, are needed to form the diagram, which indicates mean stress on the horizontal axis and fluctuating stress on the vertical axis. Line 0LC is the mean stress line. Lines AB and DE are both Goodman lines; if the maximum stress is above AB the structure will fail from fatigue. Lines BC and CD are yield lines; if the maximum stress is above BC then the structure will fail from yield. For example, for a mean stress at point L, the structure will fail from fatigue if the maximum stress exceeds the value at point N.

The equation for yield failure governed by line BC (or CD) is:

$$\sigma_{max} = \frac{S_y}{n_s} \tag{2.12}$$

The yield failure region is in the mean stress range:

$$\frac{S_y - S_e}{1 - \frac{S_e}{S_u}} \leq \sigma_m \leq S_y \tag{2.13}$$

For a characteristic current profile, the fully developed riser dynamics can be

established by simulation. At each finite element node point of the model the von Mises stress profile and thus safety factor, n_s, can be calculated via equation (2.10) and used to compare the performance of various VIV mitigation devices.

2.2 Riser System Kinematics

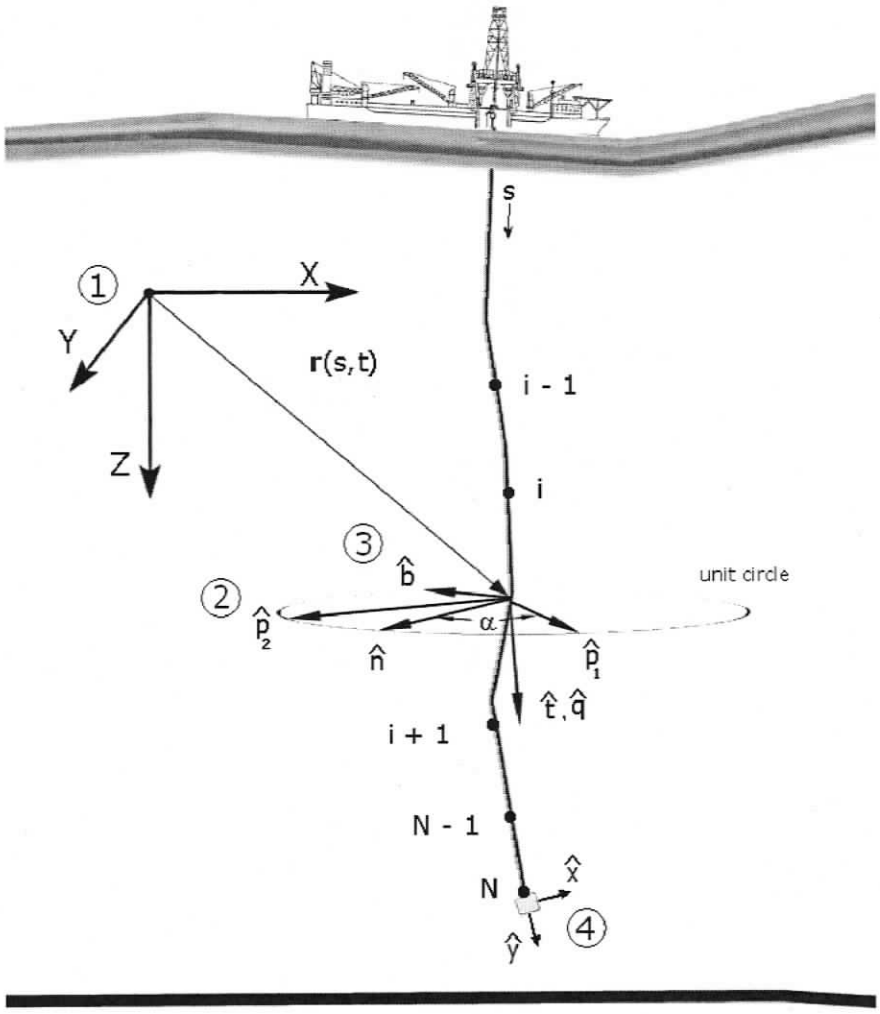

Figure 2.3: Global testbed riser representation. Several reference frames can be seen: (1) inertial reference frame; (2) local riser frame; (3) Frenet frame; (4) Body-fixed dump valve frame.

The testbed riser, connected to both a surface ship and a lumped mass, can be seen in Figure 2.3. The inertial reference frame can be seen arbitrarily placed in the environment. A continuous reference space curve $\boldsymbol{r}(s,t)$ is used to help represent the riser structure with parameters distance s along the riser and at some point in time t. To properly model torsion effects, the riser cross section is able to twist about the reference curve. To facilitate calculation of hydrodynamic and internal structural forces, several moving reference frames are used in addition to an inertial reference frame. Two reference frames are aligned with the riser and are used to evaluate the internal forces. The Frenet frame consists of orthogonal vectors tangent $\hat{\boldsymbol{t}}$ that points in the tangential direction of the curve, normal $\hat{\boldsymbol{n}}$ that points in the direction of the center of curvature, and binormal $\hat{\boldsymbol{b}}$, which completes the coordinate triad. It should be noted that $\hat{\boldsymbol{t}}$ and $\hat{\boldsymbol{n}}$ form the osculating plane in which the center of curvature lies. An additional local body frame, consisting the orthogonal principal normal vectors $\hat{\boldsymbol{p_1}}$, $\hat{\boldsymbol{p_2}}$, and tangent $\hat{\boldsymbol{q}}$, is fixed to the riser cross-section and is separated from the Frenet frame by rotation angle α about the tangent vector $\hat{\boldsymbol{t}}$, or $\hat{\boldsymbol{q}}$. The local riser frame orientation, as well as the frames attached to the dump valve and surface vessel, can be tracked with the use of an Euler angle set. The $Z(\psi) - Y(\theta) - X(\phi)$ Euler angle set [42] describes the body-fixed rotation sequence that produces the orientation of any of the moving reference frames relative to the inertial reference frame. The Euler angle set produces a transformation matrix that can be used to convert vector components to be in terms of either the moving frame or inertial reference frame.

Figure 2.3 also shows the discrete nodes of the riser finite element mesh, which number from 0 on the ship to N at the lumped mass.

2.2.1 Dump Valve and Surface Vessel Reference Frames

Figure 2.4 illustrates the dump valve with the body fixed frame $(x - y - z)$ attached at the center of mass of the rigid body. The vector describing the body position and

orientation in terms of the inertial reference frame is:

$$\boldsymbol{X} = [x, y, z, \phi, \theta, \psi]^T \tag{2.14}$$

The body velocity is expressed in terms of the body frame:

$$\dot{\boldsymbol{X}}_b = [u, v, w, p, q, r]^T \tag{2.15}$$

where the $\dot{\boldsymbol{X}}_b$ denotes the velocities in terms of the body frame, and u,v,w are the components of linear velocity in the direction of the body frame axis x,y,z, respectively. The variables p,q,r are the angular velocity values about the frame axis x,y,z, respectively. Note that the operator $\dot{()}$ represents absolute differentiation with respect to time t.

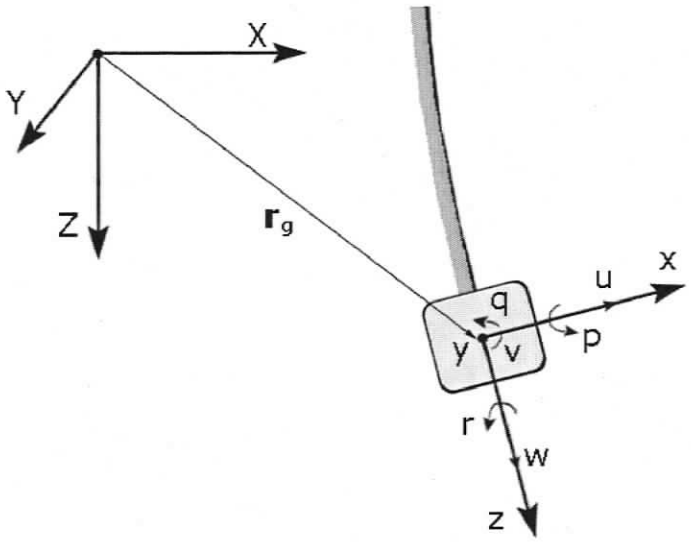

Figure 2.4: Dump valve at position $\boldsymbol{r_g}$ in inertial frame $(X - Y - Z)$. The angular velocity components p,q,r and linear velocity components u,v,w defined in terms of the body fixed frame can be seen about their respective axis.

The orthonormal transformation matrix $\mathbf{T}_1$ converts vectors expressed in the body coordinate system into the inertial coordinate system. For example, the local linear

velocities expressed in the body fixed frame can be found in terms of the inertial frame:

$$\begin{bmatrix} \dot{x} \\ \dot{y} \\ \dot{z} \end{bmatrix} = \mathbf{T}_1 \begin{bmatrix} u \\ v \\ w \end{bmatrix} \tag{2.16}$$

A rotation matrix can not be used to relate the local angular velocities to the rate of change of Euler angles. The nonlinear transformation matrix, $\mathbf{T}_2$ provided by [39]:

$$\begin{bmatrix} \dot{\psi} \\ \dot{\theta} \\ \dot{\phi} \end{bmatrix} = \mathbf{T}_2 \begin{bmatrix} p \\ q \\ r \end{bmatrix} \tag{2.17}$$

Following a yaw (ψ), pitch (θ), and roll (ϕ) Euler angle set, the transformation matrices become:

$$\mathbf{T}_1 = \begin{bmatrix} c\theta c\psi & s\theta s\phi c\psi - c\phi s\psi & s\theta c\phi c\psi + s\phi s\psi \\ c\theta s\psi & s\phi s\theta s\psi + c\phi c\psi & c\phi s\theta s\psi - s\phi c\psi \\ -s\theta & c\theta s\phi & c\theta c\phi \end{bmatrix} \tag{2.18}$$

$$\mathbf{T}_2 = \begin{bmatrix} 1 & s\phi t\theta & c\phi t\theta \\ 0 & c\phi & -s\phi \\ 0 & s\phi/c\theta & c\phi/c\theta \end{bmatrix} \tag{2.19}$$

where, for brevity, the operators have been defined:

$$c(\cdot) = \cos(\cdot) \tag{2.20}$$

$$s(\cdot) = \sin(\cdot) \tag{2.21}$$

$$t(\cdot) = \tan(\cdot) \tag{2.22}$$

Equations (2.18) and (2.19) are then assembled to generate the transformation matrix which is used to convert linear and angular body velocities and accelerations into absolute vector quantities in terms of the inertial reference frame:

$$\mathbf{T} = \begin{bmatrix} \mathbf{T}_1 & 0_{3x3} \\ 0_{3x3} & \mathbf{T}_2 \end{bmatrix} \tag{2.23}$$

The velocities expressed in the inertial frame are therefore:

$$\dot{\boldsymbol{X}} = \mathbf{T}\dot{\boldsymbol{X}}_b \tag{2.24}$$

It is simple to evaluate the accelerations with the use of rigid body mass moments of inertia, which are constant with respect to the body reference frame. Equation (2.25) converts the acceleration vectors from body frame to inertial frame:

$$\ddot{\boldsymbol{X}} = \mathbf{T}\ddot{\boldsymbol{X}}_b + \dot{\mathbf{T}}\dot{\boldsymbol{X}}_b \tag{2.25}$$

Once the accelerations are expressed in terms of the inertial frame, they can be numerically integrated and the time history of the position and orientation of the body is known.

2.2.2 Riser Frenet and Local Reference Frames

The reference space curve of the riser provides the geometric curvatures and torsions which are used to evaluate the internal forces and moments. If the strain, ϵ, in the riser is small, Frenet's equations [42] relate the space curve, $\boldsymbol{r}$, to the curvature, κ, and torsion, γ, of the riser:

$$\hat{\boldsymbol{t}} = \boldsymbol{r}' \tag{2.26}$$

$$\frac{d\hat{\boldsymbol{t}}}{ds} = \kappa\hat{\boldsymbol{n}} \tag{2.27}$$

$$\frac{d\hat{\boldsymbol{n}}}{ds} = \gamma\hat{\boldsymbol{b}} - \kappa\hat{\boldsymbol{t}} \tag{2.28}$$

$$\frac{d\hat{\boldsymbol{b}}}{ds} = -\gamma\hat{\boldsymbol{n}} \tag{2.29}$$

The operator $()'$ represents absolute differentiation with respect to the unstretched curvilinear coordinate s. The curvature of the space curve, describes the deviation of the curve from a straight line and γ, the torsion of the space curve, defines how the osculating plane twists about the tangent direction $\hat{\boldsymbol{t}}$. Since the vector directions of the local Frenet frame are derived from knowledge of the reference curve, $\boldsymbol{r}(s)$, the magnitudes of κ and γ can be found from equations (2.29) and are used in section 2.3.2 to establish the internal forces of the riser. The local riser reference frame is rotated away from the Frenet frame by angle α. The total twist of the tether is [43]:

$$\tau = \gamma + \alpha' \tag{2.30}$$

Thus, provided a description of the reference curve, $\boldsymbol{r}$, and an approximation to the additional torsional deformation, α, the elastic twist of the riser cross section can be recovered.

2.2.3 Riser Hydrodynamic Reference Frame

Predicting the hydrodynamic forces requires knowledge of the relative velocity of the riser with respect to the environmental fluid. A hydrodynamic frame is introduced such that the $\hat{\boldsymbol{z}}_H$ axis aligns with the local riser tangent $\hat{\boldsymbol{q}}$. This allows velocity components tangential and normal to the riser segment to be resolved and used in Morrison's well-known hydrodynamic force approximation. The hydrodynamic reference frame, which is used exclusively to establish relative velocities, is aligned arbitrarily around the tangential vector direction of the riser. A transformation matrix defining the hydrodynamic frame with respect to the inertial frame, $\mathbf{T}_{IH}$, is created using the Euler $Z(\psi) - Y(\theta) - X(\phi)$ rotation sequence. In this case, $\psi = 0$ is applied as the x and y directions are arbitrary within the hydrodynamic force calculation: constraining ψ to 0 does not affect the magnitude of the hydrodynamic forces since the hydrodynamic frame is merely an intermediate step to resolving the forces in the inertial frame. This constraint on the precession angle, ψ, removes the possibility of a singularity in the resulting transformation matrix:

$$\mathbf{T}_{IH} = \begin{bmatrix} c\theta & s\theta s\phi & s\theta c\phi \\ 0 & c\phi & -s\phi \\ -s\theta & c\theta s\phi & c\theta c\phi \end{bmatrix} \tag{2.31}$$

The rotation angles θ and ϕ can be evaluated with knowledge of the riser tangent vector direction, $\boldsymbol{r}'$, since the tangent vector direction is also merely the hydrodynamic frame $\hat{\boldsymbol{z}}_H$ axis direction as well. The rotation matrix $\mathbf{T}_{IH}$ relates these two forms of the tangent vector:

$$\begin{bmatrix} r'_x \\ r'_y \\ r'_z \end{bmatrix} = \begin{bmatrix} t_x \\ t_y \\ t_z \end{bmatrix} = \mathbf{T}_{IH} \begin{bmatrix} 0 \\ 0 \\ 1 \end{bmatrix} \tag{2.32}$$

From equation (2.32), θ is found from:

$$\theta = \arctan 2(z_x, z_z) \tag{2.33}$$

which is then used to solve for ϕ. If $\sin\theta < \cos\theta$:

$$\phi = \arctan 2\left(-(z_y), \frac{z_z}{\cos\theta}\right) \tag{2.34}$$

or if $\cos\theta < \sin\theta$:

$$\phi = \arctan 2\left(-(z_y), \frac{z_x}{\sin\theta}\right) \tag{2.35}$$

2.2.4 Riser VIV Reference Frame

To include VIV effects along the riser, an additional frame that defines the cross-flow and in-line directions must be resolved. The hydrodynamic lift force induced by the wake oscillator model is applied in the cross-flow direction. The VIV frame is found by applying one final rotation to the hydrodynamic reference frame introduced in section 2.2.3. This rotation brings the $\hat{\boldsymbol{x}}_H$ direction into alignment with the direction of relative velocity:

$$\hat{\boldsymbol{x}}_{VIV} = \begin{bmatrix} c\psi_{VIV} & s\psi_{VIV} & 0 \\ -s\psi_{VIV} & c\psi_{VIV} & 0 \\ 0 & 0 & 1 \end{bmatrix} \hat{\boldsymbol{x}}_H \tag{2.36}$$

This new direction is the in-line direction, $\hat{\boldsymbol{x}}_{VIV}$, which is already known in terms of the hydrodynamic frame:

$$\hat{\boldsymbol{x}}_{VIV} = \begin{bmatrix} \frac{v_x}{\sqrt{v_x^2+v_y^2}} \\ \frac{v_y}{\sqrt{v_x^2+v_y^2}} \\ 0 \end{bmatrix} \tag{2.37}$$

where v_x is the component of $\boldsymbol{V}_{rel}$ in the direction $\hat{\boldsymbol{x}}_H$, and v_y is the component of $\boldsymbol{V}_{rel}$ in the direction $\hat{\boldsymbol{y}}_H$. The rotation angle can be found with knowledge of $\hat{\boldsymbol{x}}_{VIV}$ in terms of the hydrodynamic frame:

$$\psi_{VIV} = atan2\left(\frac{v_y}{\sqrt{v_x^2+v_y^2}}, \frac{v_x}{\sqrt{v_x^2+v_y^2}}\right) \tag{2.38}$$

The cross-flow direction, $\hat{\boldsymbol{y}}_{VIV}$, is the cross-product between $\hat{\boldsymbol{x}}_{VIV}$ and the local space curve tangential vector, $\hat{\boldsymbol{q}}$:

$$\hat{\boldsymbol{y}}_{VIV} = \hat{\boldsymbol{q}} \times \hat{\boldsymbol{x}}_{VIV} \tag{2.39}$$

Figure 2.5 shows vortices shed perpendicular to the local riser section. Figure 2.6 shows a more detailed view of the VIV frame from Figure 2.5 and its relative orientation to the local hydrodynamics reference frame with axis $\hat{\boldsymbol{x}}_H$ and $\hat{\boldsymbol{y}}_H$. A correction angle, ψ_{VIV} is used to find the transformation matrix $\mathbf{T}_{VIV}$, which translates the hydrodynamic VIV loads into the inertial frame. This transformation matrix uses the same ϕ and θ angles as $\mathbf{T}_{IH}$, but instead of constraining ψ to zero, ψ_{VIV} is used and a matrix in the form of equation (2.18) is found.

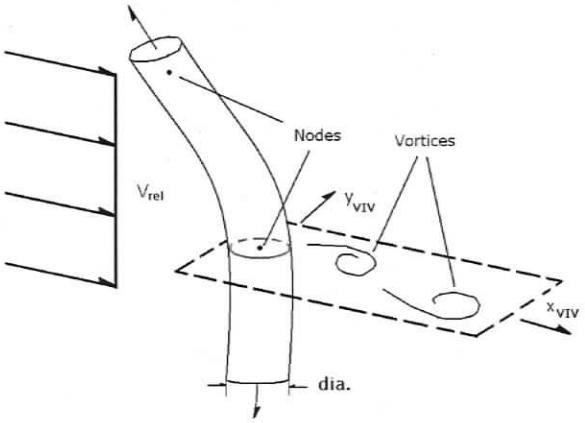

Figure 2.5: Riser segment with VIV frame.

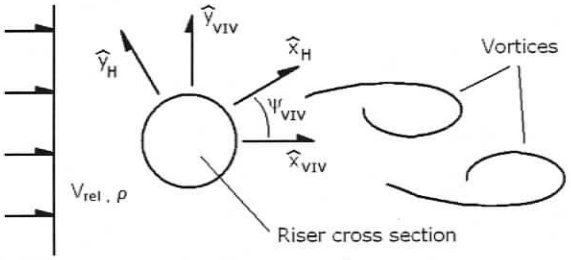

Figure 2.6: Vortex induced vibration reference frame. The hydrodynamic frame components, $\hat{\boldsymbol{x}}_H$ and $\hat{\boldsymbol{y}}_H$ are shown in addition to the correction angle ψ_{VIV}. The hydrodynamic frame is oriented arbitrarily about the riser tangential vector $\hat{\boldsymbol{t}}$ (into the page). However, the VIV frame has a well defined precession angle ψ_{VIV} about $\hat{\boldsymbol{q}}$, if $\boldsymbol{V}_{rel}$ is well defined.

2.3 Riser System Dynamics

In this section, a review of rigid body dynamics modelling is presented. Rigid body models are used to simulate the barge and dump valve motion. A key component of the rigid body models is how they integrate, or couple, to the riser dynamics. In section 2.3.1. The coupling of the flexible cable to a rigid dynamic body was implemented in [40]. Section 2.3.1 closely follows the presentation of [40]. Forces particular to the surface barge are the wave forces, which are described in section 2.3.1. In section 2.3.2, the finite element riser model formulation is introduced. Finally, the primary contribution of this work is the VIV force, which is presented in section 2.3.3.

2.3.1 Rigid Body Dynamics Modelling

The equation of motion of the rigid body, which relates the body accelerations to the applied forces, is derived from Newton's second law:

$$(\mathbf{M} + \mathbf{M}_A)\,\ddot{\boldsymbol{X}}_b = \boldsymbol{F}_B(\boldsymbol{X}) + \boldsymbol{F}_D(\dot{\boldsymbol{X}}_{br}) + \boldsymbol{F}_C(\dot{\boldsymbol{X}}) \tag{2.40}$$

where $\mathbf{M}$ and $\mathbf{M}_A$ are the mass and added mass matrices and $\boldsymbol{F}_B$,$\boldsymbol{F}_D$,$\boldsymbol{F}_C$, are the buoyancy, drag, and riser forces, respectively. The term $\dot{\boldsymbol{X}}_{br}$ is the relative body velocity found by including the prevailing current of the irrotational fluid environment:

$$\dot{\boldsymbol{X}}_{br} = \begin{bmatrix} v_x - v_{fx} \\ v_y - v_{fy} \\ v_z - v_{fz} \\ p \\ q \\ r \end{bmatrix} \tag{2.41}$$

where v_{fx},v_{fy},v_{fz} are the environment fluid current in terms of the body reference frame. These can be easily found from values specified in the inertial coordinate system with the help of the transformation matrix $\mathbf{T}_1$.

The mass matrix in equation (2.40) is given by:

$$\mathbf{M} = \begin{bmatrix} m & 0 & 0 & 0 & 0 & 0 \\ 0 & m & 0 & 0 & 0 & 0 \\ 0 & 0 & m & 0 & 0 & 0 \\ 0 & 0 & 0 & I_x & I_{xy} & I_{xz} \\ 0 & 0 & 0 & I_{xy} & I_y & I_{yz} \\ 0 & 0 & 0 & I_{xz} & I_{yz} & I_z \end{bmatrix} \tag{2.42}$$

where m is the body mass, and I_x,I_y,I_z are the mass moment of inertia values and I_{xy},I_{xz},I_{yz} are the products of inertia. The added mass matrix is given by:

$$\mathbf{M}_A = \begin{bmatrix} x_{\dot{u}} & x_{\dot{v}} & x_{\dot{w}} & x_{\dot{p}} & x_{\dot{q}} & x_{\dot{r}} \\ y_{\dot{u}} & y_{\dot{v}} & y_{\dot{w}} & y_{\dot{p}} & y_{\dot{q}} & y_{\dot{r}} \\ z_{\dot{u}} & z_{\dot{v}} & z_{\dot{w}} & z_{\dot{p}} & z_{\dot{q}} & z_{\dot{r}} \\ l_{\dot{u}} & l_{\dot{v}} & l_{\dot{w}} & l_{\dot{p}} & l_{\dot{q}} & l_{\dot{r}} \\ m_{\dot{u}} & m_{\dot{v}} & m_{\dot{w}} & m_{\dot{p}} & m_{\dot{q}} & m_{\dot{r}} \\ n_{\dot{u}} & n_{\dot{v}} & n_{\dot{w}} & n_{\dot{p}} & n_{\dot{q}} & n_{\dot{r}} \end{bmatrix} \tag{2.43}$$

Added mass is the result of an additional drag force that develops during a rigid body's acceleration through a fluid. The added mass coefficients within $\mathbf{M}_A$ are specific to the geometry of the rigid body, and most often, tow tank experiments are required to estimate them. However, the off diagonal terms are generally neglected if the body is symmetric and operates at relatively low speeds [44]. It is not unusual for a constant coefficient of added mass to be used for simple geometries, and with constant entries in $\mathbf{M}_A$, the acceleration $\ddot{\boldsymbol{X}}_b$ can be found by explicitly evaluating (2.40) since the state information, including position and velocity of the body, are known at each step in time of the simulation. A table of added mass coefficients for lateral accelerations of simple geometries can be seen in Figure 2.7. These coefficients are for the linear acceleration diagonal terms of $\mathbf{M}_A$ only.

The barge was approximated as a rectangular prism of dimensions 152m, 30.5m, and 11.6m. The added mass coefficients are found by using the wetted dimensions of the barge assuming 50% submergence in a flat sea. The second entry in Figure 2.7 is used to find the added masses and the fourth entry in Figure 2.7 was used to find the rotational added mass. The drag coefficients used for each wetted face were found by interpolating the laminar coefficients for a flat plate of appropriate dimensions seen in Figure 2.8. The dump valve was approximated as a sphere of radius 1 m and the

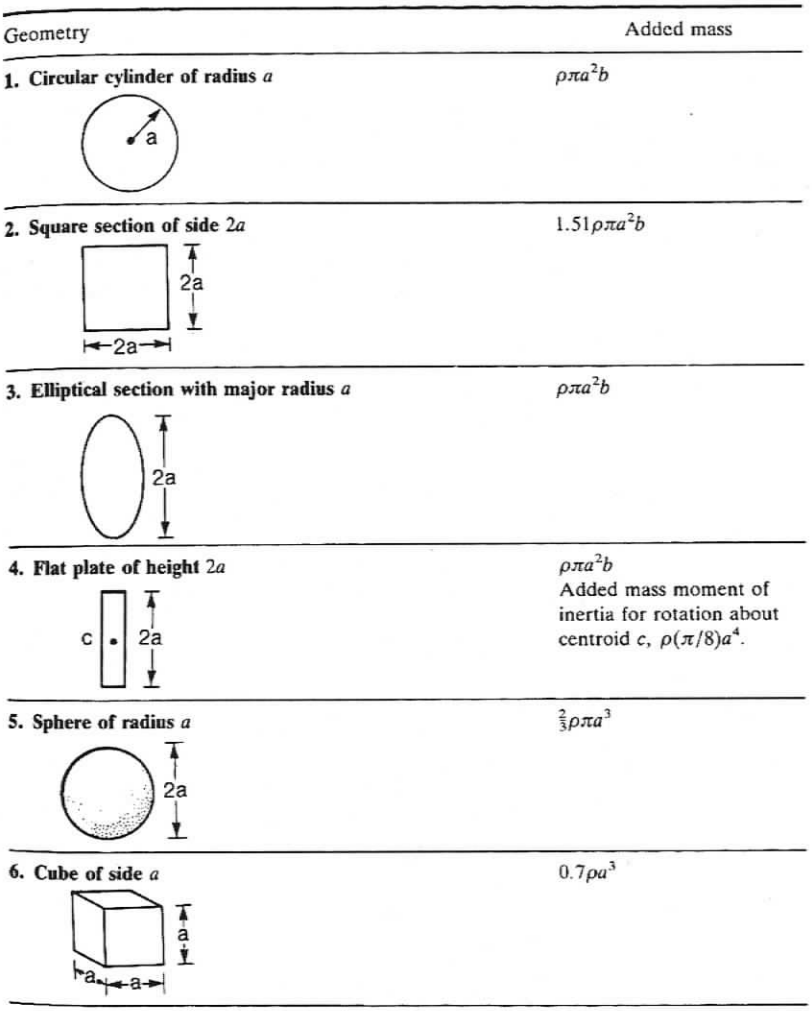

Figure 2.7: Added mass coefficients for lateral acceleration [12]

drag coefficients and added mass were interpolated from known values provided in Figures 2.7 and 2.8.

Variable Buoyancy Model

The existing rigid body dynamics model was developed for use in underwater remotely operated vehicle (ROV) simulation and lacked the forcing effects of ocean surface waves. These effects are necessary to simulate the motion of the surface barge without resorting to a prescribed kinematic motion.

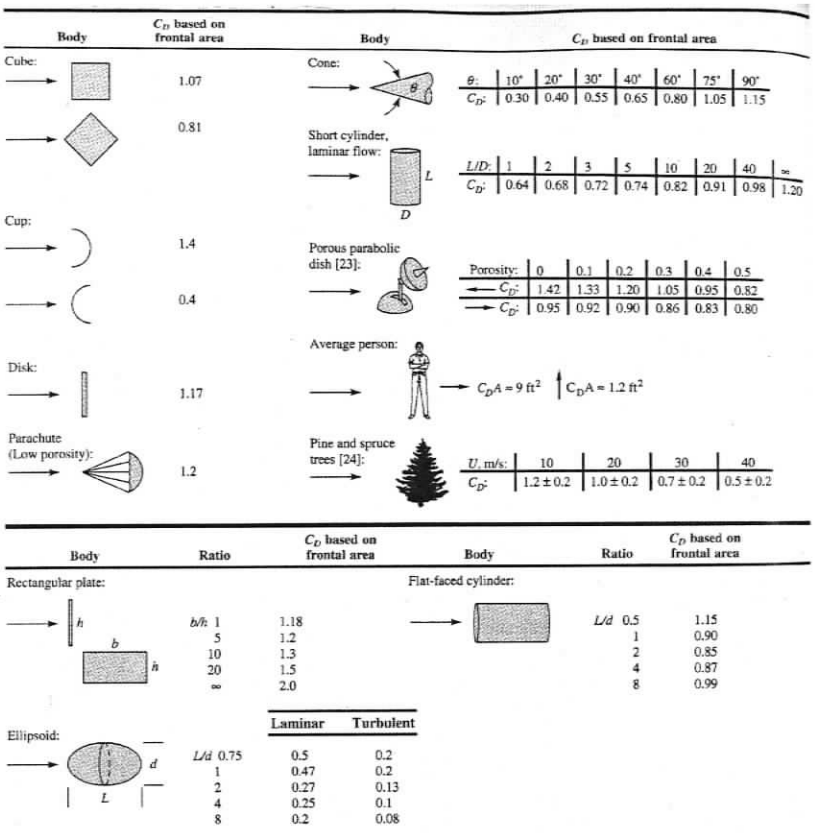

Figure 2.8: Drag coefficients for various body shapes [9]

A body floating in the ocean is subject to many forces as illustrated in Figure 2.9. Basic information on the body is known: mass, volume, geometric and inertia properties. If the body is completely submerged, the buoyancy force calculation is trivial and the drag force is evaluated with the use of well-known empirical drag coefficients. The surface wave excitation forces require more complex calculations that are highly nonlinear. For example, in particularly violent seas, portions of a body can momentarily surface and cause impact loads upon re-entry into the water. Another impact loading is when a wave breaks at the moment of contact with a structure. Further discussion on impact loadings that emphasise the complexity of the wave force calculation can be found in [45]. Wave diffraction and reflection effects about the structure can be neglected if the ocean wavelength is large compared to a characteristic dimension of the surface vessel (see, for example, [2, 45]). In order

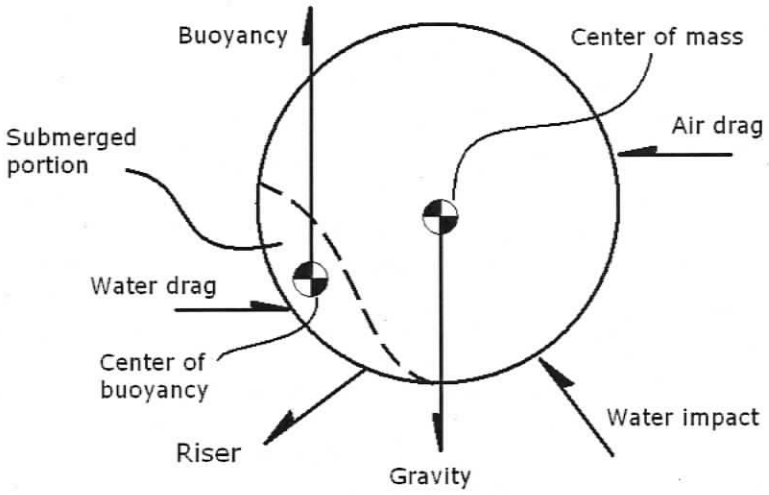

Figure 2.9: Body subjected to ocean environment forces

to reduce complexity, water impact, wave reflection and diffraction effects, and drag modifications due to partial submergence were neglected. What results is a variable buoyancy model that calculates the buoyancy force acting on a surface vessel using current state information, geometric information of the body shape and a dynamic ocean height profile.

Submerged Volume Algorithm

The buoyancy force acting on a completely submerged object, seen in 2.10 is easy to calculate with Archimedes law of buoyancy: the magnitude of buoyancy is the weight of the displaced fluid, and the direction is opposite that if the gravitational acceleration.

However, the buoyancy force acting on a partially submerged arbitrarily oriented object is not so trivial to calculate. Figure 2.11 shows an object in the ocean and Figure 2.12 shows the assumed water height within the body represented by a discrete array of volume cells.

The Froude-Krylov hypothesis (see [46]), which states that the partially submerged

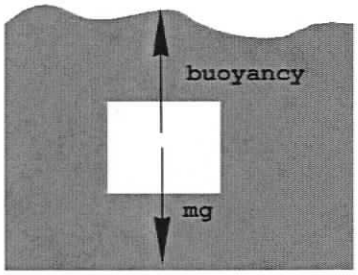

Figure 2.10: Submerged body

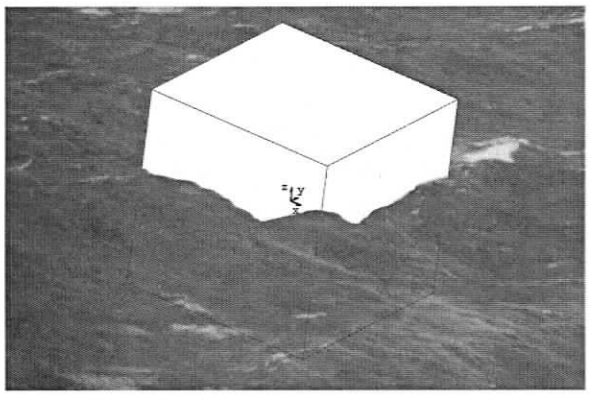

Figure 2.11: Noisy ocean surface

object does not significantly disturb the ocean water particles, was used. This allows the use of equation (2.58) to assist in evaluating the displaced water height. The submerged volume is approximated with discrete rectangular cells of known size in the object's body coordinate system. In order to solve the water height in each cell, an algorithm was developed by analysing a vector equation derived from Figure 2.13, which is evaluated explicitly based on the state of the body and sea surface displacement, ζ. Figure 2.13 displays a vector diagram that is used to derive the equation that finds the water height. The position vector of the top of the cell can be written in terms of the global coordinate system or the local body coordinate system. In terms of the global coordinate system, it is simply:

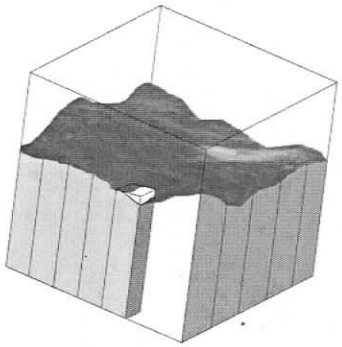

Figure 2.12: Submerged volume approximation

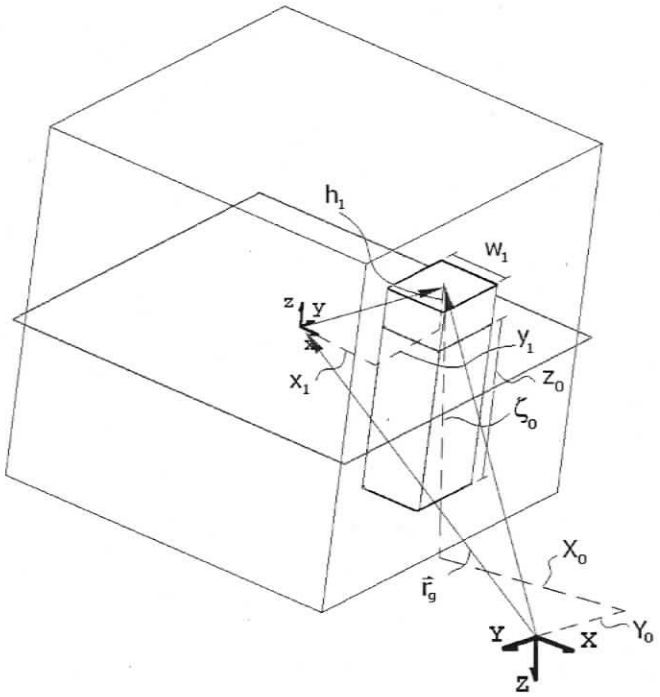

Figure 2.13: Vector diagram of water height

$$\boldsymbol{h_c} = X_0\hat{\boldsymbol{I}} + Y_0\hat{\boldsymbol{J}} + \zeta(X_0, Y_0, t)\hat{\boldsymbol{K}} \tag{2.44}$$

where $\boldsymbol{h_c}$ is the cell height position vector, $\hat{\boldsymbol{I}} - \hat{\boldsymbol{J}} - \hat{\boldsymbol{K}}$ are the global coordinate unit vector directions, and X_0 and Y_0 are the positions on the water surface in global coordinates. In terms of body coordinates, this water height can be written:

$$\boldsymbol{h_c} = \boldsymbol{r_g} + x_1\hat{\boldsymbol{i}} + y_1\hat{\boldsymbol{j}} + h_1\hat{\boldsymbol{k}} \tag{2.45}$$

where $\boldsymbol{r_g}$ is the vector locating the body's coordinate system from the global coordinate system origin, $\hat{\boldsymbol{i}} - \hat{\boldsymbol{j}} - \hat{\boldsymbol{k}}$ are the body coordinate system unit vectors, and x_1 and y_1 are the location of the cell in the body coordinate system with corresponding height h_1.

The rotation matrix in equation (2.18) is a function of the body state and it relates vectors in the body reference frame to the inertial reference frame. Combining equations (2.44), (2.45) and (2.45) gives a system of three equations that can not be solved analytically because of the trigonometric function:

$$\begin{bmatrix} X_0 \\ Y_0 \\ \sum_i^{N_w} \frac{H_i}{2} \cos\left(k_i X_0 + l_i Y_0 - \omega_i t\right) \end{bmatrix} = \boldsymbol{r_g} + \mathbf{T}_1 \begin{bmatrix} x_1 \\ y_1 \\ h_1 \end{bmatrix} \tag{2.46}$$

A numerical optimization technique applied to equations (2.46) provides a relatively quick solution.

Recovering the buoyant force and tipping moment

There are several steps required to numerically determine the cell height from equation (2.46). The process is iterative and uses the bisection method, which is guaranteed to

converge for a function that satisfies the intermediate-value theorem (see Appendix C for more detail).

Recall that x_1 and y_1 are the known locations of the cell in the body coordinate system. The vector $\boldsymbol{r_g}$ and the transformation matrix $\mathbf{T}_1$ are both known in terms of the body state data. An estimate of the water height h_1 is made. Equations (2.46) then gives the corresponding values of X_0 and Y_0. The remaining equation from (2.46) is rearranged:

$$\begin{aligned} \sum_i^{N_w} \frac{H_i}{2} \cos\left(k_i X_0 + l_i Y_0 - \omega_i t\right) &= \boldsymbol{r_g} \cdot \hat{\boldsymbol{K}} + (-s\theta)x_1 + (c\theta s\phi)y_1 + (c\theta c\phi)h_1 \\ error &= \boldsymbol{r_g} \cdot \hat{\boldsymbol{K}} + (-s\theta)x_1 + (c\theta s\phi)y_1 + (c\theta c\phi)h_1 \\ &\quad - \sum_i^{N_w} \frac{H_i}{2} \cos\left(k_i X_0 + l_i Y_0 - \omega_i t\right) \end{aligned} \tag{2.47}$$

With the correct value of h_1, the error value given by equation (2.47) is zero and so it is the optimization function for use with the bisector method (see Appendix C). Before the bisector method can be used, starting values h_{1xa} and h_{1xb} that produce $error_a$ and $error_b$ from (2.47) such that $error_a$ and $error_b$ have different signs are required. The upper and lower height values from the objects geometry at the volume cell location are submitted to (2.47) first. If the resulting h_{1xa} and h_{1xb} values have the same sign, the body is either totally submerged or exposed and further iteration is not necessary. Otherwise, the bisector algorithm is invoked and the approximate displaced water height is found. Convergence and validation analysis is discussed in chapter 3.

Once the cell height is known, the submerged volume is found simply from adding the volumes of each cell:

$$V_{sub} = \sum_i^{N_c} w_i^2 (h_i - z_o) \tag{2.48}$$

where V_{sub} is the submerged volume, N_c is the total number of cells used, w_i is the width of cell, h_i is the height of the cell, and z_0 is the bottom of the body. The component directions of the vector that locates the centroid of the submerged volume can also be found. This is important since the centroid is the point of application of the buoyancy force vector:

$$x_{bf} = \frac{\sum_i^{N_c} w_i^2 (h_i - z_o)}{V_{sub}} \tag{2.49}$$

where x_i is the location of the cell (in body coordinates) and x_{bf} is the overall x-direction component (in body coordinates) centroid. A similar process is required for the y-direction location of the centroid. The z-direction centroid component is:

$$z_{bf} = \frac{\sum_i^{N_c} \frac{1}{2}(h_i - z_0) w_i^2 (h_i - z_o)}{V_{sub}} \tag{2.50}$$

The vector direction of the buoyancy force is in the opposite direction of gravitational acceleration in the global coordinate system. With the use of the transformation matrix from equation (2.18), the buoyancy force can now be described in terms of the body coordinate system and applied in equation (2.40). The force $\boldsymbol{f_{bf}}$ due to buoyancy is:

$$\boldsymbol{f_{bf}} = g V_{sub} \mathbf{T}_1 \begin{bmatrix} 0 \\ 0 \\ -1 \end{bmatrix} \tag{2.51}$$

where g is gravitational acceleration. The moment $\boldsymbol{f_{bm}}$ due to buoyancy is:

$$\boldsymbol{f_{bm}} = g V_{sub} \begin{bmatrix} x_{bf} \\ y_{bf} \\ z_{bf} \end{bmatrix} \times \mathbf{T}_1 \begin{bmatrix} 0 \\ 0 \\ -1 \end{bmatrix} \tag{2.52}$$

Concatenating equations (2.51) and (2.52) creates the replacement buoyancy force for use in equation (2.40):

$$\boldsymbol{F_B} = \begin{bmatrix} \boldsymbol{f_{bf}} \\ \boldsymbol{f_{bm}} \end{bmatrix} \tag{2.53}$$

Ocean Surface Simulation

The ocean surface was generated through analytical knowledge of deep ocean water waves. The anatomy of an ocean wave can be seen in Figure 2.14. In the simulation, it is assumed only planar waves, which propagate uniformly in one direction.

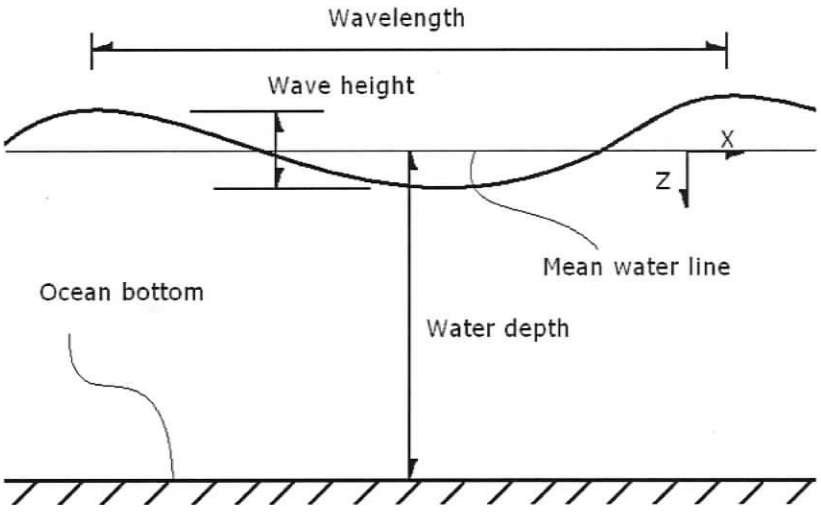

Figure 2.14: Anatomy of an ocean wave

Ocean surface displacement can be modelled with Airy waves, which are merely sinusoidal functions, as long as the Airy wave height is much smaller than the wavelength [47–51]. Equation (2.54) shows the sea surface elevation, $\zeta(x, y, t)$, as a function of the wave height H, wave number k (x-component) and l (y-component), and circular frequency ω:

$$\zeta(x, y, z) = \frac{H}{2} \cos(kx + ly - \omega t) \tag{2.54}$$

where x and y are coordinates along the sea surface and t is some point in time. Airy waves can be superimposed to form models of complex sea states with multidirectional wave fronts.

Ocean gravity waves exhibit a dispersion relation, which relates the frequency to the wave number (see, for example, [49–51]):

$$\omega = \sqrt{gK_w \tanh(K_w d)} \tag{2.55}$$

where g is acceleration due to gravity, d is the ocean depth, and K_w is the magnitude of the wave vector:

$$K_w = \sqrt{k^2 + l^2} \tag{2.56}$$

In deep water, $\tanh(K_w d) \approx 1$ so a much simpler dispersion relation exists:

$$\omega = \sqrt{gK_w} \tag{2.57}$$

Equation (2.54) only describes a monochromatic wave, though in reality the sea surface is comprised of a wide spectrum of wave frequencies and amplitudes. To improve the model equation (2.54) can be rewritten:

$$\begin{aligned} \zeta(x, y, z) &= \sum_{i}^{N_w} \zeta_i \\ &= \sum_{i}^{N_w} \frac{H_i}{2} \cos(k_i x + l_i y - \omega_i t) \end{aligned} \tag{2.58}$$

for N_w planar monochromatic waves that make up the ocean surface. Figure 2.15 shows visualized output of two planar waves: wave 1 has the vector $l_1\hat{\boldsymbol{J}}$ and wave 2 has the vector $k_2\hat{\boldsymbol{I}}$.

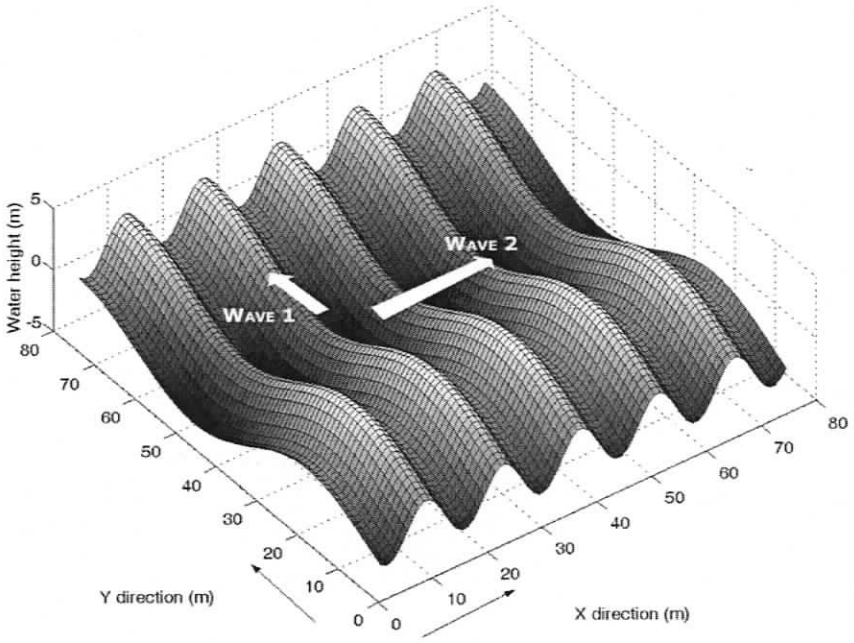

Figure 2.15: Superposition of two planar waves

2.3.2 Flexible Riser Dynamics

The intent of this section is to provide a brief introduction to how the hydrodynamic loading function is discretised and applied to the nodes of the finite element mesh, and how this hydrodynamic force drives motion and deformation of a riser. This provides the foundation for how the VIV forces are superimposed within an existing finite element riser model. Recall that the slenderness of the testbed riser, described by an aspect ratio of almost 5000 can be matched by a length of human hair almost 0.5 m long. A free body diagram of an infinitesimally long segment of a continuous slender structure can be seen in Figure 2.16. At both ends of the segment, the local Frenet and body reference frames, which are required to evaluate external and internal

forces acting on the body, are shown. The ends of the segment are separated by an arc length $ds(1+\epsilon)$, where ds is the differential segment length under strain, ϵ.

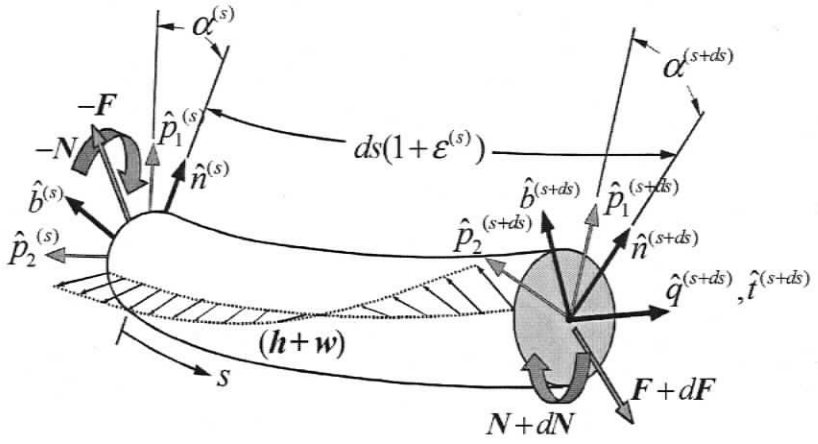

Figure 2.16: Differential riser segment [36]

Internal bending moments $\boldsymbol{N}$ and reaction forces $\boldsymbol{F}$ are also shown at the ends of the section. An external distributed hydrodynamic and gravitational force $(\boldsymbol{h}+\boldsymbol{w})$ is applied along the length of the segment. The distributed hydrodynamic loading can be the result of a combination of drag (in-line) or lift/VIV (cross-flow) forces. The equations of motion for the riser segment in the inertial reference frame are given in [36]:

$$\boldsymbol{F}' + \boldsymbol{h} + \boldsymbol{w} = \mathrm{M}_I \ddot{\boldsymbol{r}} \tag{2.59}$$

$$\boldsymbol{N}' + \boldsymbol{r}' \times \boldsymbol{F} + \boldsymbol{n} = \boldsymbol{0} \tag{2.60}$$

where $\mathbf{M}_I$ is the mass matrix (with added mass), $\boldsymbol{n}$ is the distributed applied moment. The rotational inertia is neglected for two reasons: the segment is very slender and the angular accelerations of the segment are known to be very small due to the water pulley phenomenon [36].

The internal moments are described by an extension of the Euler-Bernoulli approximation known as Love's Ordinary Approximation Theorem [43]:

$$\boldsymbol{N} = EI\kappa\hat{\boldsymbol{b}} + GJ\tau\hat{\boldsymbol{t}} \tag{2.61}$$

with riser flexural rigidity EI, torsional rigidity GJ, magnitude of curvature κ, and total twist τ. Substituting equation (2.61) into (2.60), the internal force is found in terms of the elastic deformations ϵ, κ, and τ.

In order to implement Galerkin's criterion and extract the discrete finite element equations from equation (2.60), a trial solution to the problem must be selected. The space curve of the riser is represented by discrete nodes and the riser continuum is established by interpolating between the node points:

$$\boldsymbol{r}_i(s,t) = \boldsymbol{r}^{(i-1)}\phi_{(i,1)} + \boldsymbol{r}''^{(i-1)}\phi_{i,2} + \boldsymbol{r}^{(i)}\phi_{i,3} + \boldsymbol{r}''^{(i)}\phi_{i,4} \tag{2.62}$$

where the shape functions $\phi_{i,j}$ for element i between nodes $i-1$ and i are:

$$\phi_{i,1} = \frac{s^{(i)} - s}{L_u^{(i)}} \tag{2.63}$$

$$\phi_{i,2} = \frac{1}{6}\left(\phi_{i,1}^3 - \phi_{i,1}\right)\left(L_u^{(i)}\right)^2 \tag{2.64}$$

$$\phi_{i,3} = \frac{s - s^{(i-1)}}{L_u^{(i)}} \tag{2.65}$$

$$\phi_{i,4} = \frac{1}{6}\left(\phi_{i,3}^3 - \phi_{i,3}\right)\left(L_u^{(i)}\right)^2 \tag{2.66}$$

with unstretched element length $L_u^{(i)}$ and node i distance $s^{(i)}$ along the riser. These shape functions used produce a cubic approximation to $\boldsymbol{r}$ that exhibits continuous curvature along the span of the riser. Given current state information, $\boldsymbol{r}^{(i)}$ and $\boldsymbol{r}''^{(i)}$ at both element nodes, the shape functions allow $\boldsymbol{r}$, $\boldsymbol{r}''$, and $\boldsymbol{r}'''$ to be evaluated anywhere

in the element. The Galerkin criterion is used to extract the discrete finite element equations from the equations of motion (2.60):

$$\int_V \left(\boldsymbol{F}_i' + \boldsymbol{h}_i + \boldsymbol{w}_i - \mathrm{M}_I\ddot{\boldsymbol{r}}\right)\phi_{i,j}dV = 0 \tag{2.67}$$

where $(\cdot)_i$ implies a quantity evaluated in the domain of element i with constant material properties. Focusing on equation (2.67) and integrating the first term of the integrand by parts:

$$\int_{s^{(i-1)}}^{s^{(i)}} \left(\boldsymbol{F}_i'\phi_{i,j}' + \left(\boldsymbol{h}_i + \boldsymbol{w}_i - \mathrm{M}_I\ddot{\boldsymbol{r}}_t\right)\phi_{i,j}\right) ds = \left[(-\boldsymbol{F}_i)\phi_{i,j}\right]\Big|_{s^{(i-1)}}^{s^{(i)}} \tag{2.68}$$
$$j = 1, 2, 3, 4$$

The right hand side of equation (2.68) represents the internal forces evaluated at the boundaries of the element. For a description of the internal forces $\boldsymbol{F}$, weight and buoyancy forces, $\boldsymbol{w}$, the reader is referred to [36]. The complete finite element riser model is assembled by applying equation (2.68) simultaneously to all elements.

The distributed hydrodynamic load $\boldsymbol{h}_i$ is approximated with values that are evaluated at a the end points of the element (the nodes) and blended across the element with the linear shape functions:

$$\boldsymbol{h}_i \approx \boldsymbol{h}^{(i-1)}\phi_{i,1} + \boldsymbol{h}^{(i)}\phi_{i,3} \tag{2.69}$$

Substituting equation (2.69) into equation (2.68) and performing the integration gives the hydrodynamic forces that are applied on the riser nodes.

$$\int_{s^{(i-1)}}^{s^{(i)}} \boldsymbol{h}_i \phi_{i,j} ds = \boldsymbol{H}_i = L_u^{(i)} \begin{bmatrix} \left(\frac{1}{3}\boldsymbol{h}^{(i-1)} + \frac{1}{6}\boldsymbol{h}^{(i)}\right) \\ \left(-\frac{1}{45}\boldsymbol{h}^{(i-1)} - \frac{7}{360}\boldsymbol{h}^{(i)}\right) L_i^{(i)} \\ \left(\frac{1}{6}\boldsymbol{h}^{(i-1)} + \frac{1}{3}\boldsymbol{h}^{(i)}\right) \\ \left(\frac{1}{6}\boldsymbol{h}^{(i-1)} + \frac{1}{3}\boldsymbol{h}^{(i)}\right) L_u^{(i)} \end{bmatrix} \tag{2.70}$$

where $\boldsymbol{H}_i$ is the discretised distributed hydrodynamic force that is applied on the riser nodes. These are directly proportional to the hydrodynamic forces per unit length measured at the nodes. The lumped mass assumption negates the influence on the curvature on the distributed hydrodynamic loading. The distributed hydrodynamic loading measured at the nodes for use in equation (2.70) is:

$$\boldsymbol{h}^{(i)} = -\frac{1}{2}\rho_w C_D D V_{rel}^2 \begin{bmatrix} f_p \frac{v_x}{\sqrt{v_x^2+v_y^2}} \\ f_p \frac{v_y}{\sqrt{v_x^2+v_y^2}} \\ f_q \frac{v_z}{|v_z|} \end{bmatrix} \tag{2.71}$$

where C_D is the drag coefficient of the riser, V_{rel} is the total relative velocity between the riser and fluid, v_x-v_y-v_z are the relative velocity components expressed with respect to the hydrodynamic frame at node i, and f_p and f_q are non-linear loading coefficients that are functions of the angle of V_{rel} with respect to the tangent vector of the riser, $\hat{\boldsymbol{t}}$.

2.3.3 Vortex Induced Vibration Model

This section describes the wake oscillator differential equations that are used to generate the force that is applied to the riser nodes in order to model the VIV phenomenon. The VIV effects are integrated into the riser model by superimposing the distributed lift force on the existing distributed hydrodynamic load evaluated at a node, $\boldsymbol{h}^{(i)}$.

This directly affects the total hydrodynamic force applied to the node, $\boldsymbol{H}_i$ that results from integrating over the domain of the element with the Galerkin criteria, seen in equation (2.70). The lift force per unit length is calculated and blended across the elements in the same manner as the drag force calculated by Morrison's equation.

Cross-flow effects

A wake oscillator model was selected as because its computational economy makes it feasible to use in simulation-based iterative design. In addition, wake oscillators produce accurate results when calibrated with experimental data. Usually a Van der Pol differential equation is used to generate the oscillatory behaviour of the structure lift coefficient in the wake oscillator model. They are used because they are self-starting and also produce a self-limiting structural response when driven at the structure natural frequency. The lift coefficient is then used to evaluate the lift force per unit length at the node points based on the structure relative velocity, V_{rel}, and the vortex shedding frequency predicted by the Strouhal number, S_t.

Modelling the lift coefficient by a Van der Pol differential equation is an attempt to numerically reproduce experimental observations. The wake oscillator differential equation presented here is distinct from the fundamental equations that govern vortex shedding. Originally wake oscillators were used to study single degree of freedom (DOF) rigid circular cylinder VIV behaviour. In more recent years, the use of wake oscillators has extended to modelling slender flexible circular cylinder VIV response [31, 32, 34]. The approach followed in this work is to apply a discrete distribution of wake-oscillators over the nodes of the finite element riser model.

In order to simplify the calibration process and ensure a generic and accurate tool, a simple wake oscillator model was selected. Recent implementations of wake oscillator models include [31–34]. The wake oscillator from [33] was selected due to its simplicity as well as the improved qualitative and quantitative behaviour resulting

from inertial coupling to the riser structure model:

$$\ddot{q} + \epsilon\omega_s(q^2 - 1)\dot{q} + \omega_s^2 q = \frac{A}{D}\ddot{y} \tag{2.72}$$

where A and ϵ are an experimentally determined coefficients, D is cylinder diameter, q is the Van der Pol oscillation variable, $\ddot{y}$ is structural acceleration in the cross-flow direction, and ω_s is the vortex shedding frequency given by:

$$\omega_s = 2\pi S_t \frac{V_{rel}}{D} \tag{2.73}$$

where S_t is the dimensionless Strouhal number and is approximately 0.2 for a Reynolds number range of about 300 to 10^5 [9,10,26], within which the experimental data available and many marine engineering applications take place. Equation (2.72) shows that the desired self-limiting response produced by the Van der Pol is due to the nonlinear damping term $\omega_s(q^2 - 1)\dot{q}$, which produces negative damping at low amplitudes and positive damping at large amplitudes. The relationship between the Van der Pol variable q and the lift coefficient C_L is given by:

$$q = 2\frac{C_L}{C_{L0}} \tag{2.74}$$

where C_L is the variable lift coefficient and C_{L0} is the amplitude of the lift coefficient produced by vortex shedding on a fixed cylinder, and is typically set to around 0.28. With data on forced cylinder experiments, it was observed that structural acceleration coupling to the Van der Pol provides qualitatively and quantitatively more accurate results [33] than structure displacement or velocity coupling, which are much more commonly used in the literature.

An additional stall term was proposed in [14] to limit the response of structures with low structural damping and was implemented in [32]. Only axial damping is

incorporated in the riser model. Though bending and torsion damping effects are not considered in the finite element riser model, the hydrodynamic medium swamps any structural damping such that the additional stall term was not used.

The lift coefficient was used in its classic empirical relation to quantify the lift force per unit length in the cross-flow vector direction measured at the node of the riser element:

$$\boldsymbol{h}_{VIV}^{(i)} = \frac{1}{2}\rho_w D C_L V_{rel}^2 \hat{\boldsymbol{y}}_{VIV} \tag{2.75}$$

where ρ_w is the fluid density, D is the riser (outer) diameter. Equation (2.71) is now modified to become:

$$\boldsymbol{h}^{(i)} = -\frac{1}{2}\rho_w C_D D V_{rel}^2 \begin{bmatrix} f_p \frac{v_x}{\sqrt{v_x^2+v_y^2}} \\ f_p \frac{v_y}{\sqrt{v_x^2+v_y^2}} \\ f_q \frac{v_z}{|v_z|} \end{bmatrix} + \boldsymbol{h}_{VIV}^{(i)} \tag{2.76}$$

Equation (2.72) only provides the dynamic behaviour of the lift coefficient. The direction of this new effect is the cross-flow direction and the associated magnitude of the VIV force were discussed section 2.2.4. It should be noted that the cross-flow VIV induced velocity is filtered from feeding back into the wake oscillator equation through the V_{rel} quantity as well as affecting the calculation of in-line and cross-flow directions. However, VIV velocity is not filtered when the hydrodynamic drag force is calculated.

In-line effects

The cross-flow vibration behaviour can influence the in-line direction through amplification of the drag coefficient. Depending on the nature of the structure, the amplified

drag coefficient can induce low frequency in-line vibration, as demonstrated in [32].

The drag coefficient amplification modifier was provided by [15]:

$$\frac{C_d}{C_{d0}} = 1.0 + 1.043 \left(\frac{2Y_{rms}}{D} \right)^{0.65} \tag{2.77}$$

where C_d is the variable drag coefficient, C_{d0} is the steady-state drag coefficient, and Y_{rms} is the riser vibration root-mean-square amplitude measured at the antinode of vibration. Refinements to (2.77) are available from [16]:

$$\frac{C_d}{C_{d0}} = 1 + 0.355 \left(\frac{2Y_{rms}}{D} \right)^{0.9} \tag{2.78}$$

and from [17]:

$$\frac{C_d}{C_{d0}} = 1 + 2.3 \left(\frac{\sigma_y}{D} \right) + 1.7 \left(\frac{\sigma_y}{D} \right)^2 \tag{2.79}$$

where σ_y is the standard deviation of cross-flow displacement. Some recent studies claim this equation overestimates the drag amplification [16] but since the older equation was obtained at more reasonable physical similarity rules (aspect ratio D/L and subcritical Reynolds number) the older equation was used. In order to track the equivalent cross-flow root mean square deflection, Y_{rms}, the component of node velocity in the cross-flow direction was integrated through time. A low-frequency drift filter was applied to the result and details on implementation can be seen in Appendix D. This produced a sinusoidal displacement signal which provides the Y_{rms} value.

Since the VIV force is evaluated at each element based on local velocities and accelerations, the model is naturally suited to simulating large systems which undergo significant deflections and structural property changes. Such systems include large aspect ratio marine risers, marine mooring cables, and towed or remotely operated vehicles.

Chapter 3

Calibration and Validation

In Chapter 2, the nature of the wake oscillator model was quantified with equations (2.72) through (2.74). The wake oscillator was shown to use a differential equation that dictates the time domain evolution of the riser lift coefficient, with the resulting lift force applied in the cross-flow direction. However, the Van der Pol parameters must be set to reflect the VIV response of the testbed riser.

In this Chapter the calibration and validation of the variable buoyancy and VIV modules are described. For the variable buoyancy model, validation with analytical results and mesh convergence tests are completed to characterise the behaviour of the algorithm. The VIV model is calibrated with experimental data from the literature and validated with additional experimental and numerical data available from the literature.

3.1 Variable Buoyancy Validation

The variable buoyancy module will be used to drive the motion of the surface barge. As described in section 2.3.1, the surface barge is approximated as a rectangular prism and so the module is tested with similar simple geometries: cube, sphere,

and cylinder. An arbitrary quantity used for analysis is the buoyant product, which is defined as the product of magnitudes of buoyant force and location of center of buoyancy. The buoyant product is used for analysis because it tests the convergence of both the buoyant force and the location of center of buoyancy simultaneously.

The accuracy of the algorithm is tested by comparing the buoyant product to known theoretical values for geometric shapes with the same characteristic dimensions. Next, the convergence of the algorithm is tested by examining the buoyant product of bodies with random Euler angle orientation in a noisy ocean surface. Finally, a nondimensionalised study of the most problematic geometry is completed to clarify the limitations of the algorithm.

3.1.1 Buoyancy Product Accuracy

In order to characterise the performance of the variable buoyancy algorithm, three simple shapes in various orientations were examined: cube, cylinder, and sphere.

In all three cases, the Euler angles were set to 0, the same characteristic dimension magnitudes were applied, and the object was 50 % submerged in salt water with no ocean waves present. Figure 3.1 clearly shows convergence as the number of volume cells that represent the body (mesh density) is increased. Because the volume cells are square, there is no mismatch for such a simple orientation for the square body shape and the buoyant product shows extremely small constant error.

3.1.2 Buoyant Product Convergence

Euler angles of $\psi = 0$, $\theta = 27$, and $\phi = 7$ degrees were selected for the convergence analysis. New percentage error plots, seen in Figure 3.2, were generated using the buoyant product. The converged value used showed less than 0.02% change with increasing mesh density. Similar characteristics were observed as in Figure 3.1: the

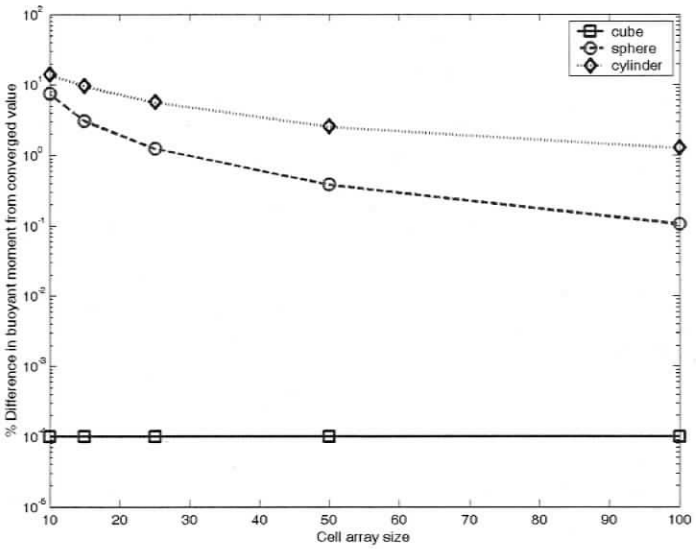

Figure 3.1: Buoyancy product error from known value.

cube shape showed the quickest convergence while the cylinder shape exhibited the slowest convergence.

It is intuitive that the cube results converged the fastest since the volume cells are square in shape and cause little mismatch when calculating the volume of the body. In addition, the cube results also show that the error in approximating the sea surface with rectangular volume cells is quickly dissipated. One reason the cylinder values converged the slowest is the error induced by approximating a circular cross-section with square volume cells is extruded along the submerged segment, which is visualised in Figure 3.3. The error extrusion explains why the sphere performs better than the cylinder but not as well as the cube: the sphere does not have long sides over which the error accumulates as with the cylinder as demonstrated in Figure 3.3.

To further characterise the cylinder error, the same Euler angles were kept but the aspect ratio, or slenderness ratio $\frac{H}{D}$, of the cylinder was varied. For each ratio $\frac{H}{D}$, three sets of different dimensions H and D were selected and studied for a variety of mesh densities. For each mesh density, the three sets of H and D values produced

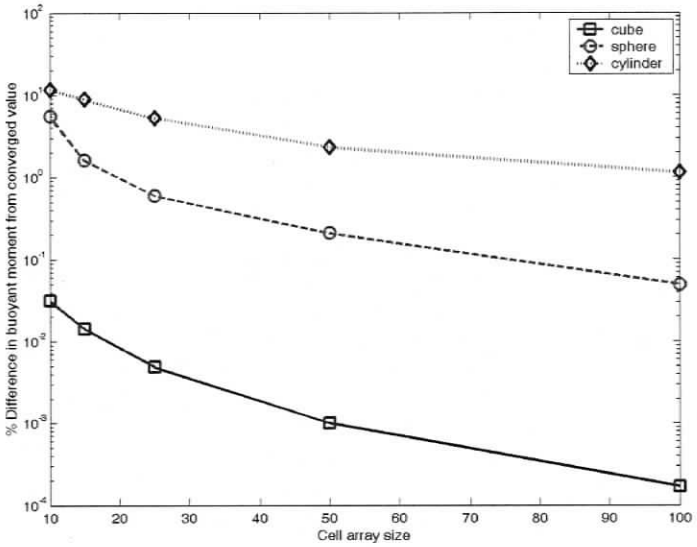

Figure 3.2: Buoyancy product error from converged values. The error was determined by comparing the buoyant product to a value obtained from a mesh that gave a convergence tolerance of 0.02 %.

three convergence error values and so the average quantity was used to represent the convergence error for the particular $\frac{H}{D}$. Figure 3.4 shows that convergence of buoyancy force is faster for squat cylinders (small $\frac{H}{D}$) than of narrow cylinders (large $\frac{H}{D}$), which reinforces the theory that the cylindrical error is due to extrusion or accumulation of the cross section error seen in Figure 3.4. This is because the error extruded for a slender cylinder is a larger fraction of total submerged volume than for a squat cylinder.

3.2 Vortex Induced Vibration Module Validation

The VIV module is intended for use in predicting a high aspect ratio ($\frac{L}{D} \approx 6000$) slender structure response in the subcritical Reynolds number range. There are three important physical response characteristics to compare: amplitude, frequency, and mode shape. Data from [52] was selected to calibrate the VIV model since the

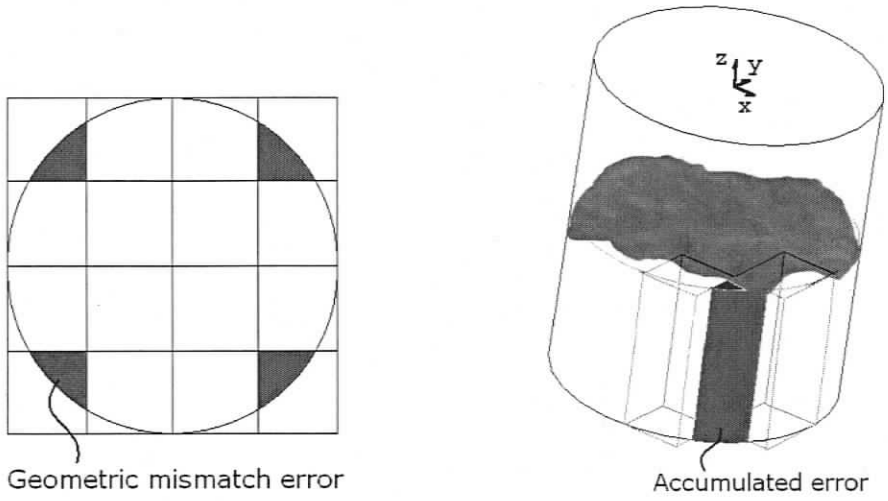

Figure 3.3: Cylinder error: (a) introduced by approximating a circular section with square segments (b) error extruded along the length of the cylinder.

Reynolds number and aspect ratio of the experiments were closest to the testbed riser. Table 3.1 outlines the aspect ratios and Reynolds numbers for fresh water experiments described in published works. Note that the Reynolds numbers from all sources were recalculated using maximum current speeds and the kinematic viscosity of seawater: $\nu = 1.8\text{E-}6\ \frac{m^2}{s}$.

Table 3.1: Physical similarity values for various simulations and experiments

Source	Re	L/D
Testbed Riser	1.6E5	4.8E3
[52]	3.8E4	1.4E3
[16]	1.0E3	4.0E2
[17,30]	1.6E4	4.7E2
[53]	1.3E5	4.8E2

Not all structural stiffness values used in the simulator were provided in [16, 17, 30, 52, 53]. Derivation of the remaining structural properties required for emulation with the VIV simulator is provided in Appendix E.

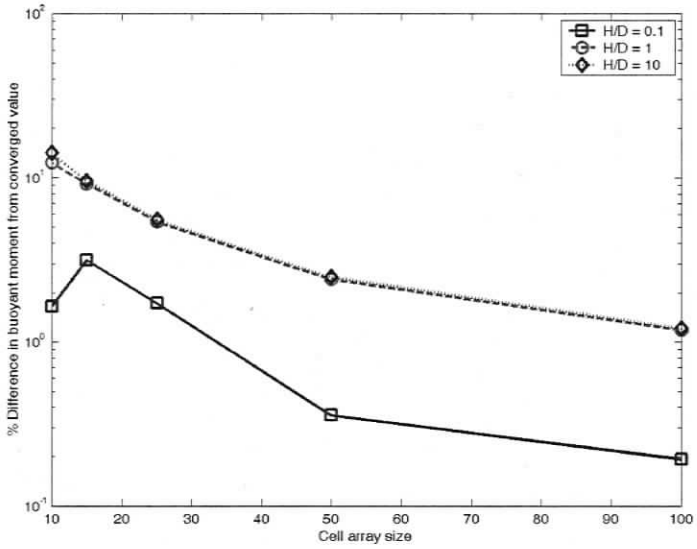

Figure 3.4: Buoyancy product error from converged value

3.2.1 Calibration with Uniform Current

The experimental setup of [52] can be seen in Figure 3.5. The experiment included a mechanism to ensure the tension in the riser was maintained in the range of 4000 N to 6000 N. To mimic this behaviour in the numerical simulation, the risers were pretensioned by displacing the supports until a tension of approximately 5000 N was reached for each current considered. In addition, the drag coefficient amplification described by equation (2.77) was deactivated since the tension was actively controlled during the real experiment. The supports used moment-free universal joints. Finally, in order to ensure rapid wake oscillator VIV initiation, a small cross-flow deflection of less than $0.05D$ was added to the initial conditions of the riser orientation. Experiment parameters can be seen in Table 3.2.

In order to tune the wake oscillator coefficients, A and ϵ, many simulations were executed with different coefficient values. After the structure had reached a steady state vibration, temporal standard deviation measurements were made from the cross-flow vibration amplitude at each node in the finite element mesh:

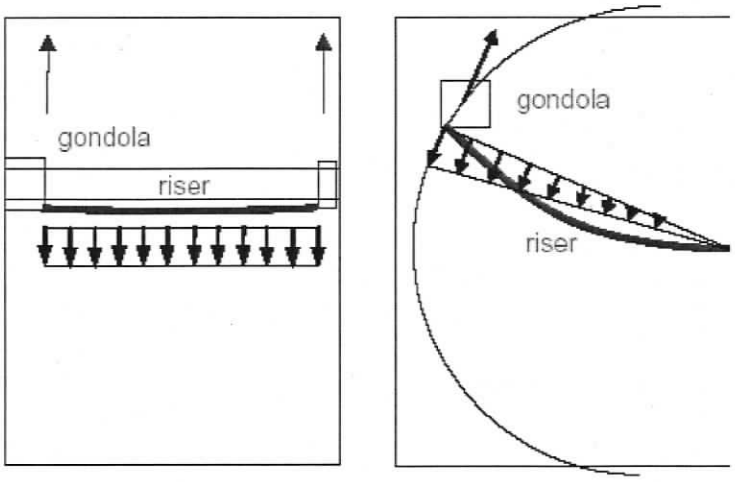

Figure 3.5: Uniform and linear current experiment setup [52]

Table 3.2: Simulation values extracted from [52]

Parameter	Value
fluid density ρ_w	$1025\frac{kg}{m^3}$
riser density ρ_r	$1640\frac{kg}{m^3}$
riser diameter D	$0.027m$
riser length L	$38m$
drag coefficient C_d	1.05
EA	$8.2e6N$
EI	$6.0e2Nm^2$
GJ	$4.0e2Nm^2$

$$\sigma_{VIV}^{(i)} = \frac{1}{T}\int_t \left[\left(\boldsymbol{r}(s^{(i)},t) - \boldsymbol{r}(s^{(i)})_{mean}\right)\cdot \hat{\boldsymbol{y}}_{VIV}\right] dt \tag{3.1}$$

where T is the length of sample time and $\sigma_{VIV}^{(i)}$ and $\boldsymbol{r}(s^{(i)})_{mean}$ are the temporal standard deviation of cross-flow displacement and temporal mean of displacement at node i of the finite element mesh, respectively. The mean and maximum values of σ_{VIV} along the entire span of the riser were then compared to the experimentally derived values. Figure 3.6 displays a sample simulation time history of cross-flow displacement at a discrete spot 10 m along the riser. The high frequency of vibration of the scale model riser resulted in slow simulations: 750 seconds of execution time

was needed for 1 simulated second. For a single simulation, the only two numbers produced were the spatial mean and maximum of σ_{VIV}, and hence several simulations were needed in order to judge how changes in A and ϵ affected the VIV model's accuracy with respect to the results of [52]. Tuning the wake oscillator coefficients was easier with the uniform current than with the shear current because the shear currents permit multimodal responses. For the multimodal responses, the spatial mean and maximum of σ_{VIV} are not descriptive enough to permit a direct comparison between the experimental and simulation results.

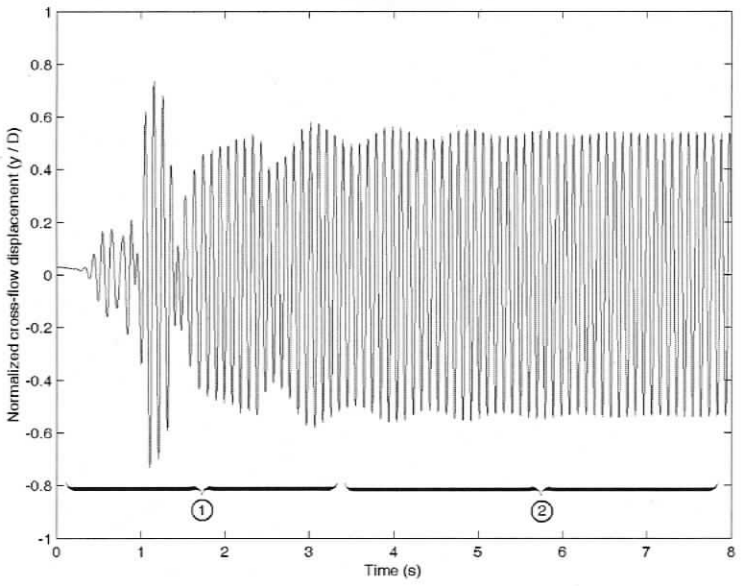

Figure 3.6: Dynamic cross-flow direction response at $s = 10m$. Phase (1): transient wake oscillator response to initial conditions of simulation. Phase (2): steady dynamic state of lock-in is reached. Analysis of vibration frequency, amplitude, and other properties are always done in phase (2) to match the original experiment process.

The final values selected for the coefficients were 20 and 0.1 for A and ϵ, respectively. These values provide a VIV response that approaches the upper range of the experimental data spread. Figures 3.7 and 3.8 display the numerical simulation values for three finite element mesh densities superimposed on the experimental data range provided in [52].

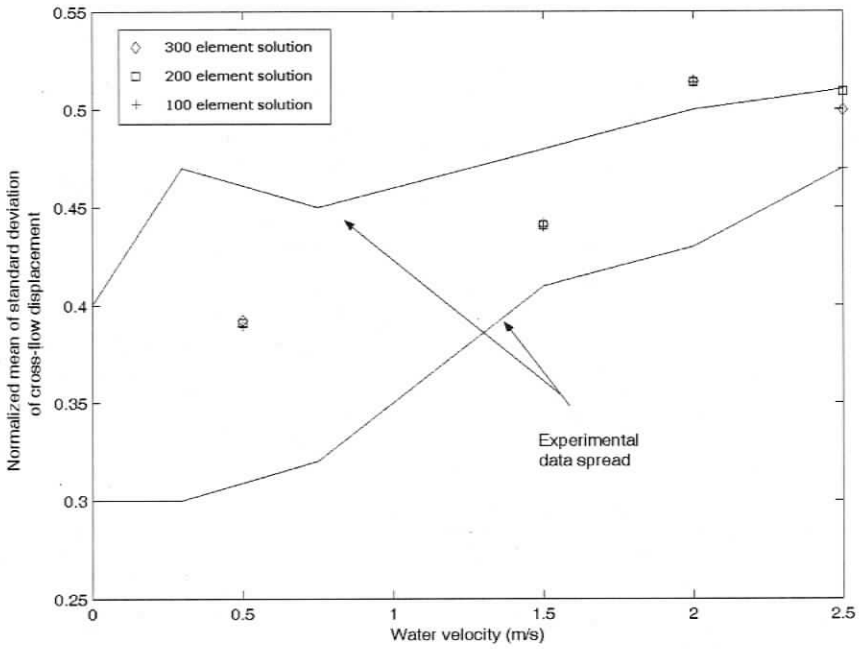

Figure 3.7: Uniform current: measured mean values of temporal standard deviation of cross-flow displacement from experimental setup [52]

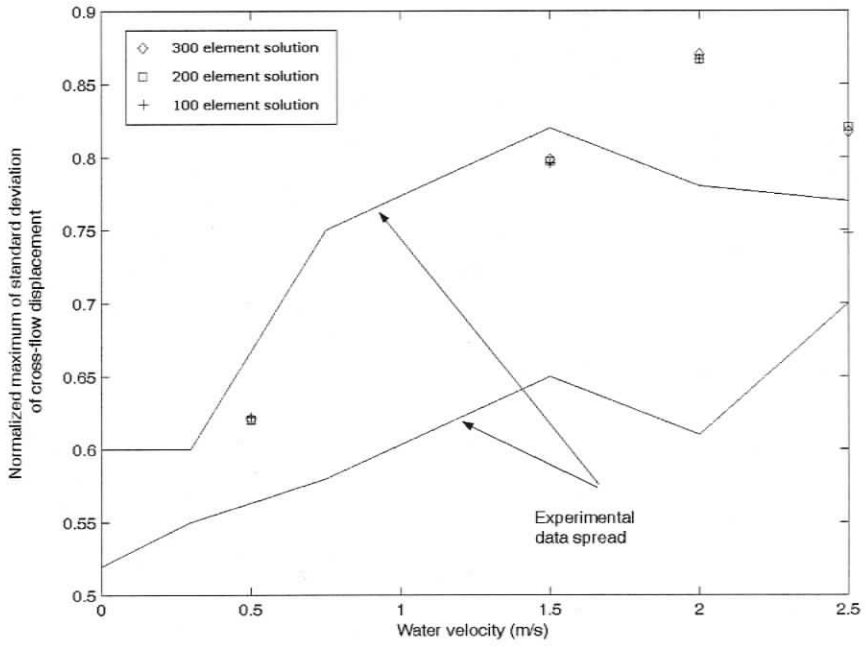

Figure 3.8: Uniform current: measured maximum values of temporal standard deviation of cross-flow displacement from experimental setup [52]

The cross-flow vibration envelope swept out by the riser for $0.5\frac{m}{s}$ and $1.5\frac{m}{s}$ flow can be seen in Figures 3.9 and 3.10. Each plot shows evidence that the structure is vibrating at a higher mode of vibration as the water velocity, and thus vortex shedding frequency as governed by the Strouhal relationship in equation (1.3), increases. In addition, the spanwise asymmetric vibration amplitude was observed in the original experiment. Further analysis revealed the cross-flow displacement and lift coefficient frequencies were the same at each point along the span and can deviate slightly from equation (1.3). This shows that the wake oscillator mimics the lock-in phenomenon that was shown in Figure 1.7. The reduced velocity, calculated from equation (1.5), for each case is within the expected range of values of 4 and 7 [10,53] for the steady state VIV response. The reduced velocity and the vibration frequencies that were observed in the simulation and the experiment of [52] are listed in Table 3.3. Also shown in Table 3.3 is the nearest structural natural frequency to the vibration frequency, f_{ex}. This natural frequency is calculated from equation (1.9). The dominant mode of vibration produced by the simulation and experiment and the nearest mode predicted by equation (1.9) can be seen in Table 3.4. In all instances, the simulator produced higher modes and vibration curvatures than in the experiment. This behaviour may be an impact of using wake oscillator coefficients that produced the highest structure response from the experimental data scatter. In addition, the error seems to increase with vibration frequency. Referring back to section 1.2, structural damping acts to decrease the amplitude of the VIV response, and hence the errors observed here could be due to the lack of a damping model within the flexural dynamics of the riser.

3.2.2 Validation with Shear Current

The coefficients A and ϵ for the wake oscillator were selected in section 3.2.1. In order to better understand the response of the model to different environment conditions such as current profiles and riser properties, several simulations examined.

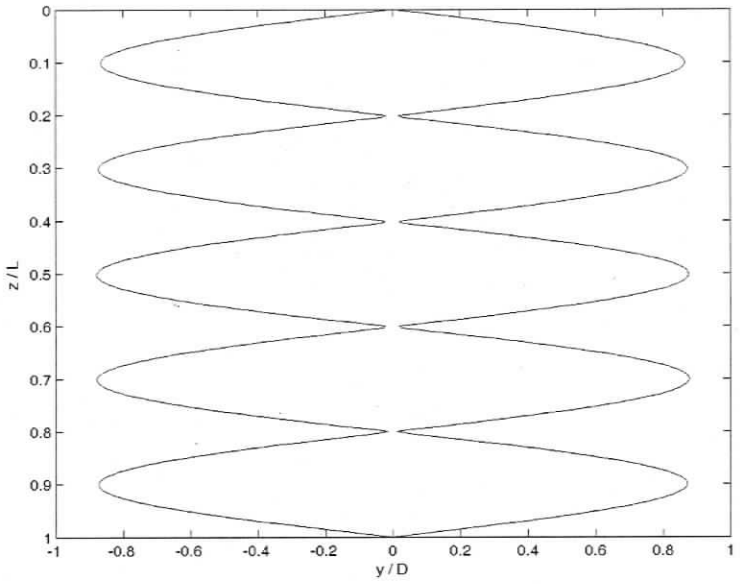

Figure 3.9: Uniform current: simulated vibration envelope at $0.5\frac{m}{s}$. The vertical axis is distance along the riser normalised by riser length L, while the horizontal axis is cross-flow vibration amplitude normalised by riser diameter D. Vibration mode appears to be 5.

Table 3.3: Comparison of simulated, experimental, and theoretical vibration frequencies for VIV with a uniform current profile. In the last column, f_n is the nearest natural frequency to f_{ex} found by adjusting the mode number n in equation (1.9).

V_{rel} $\frac{m}{s}$	V_r	f_{ex} (Hz)	exp. f (Hz)	f_n eq.(1.9) (Hz)
0.5	5.1	3.64	3.0	3.87
1.5	5.1	10.9	8.5	11.1
2.0	5.6	13.3	11	13.3
2.5	5.5	17.1	13	16.9

Table 3.4: Comparison of simulated, experimental, and theoretical mode numbers for VIV with a uniform current profile

V_{rel} $\frac{m}{s}$	sim. mode	exp. mode	mode eq.(1.9)
0.5	5	4	4
1.5	11	9	11
2.0	15	11	13
2.5	17	13	16

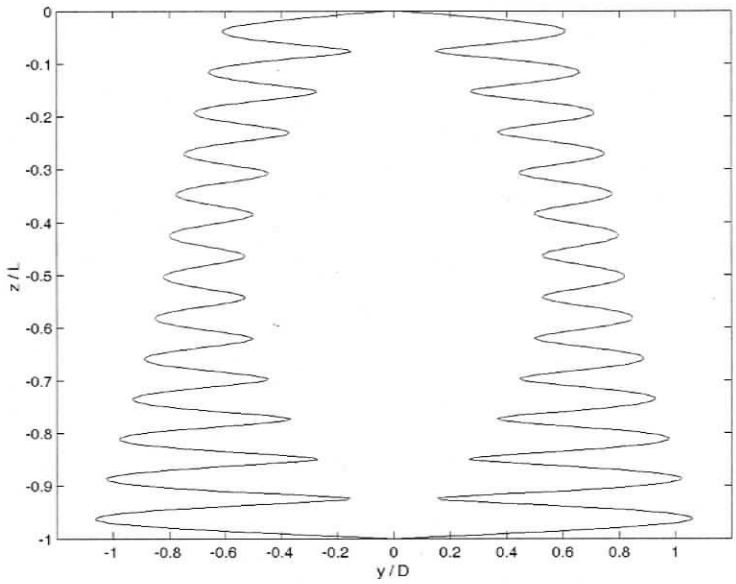

Figure 3.10: Uniform current: simulated vibration envelope at $1.5\frac{m}{s}$. Vibration mode appears to be 13. Asymmetric spanwise vibration envelope has been observed in experimental data.

In this section, a linear shear current with 100% reduction of water velocity over the length of the riser was used with experimental data provided by [52]. The experimental setup can be seen in Figure 3.5: rotation of the gondola platform produced the shear current over the riser. Again, to mimic the tension control of the experiment, the simulation did not use drag coefficient amplification as prescribed by equation (2.77). As expected, the vibration amplitude observed in the shear current simulations was significantly less than in the uniform current case. Comparison of the mean and maximum temporal standard deviations can be seen in Figures 3.11 and 3.12. The behaviour of the wake oscillator model is qualitatively correct: in the amplitude of the VIV response, the simulation shows more attenuation than the experimental results.

Simulations were completed to compare the vibration envelope reduction at various reductions of maximum velocity, including 100%, 90%, 66%, and 15% reduction

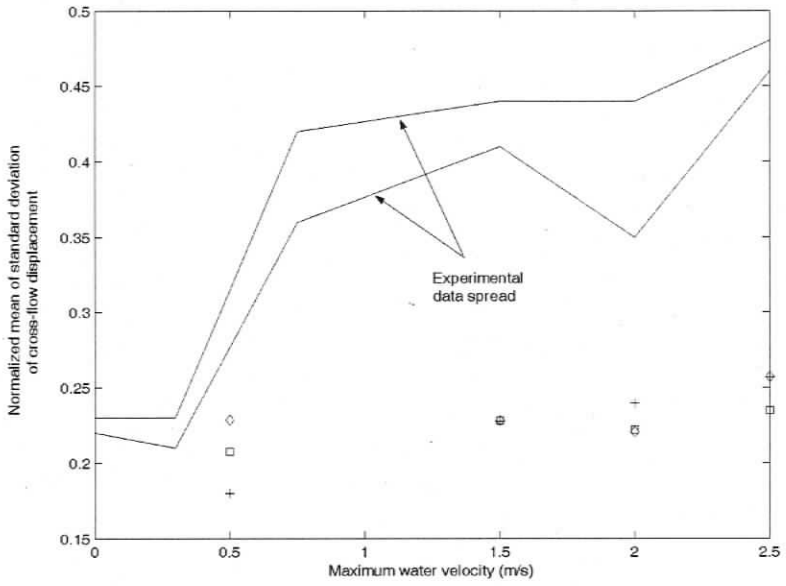

Figure 3.11: Sheared current: measured mean values of temporal standard deviation of cross-flow displacement from experimental setup [52]

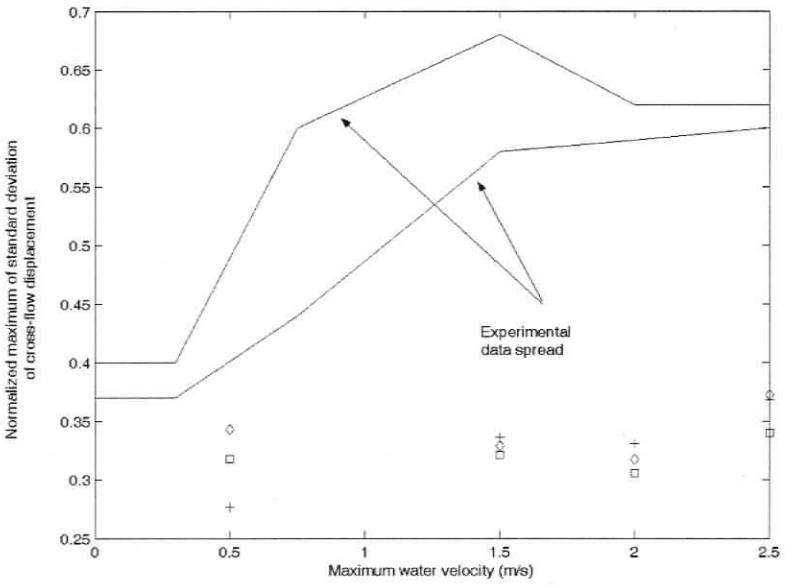

Figure 3.12: Sheared current: measured maximum values of temporal standard deviation of cross-flow displacement from experimental setup [52]

Table 3.5: Comparison of simulated, experimental, and theoretical vibration frequencies for VIV with a shear current profile

$V_{max}\frac{m}{s}$	V_r	f_{ex} (Hz)	exp. f (Hz)	f_n eq.(1.9) (Hz)
0.5	6.0	3.10	2.5	2.90
1.5	5.6	10.0	7.5	10.0
2.0	5.4	13.8	9.5	13.3
2.5	5.6	16.4	11	16.9

Table 3.6: Comparison of simulated, experimental, and theoretical mode numbers for VIV with a shear current profile

$V_{max}\frac{m}{s}$	sim. mode	exp. mode	mode eq.(1.9)
0.5	4	3	3
1.5	10	10	10
2.0	11	12	13
2.5	12	14	16

of the maximum velocity over the riser span. Figure 3.13 illustrates three current profiles with 0%, 50%, and 100% shear. The vibration envelope for the different shear current profiles can be seen in Figures 3.14 and 3.15. The vibration envelope shows a significant reduction in amplitude. In addition, the larger shear in the current results in a lower stimulated mode, which is qualitatively consistent with the results from [52]. The simulation of a lower mode by a sheared current is intuitive since the vortex shedding is less correlated along the span of the riser which results in weaker forcing. However, without appropriately tuning the coefficients, the wake oscillator model should be used with only small deviations from a uniform current.

3.2.3 Validation with Uniform Current

The existing literature provided data from a numerical simulation which used a 3D finite element structural model and the discrete vortex method (DVM) to model VIV response [53]. The simulation was recreated with the same physical parameters in order to observe any major discrepancies. The simulation setup can be seen in Figure 3.16. In the original work, the top 17% of the riser penetrated the water surface, but

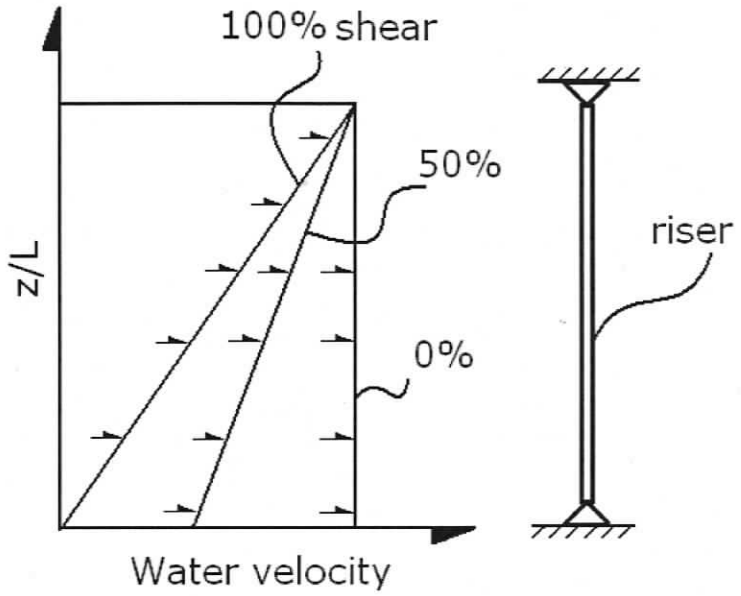

Figure 3.13: Variation in shear of water velocity profile

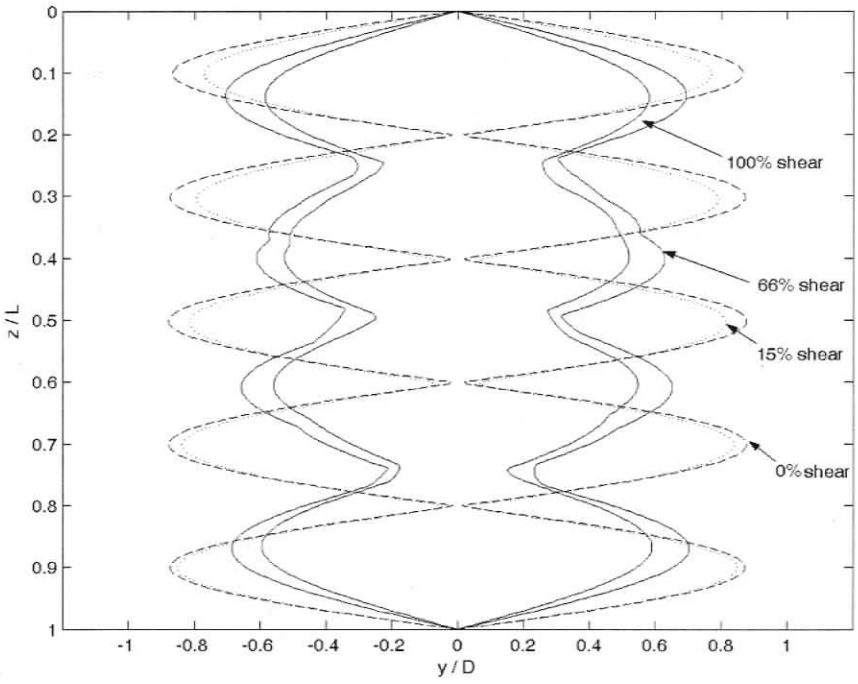

Figure 3.14: Shear current: simulated vibration envelopes with maximum water velocity at $0.5\frac{m}{s}$

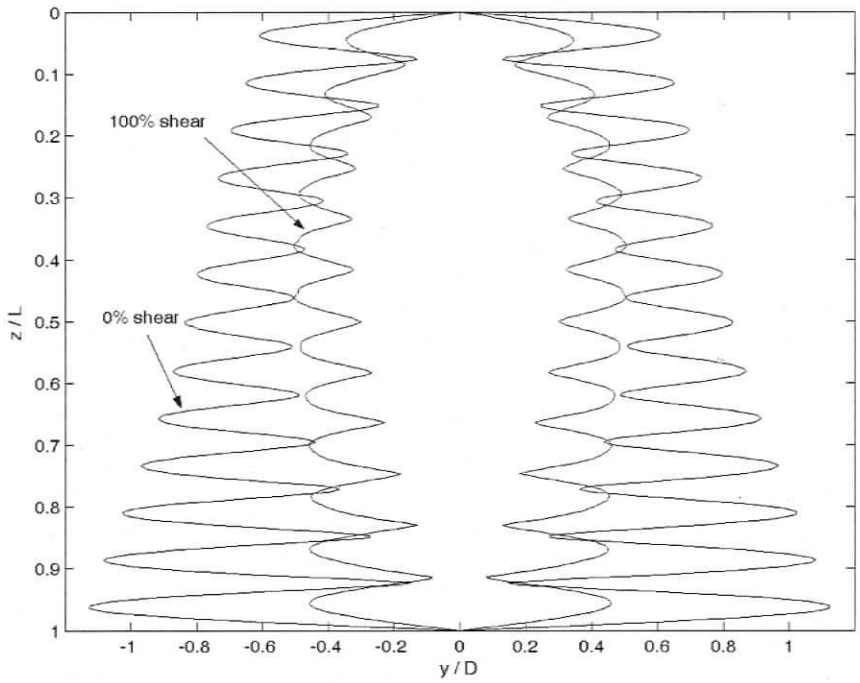

Figure 3.15: Shear current: simulated vibration envelopes with maximum water velocity at $1.5\frac{m}{s}$

in the reconstructed simulation the entire riser was submerged to ensure reliable wake oscillator performance in light of the results from section 3.2.2.

The physical parameters for the simulation can be seen in Table 3.7. Young's modulus and the riser geometry were provided in [53] and the remaining parameters were evaluated in Appendix E using these specified values. Pinned boundary conditions were used and a comparison of results can be seen in Table 3.8.

The results compiled in Table 3.8 show good agreement in vibration mode although there are discrepancies in the calculated reduced velocity. In both the simulation cases, the reduced velocity was calculated using equation (1.5) and the frequency of the dominant structural vibration. Unfortunately, the data provided in [53] did not detail changes in the structural tension due to VIV even though the finite element stiffness matrix includes terms accounting for changes in tension. Table 3.9 shows the simulation's prediction of mean riser top tension.

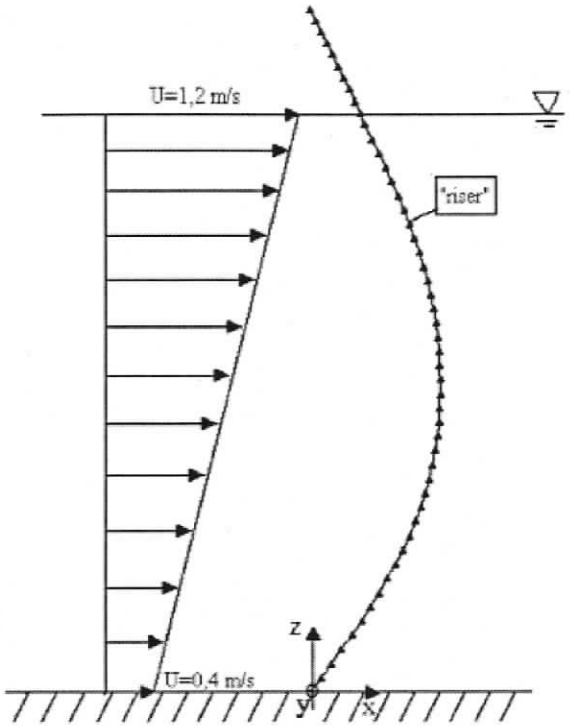

Figure 3.16: Uniform and linear current numerical experiment setup [53]

Table 3.7: Simulation and structural values extracted from [53]

Parameter	Value
fluid density ρ_w	$1025\frac{kg}{m^3}$
riser density ρ_r	$2757\frac{kg}{m^3}$
riser diameter D	$0.25m$
riser length L	$120m$
drag coefficient C_d	1.2
section modulii	
EA	$2.924e9N$
EI	$1.960e7Nm^2$
GJ	$1.493e7Nm^2$

Table 3.8: Results of uniform current experiments

$V\frac{m}{s}$	Mode	Mode [53]	V_r	V_r [53]	%difference
0.23	1	2	4.6	6.76	-32
0.38	2	2	5.8	4.87	20
0.54	3	3	4.5	4.00	12
0.85	3	4	5.2	4.03	29
0.93	3	4	5.4	4.4	24

Table 3.9: Top tension variation with current speed

$V\frac{m}{s}$	Top tension (N)
0.23	1.09e5
0.38	1.71e5
0.54	2.34e5
0.85	4.05e5
0.93	4.51e5

The riser top tension in [53] was given as 200 kN. Table 3.8 shows that for $V = 0.5\frac{m}{s}$, the simulated riser top tension is nearest to 200 kN (minimum difference of 17%), and the error in reduced velocity seen in Table 3.8 is minimal. Since only Young's modulus and dimensions of the riser were provided by the data, a possible source of error is a difference in structural parameters calculated (EI,EA,GJ). The finite element model used in this work is more complete than that used in [53] and the difference in structural model which includes torsion mechanics may influence the VIV response.

Chapter 4

Deep Sea Mining Riser Model

In this Chapter, the riser dynamics model, including the VIV calculations, is coupled with rigid body dynamics models of the dump valve and surface barge. The testbed riser system is discussed in detail in section 4.1. This includes the procedure used to produce the steady dynamic VIV in the testbed riser as well as discussion on the metric used to compare the performance of each testbed riser configuration. The results of a finite element mesh convergence test are presented in section 4.2. Simulations are run with various combinations of flex joints and buoyancy modules along the riser span. The results of the simulations incorporating flex joints are presented in section 4.3 and the results of simulations incorporating buoyancy modules are presented in section 4.4.

4.1 The Testbed Riser

The schematic of the complete system can be seen in Figure 1.15, which is shown again in Figure 4.1 for convenience. In order to simplify the model of the system, the excavator and connector hose were neglected. In addition, the slurry in the riser was assumed to be a static fluid column of constant density. The main objective is

to use the VIV simulator as a tool to evaluate the changes in fatigue damage when flex joints and buoyancy modules are introduced in the testbed riser.

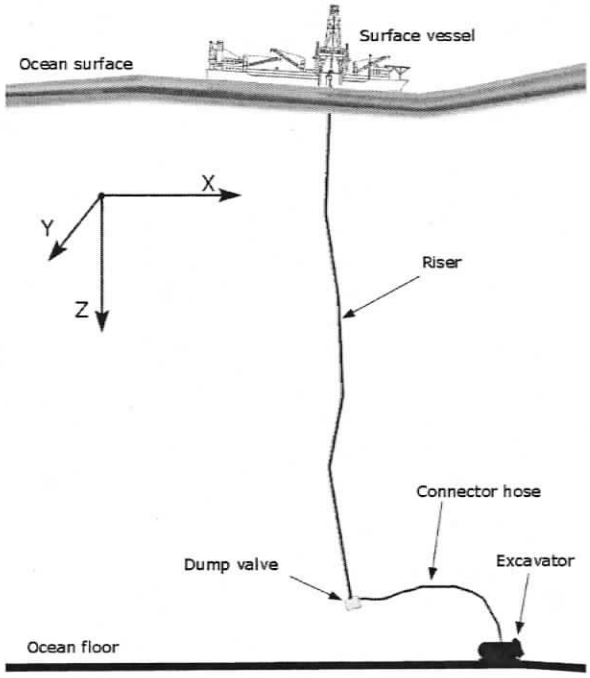

Figure 4.1: Deep water mining system. The excavator extracts material and minerals from the sea floor, which are transported up the connector hose, riser, and then to the surface vessel for storage, processing, and transport. The dump valve at the bottom of the riser serves to eject excess material back to the ocean floor.

The simulation combines the riser model of section 2.3.2 and two rigid body models, one for the surface barge and one for the dump valve, as described in 2.3.1.

Flex joints are introduced in the model to alter the structural natural frequency behaviour and help suppress the more damaging higher modes of vibration from appearing. Buoyancy modules are introduced to prevent the vortices from shedding at a uniform frequency along the testbed riser span thereby affect the vibration frequency. The metric used to compare the performance of the testbed riser is the safety factor, n_s, from fatigue failure. It is evaluated at each node in the testbed riser finite element mesh. Experiment parameters used in the simulations can be seen in Table 4.1. Since detailed information on the flex joint properties was limited, the bending stiff-

ness term EI for flex joint regions was reduced by roughly four orders of magnitude compared to the nominal riser bending stiffness.

Table 4.1: Simulation values for riser analysis

Parameter	Value
fluid density ρ_w	$1025\frac{kg}{m^3}$
riser density ρ_r	$1843\frac{kg}{m^3}$
riser diameter D	$0.3302m$
riser length L	$1600m$
riser drag coefficient C_d	1.2
section modulii	
EA	$2.534e9N$
EI	$3.198e7Nm^2$
GJ	$2.558e7Nm^2$

One current profile type with several magnitudes was used to study the riser VIV. Though limited current data for the region of operation was available, which can be seen in Figure 4.2, a worst-case scenario current profile was selected for use in the simulator. The worst-case analysis was selected to ensure conservative results as well as to help distinguish the dynamic responses of each testbed riser configuration. Preliminary simulations showed that a step current produced much higher modes of vibration in the riser than a completely uniform current. For this reason, a 1100 m deep step current was used for all simulations. An additional benefit is the step current is similar to the uniform current, so a more accurate response from the calibrated wake oscillator model can be expected than with a noisy or shear current profile (see section 3.2.2). In all cases, step current magnitudes of $0.5\frac{m}{s}$, $0.7\frac{m}{s}$, and $0.9\frac{m}{s}$ were used due to their ability to stimulate a wide range of modes of vibration in the riser.

In order to compare the performance of different testbed riser configurations, the von Mises stress (see Appendix F) was calculated at a point on the outer surface of the riser, which can be seen in Figure 4.3. This point endures the largest stress oscillations and so for each node in the finite element testbed riser mesh, the temporal von Mises stress profile was calculated with information provided by the simulation.

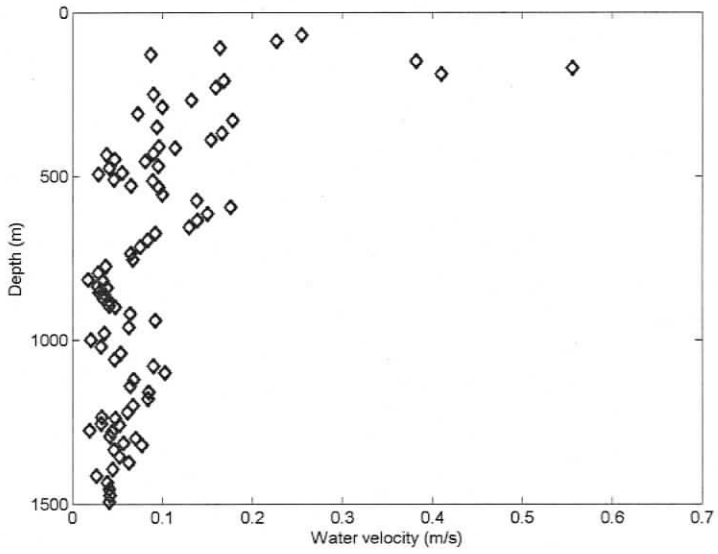

Figure 4.2: Data obtained on environment current velocities from the actual testbed riser operational environment. The current profile is quite noisy, but appears closest to a shear current. However, this profile was produced at one point in time and more data is needed for a reliable estimate of the profile's characteristics. In the work presented here, a conservative approach is adopted by using a worst-case analysis with a uniform current to 1100 m depth.

The temporal stress profile provides the mean and amplitude of von Mises stress, which is used in the modified Goodman diagram to calculate the safety factor, n_s, that guards against fatigue or yield failure with equations (2.10) and (2.12).

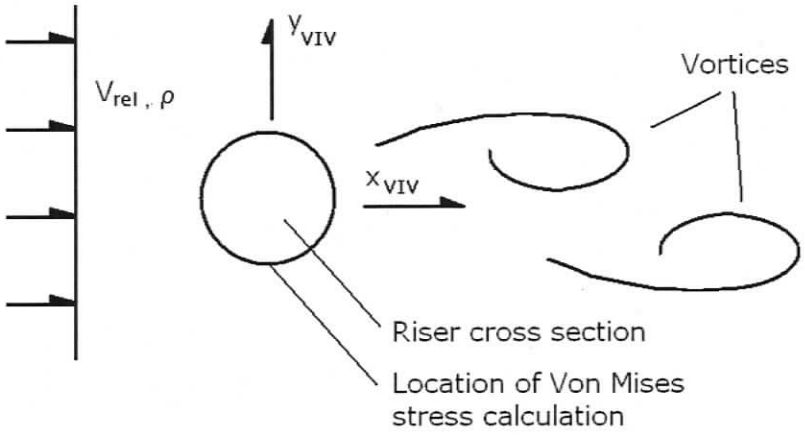

Figure 4.3: Location on the testbed riser where the von Mises stress is evaluated. The von Mises stress is evaluated at all nodes in the mesh of the riser. This point was selected as it is the location of maximum curvature oscillation and hence stress oscillation.

In order to approximate the stress amplitude in a simple manner, a linear relationship to the standard deviation is used:

$$\sigma_{amp} = \sqrt{2}\sigma_{SD} \tag{4.1}$$

whereby an observed temporal standard deviation of stress, σ_{SD}, is translated into an equivalent monotonic stress amplitude, σ_{amp}. The constant used in equation (4.1) provides the exact amplitude value if a perfectly sinusoidal function is present. The maximum stress value to be used in the failure criteria is therefore:

$$\sigma_{max} = \sigma_m + \sigma_{amp} \tag{4.2}$$

The position plots of the barge, dump valve, and initial and final riser positions from a simulation of 1000 s length in a $0.5\frac{m}{s}$ current with 15 s, 3 m high ocean waves

can be seen in Figure 4.4. The barge shows drifting introduced by the buoyancy force and moment that is ultimately dominated by the hydrodynamic load from the current. A sample temporal von Mises stress profile from a point 800 m along the testbed riser can be seen in Figure 4.5. The stress plot is quite different from an ideal sinusoidal function, which is a result of the transient effects of the drifting barge and ocean waves at the surface. To reduce the interference of these dynamic effects, the top of the riser was pinned at the ocean surface and the dump valve was approximated as a lumped mass. With dynamic effects from surface waves and surface vessel drift filtered out of the simulation, the impact of flex joints and buoyancy modules can be more easily observed. The von Mises stress profile 800 m along the span of the riser with the simplified model can be seen in Figure 4.6. Comparison of Figures 4.5 and 4.6 shows that the simplified model produces a much cleaner stress profile. In addition, the resulting n_s was calculated for each case and can be seen in Figure 4.7. Since the mean von Mises stress values seen in Figures 4.5 and 4.6 are within roughly 10% of each other, the difference in n_s values see in Figure 4.7 are due to the changes approximated stress amplitude: the simplified dynamics model produces a cleaner signal with lower standard of deviation than the full dynamics model. Furthermore, the n_s profile for the simplified dynamics model clearly indicates spatial oscillations along the span of the riser that result from the nature of the particular mode of vibration of the riser.

The cross-flow filtering response at 800 m along the riser from the special cross-flow coordinate can be seen in Figure 4.8. The unfiltered cross-flow displacement is produced by integrating the testbed riser velocity component in the cross-flow direction through time. The low-pass filter used to remove and drift from this process is presented in Appendix D and though some distortion is introduced by this process the resulting equivalent cross-flow displacement can be used for updating the drag coefficient via equation (2.77).

In all remaining simulations completed, the simplified dynamics model with pinned

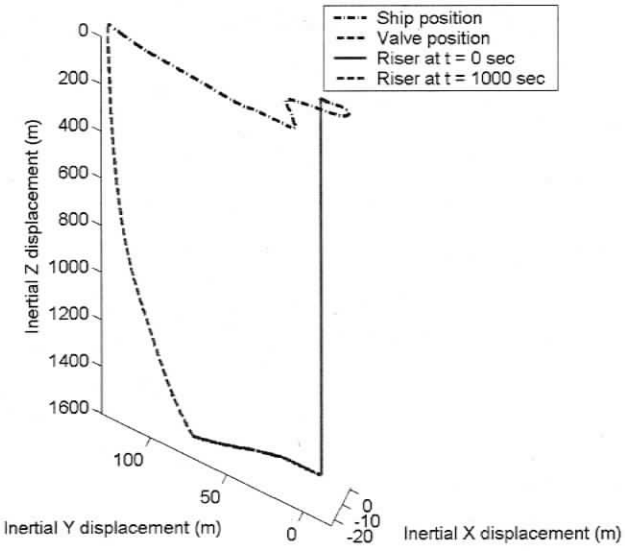

Figure 4.4: Position history of testbed riser

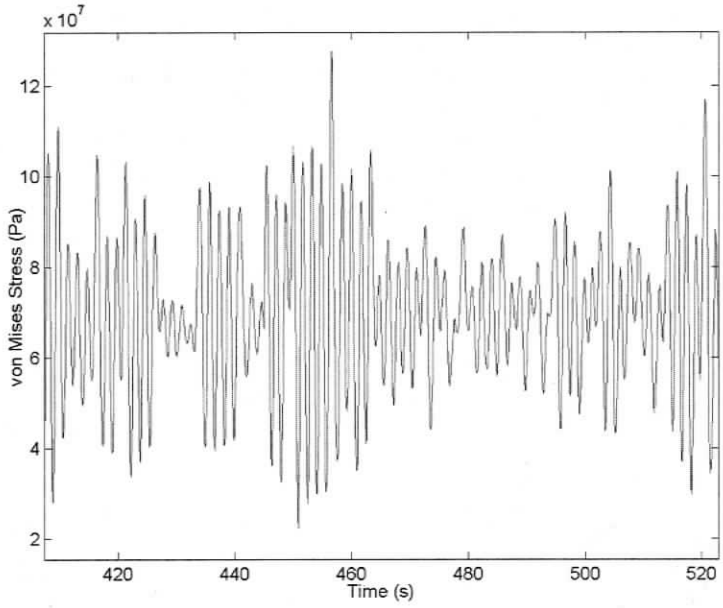

Figure 4.5: Temporal von Mises stress at 800 m along the testbed riser. This plot is from the testbed riser with rigid body surface vessel and dump valve models in a $0.5\frac{m}{s}$ current.

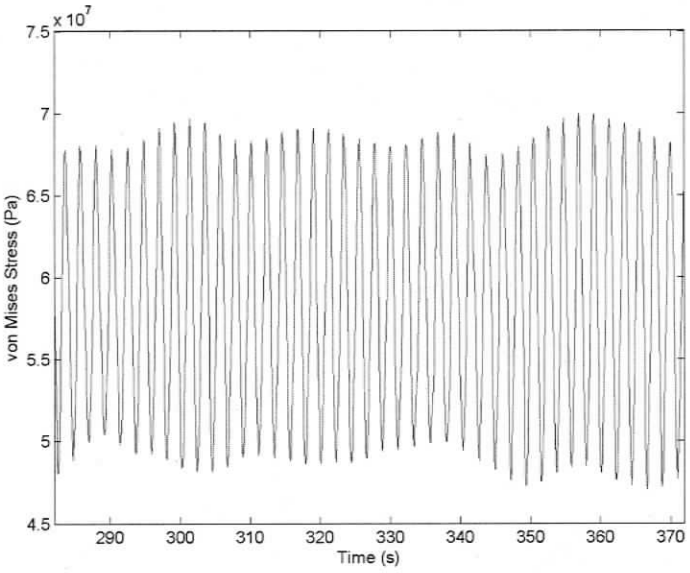

Figure 4.6: Temporal von Mises stress profile at a point 800 m along the simplified testbed riser. The plot is from the testbed riser with pinned surface boundary and a lumped mass representation of the dump valve in a $0.5\frac{m}{s}$ current.

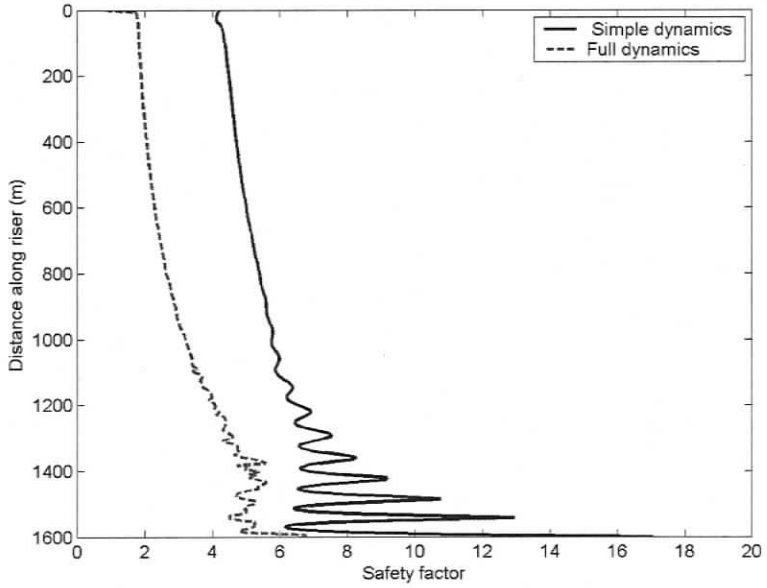

Figure 4.7: Safety factor comparison between simplified dynamics and full dynamics testbed riser system

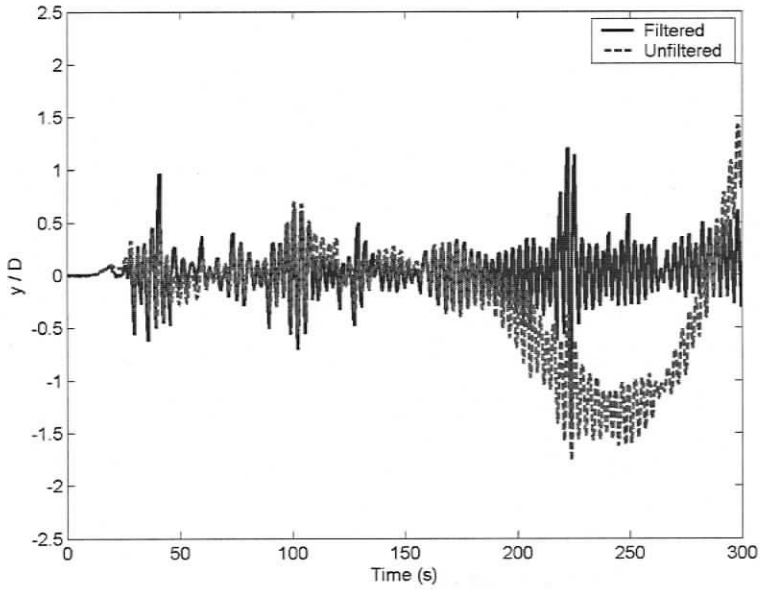

Figure 4.8: Approximated cross-flow direction displacement. The unfiltered response is extracted by integrating the component of testbed riser velocity in the cross-flow direction through time. The filtered results are produced from the use of the high-pass filter discussed in detail in Appendix D.

riser boundary condition at the top and lumped mass valve representation was used. To find the steady-state von Mises stress profiles for each current profile, the steady-state riser position was found for each water current profile with the VIV module deactivated. The VIV module is then activated and the measurements made on the resulting dynamic steady state response. This process was completed to reduce the transient behaviour of the riser as only the dynamic steady state VIV can be used for effective comparison of different riser configurations. Figures 4.9, 4.10 and 4.11 show the vibration envelope of the unmodified riser exposed to each current and illustrate higher modes of vibration stimulated at higher current velocities.

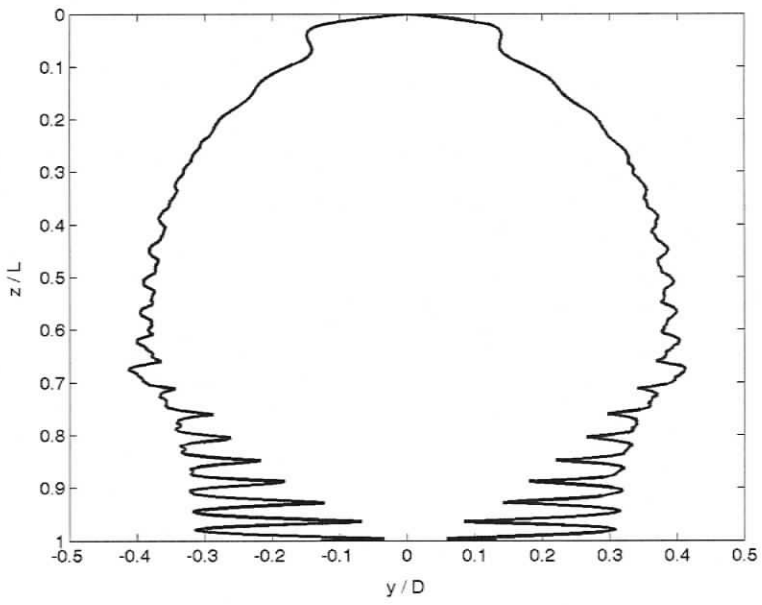

Figure 4.9: Vibration envelope of the unmodified testbed riser in a 1100 m deep 0.5 $\frac{m}{s}$ step current. An indication of the mode of vibration is the number of peaks in the vibration envelope.

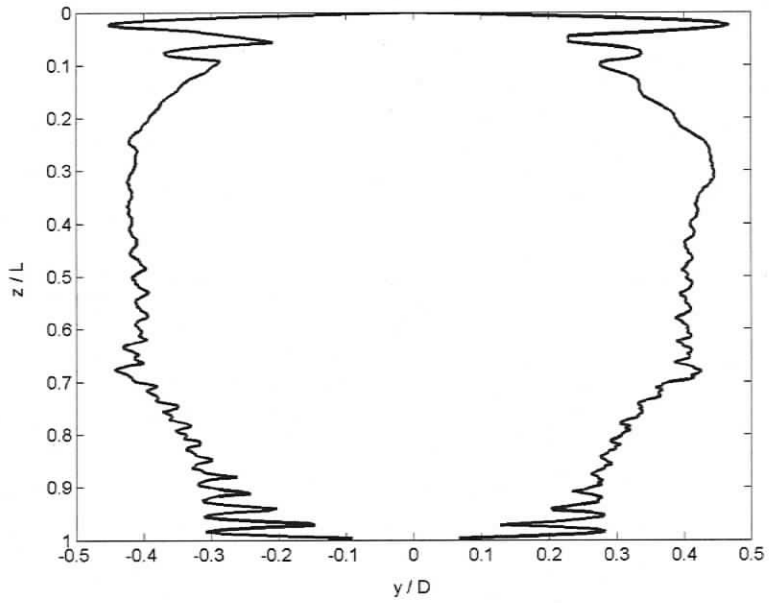

Figure 4.10: Vibration envelope of the unmodified testbed riser in a 1100 m deep 0.7 $\frac{m}{s}$ step current.

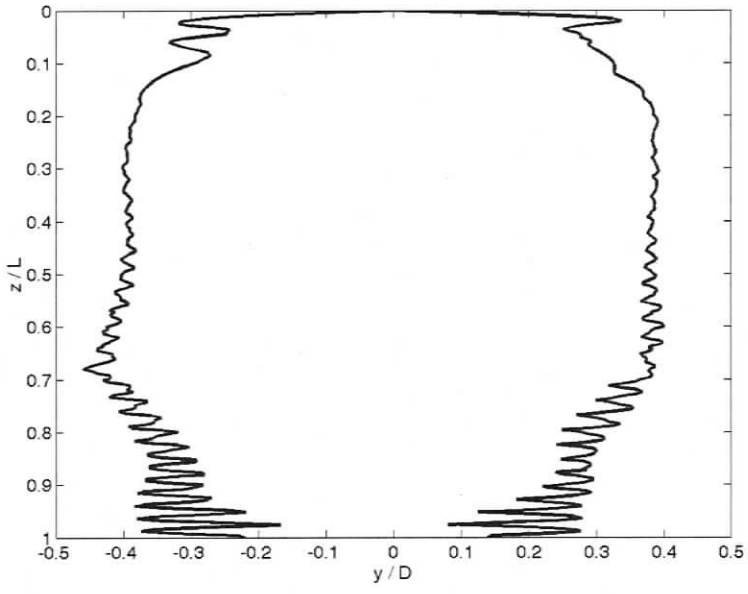

Figure 4.11: Vibration envelope of the unmodified testbed riser in a 1100 m deep 0.9 $\frac{m}{s}$ step current. The mode of vibration appears to be significantly higher than in the 0.5 $\frac{m}{s}$ case.

4.2 Mesh Convergence

A convergence study was conducted to determine the number of elements required to ensure the testbed riser mesh has minimal influence on the results of the simulator. Vortex induced vibration simulations of the testbed riser in currents of $0.1\frac{m}{s}$, $0.5\frac{m}{s}$, $0.9\frac{m}{s}$, and $1.5\frac{m}{s}$ were completed with 50, 100, 200, 225, and 250 elements. In section 3.2.1, the parameter $\sigma_{VIV}^{(i)}$ was introduced in equation (3.1) to help characterise the dynamic vibration behaviour of the riser. An similar term that uses the cross-flow component of curvature rather than cross-flow displacement is now introduced:

$$v_{VIV}^{(i)} = \frac{1}{T}\int_t \left[\left(\boldsymbol{r}''(s^{(i)},t) - \boldsymbol{r}''(s^{(i)})_{mean}\right)\cdot \hat{\boldsymbol{y}}_{VIV}\right] dt \tag{4.3}$$

where T is the sample time and $v_{VIV}^{(i)}$, $\boldsymbol{r}''(s^{(i)},t)$, and $\boldsymbol{r}''(s^{(i)})_{mean}$ are the standard deviation of curvature in the cross-flow direction, testbed riser curvature, and temporal mean curvature at node i in the riser finite element mesh, respectively. In addition to the mean of v_{VIV} and mean and maximum σ_{VIV} along the riser span, the mean top tension and vibration frequency were checked for convergence. The relative difference of these parameters between the 200 element and 100 element cases can be seen in Table 4.2 and between a 250 element and 225 element cases can be see in Table 4.3.

Table 4.2: Relative change in values from 100 to 200 element mesh

$V_{rel}\frac{m}{s}$	T_{mean} (%)	$mean\frac{\sigma_{VIV}}{D}$ (%)	$max\frac{\sigma_{VIV}}{D}$ (%)	$mean v_{VIV} D$ (%)	f_{ex} (%)
0.1	0.75	1.4	0.02	0.17	0.02
0.5	0.75	1.8	2.6	3.9	4.7
0.9	0.75	3.0	6.3	6.2	22
1.5	0.70	0.51	1.0	19	0.55

Table 4.2 shows that at lower current velocities, a mesh density of 100 elements is adequate. However, the curvature convergence indicates that as V_{rel} increases and higher modes of vibration and higher curvatures appear, more elements are required.

However, it is desirable to have a smaller number of elements as adding more elements considerably increases the execution time of the simulation. Since the parameters selected appear to fluctuate by only a few percent, Table 4.3 indicates using a 250 element mesh will be adequate for simulations while maintaining reasonable simulation execution time.

Table 4.3: Relative change in values from 225 to 250 element mesh

$V_{rel}\frac{m}{s}$	T_{mean} (%)	$mean\frac{\sigma_{VIV}}{D}$ (%)	$max\frac{\sigma_{VIV}}{D}$ (%)	$meanv_{VIV}D$ (%)	f_{ex} (%)
0.1	0.10	0.49	0.12	0.4	0.00
0.5	0.10	2.4	7.12	0.22	4.3
0.9	0.10	0.54	1.09	3.0	2.14
1.5	0.11	2.8	0.18	7.3	1.7

4.3 Flex Joint Results

Flex joints of 20 m length were placed in various locations on the riser. Testbed riser configurations include single flex joint installations and multiple flex joints placed at several distances along the riser:

1. 200 m
2. 1100 m
3. 1400 m
4. 1100 m and 1400 m
5. 1100 m, 1200 m, 1300 m, and 1400 m

Placement of flex joints is arbitrary. Most were placed near the bottom of the testbed riser because the lower local tension values facilitates greater influence on the vibration behaviour (see section 1.2.2 for more detail). The case with a flex joint placed at 200 m illustrates the diluted influence of bending stiffness changes due to the greater local tension at the 200 m location.

4.3.1 Upper Region Flex Joint

The safety factor, n_s, for the unmodified testbed riser case and 200 m flex joint riser for 0.5 $\frac{m}{s}$, 0.7 $\frac{m}{s}$, and 0.9 $\frac{m}{s}$ current profiles can be seen in Figures 4.12, 4.13, and 4.14, respectively.

The n_s profile for the each water velocity, V_{rel}, seen in Figures 4.12 - 4.14 show good correlation to the plain testbed riser. This was anticipated by equation (1.9) for two reasons. The flex joint was placed in a region of high tension, which dominates the nature of the natural frequency in that region of the riser.

Within the flex joint, the relatively small bending stiffness ensures that all curvature oscillations are eliminated from the von Mises stress. However, the mean stress value, which is due to tension, remains and this leads to a nonzero n_s value in the flex joint. The n_s value in the flex joint actually remains constant for each V_{rel} case, though its influence relative to the remainder of the n_s profile of the testbed riser appears to increase with increasing V_{rel}. This is because larger magnitude curvatures from higher modes of vibration contribute to amplifying the von Mises stress but do not affect the mean stress value.

Signs that higher modes are stimulated with larger current velocities are the increase in oscillation frequency, which can be seen in Table 4.4 as well as the increase in spatial fluctuation of n_s seen in Figures 4.12 - 4.14.

Table 4.4 also shows the reduced velocity, V_r, which in all cases is within the range of values predicted in section 1.2.

Table 4.4: Reduced velocity and difference in frequency of von Mises stress from plain testbed riser

$V_{rel}\frac{m}{s}$	V_r	f_{ex} (%)
0.5	5.4	4.0
0.7	5.9	0.73
0.9	6.0	5.5

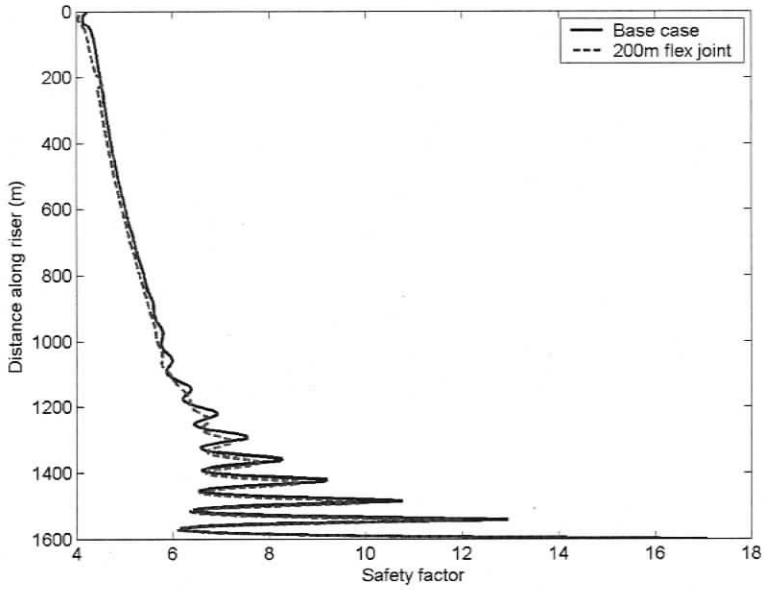

Figure 4.12: Upper region flex joint n_s for $0.5\frac{m}{s}$ step current. The presence of the flex joint locally increases n_s at 200 m along the riser. The remaining portion of the riser is very similar and well correlated to the base case n_s profile.

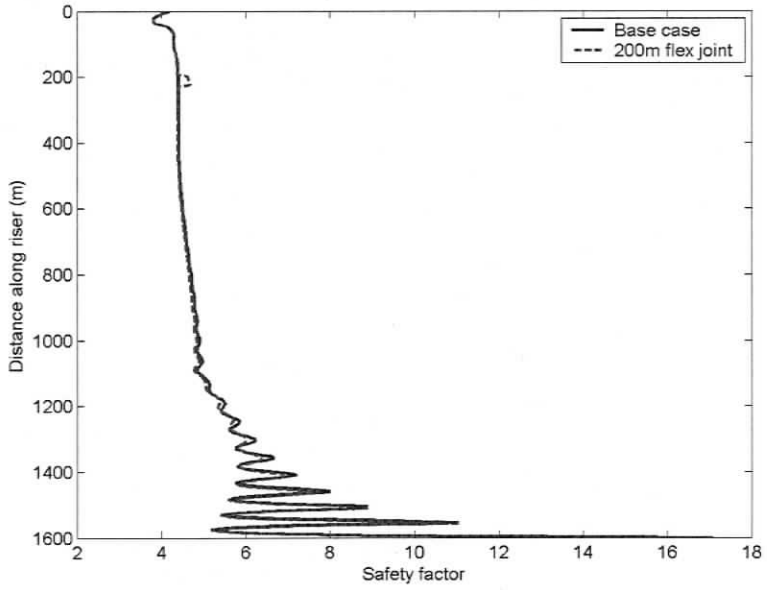

Figure 4.13: Upper region flex joint n_s for $0.7\frac{m}{s}$ step current. A higher mode of vibration is clearly present in the testbed riser due to the increase in spatial fluctuations of n_s along the span of the riser.

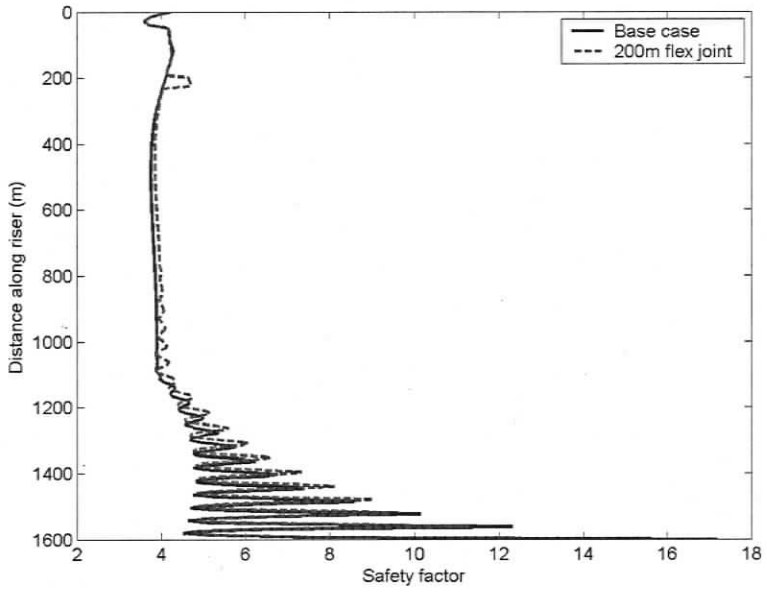

Figure 4.14: Upper region flex joint n_s induced by $0.9\frac{m}{s}$ step current

4.3.2 Lower Region Flex Joints: $0.5\frac{m}{s}$ Step Current

The n_s profiles for testbed risers with flex joints in the lower regions can be seen in Figures 4.15 - 4.18. As seen in section 4.3.1, The discontinuities in n_s along the span of the testbed riser indicate the location of the flex joints.

While n_s increases locally at each flex joint, the remaining regions along the testbed riser span seem to be unaffected as they correlated well with the unmodified riser results.

Table 4.5: Reduced velocity and difference in frequency of von Mises stress from plain testbed riser for each flex joint configuration at $0.5\frac{m}{s}$

Flex joints	V_r	f_{ex} (%)
1 (1100m)	5.6	0.4
1 (1400m)	5.4	4.0
2	5.7	1.0
4	5.7	1.0

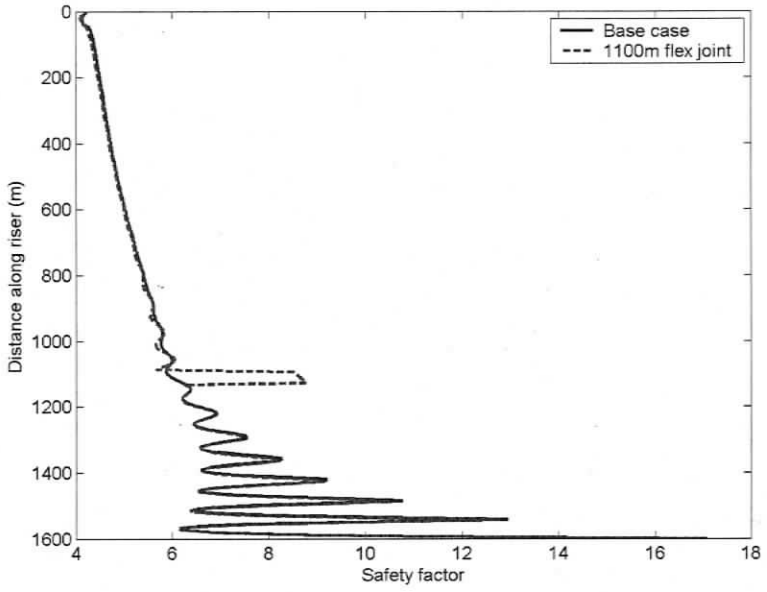

Figure 4.15: Testbed riser with flex joint at 1100 m n_s for $0.5\frac{m}{s}$ step current.

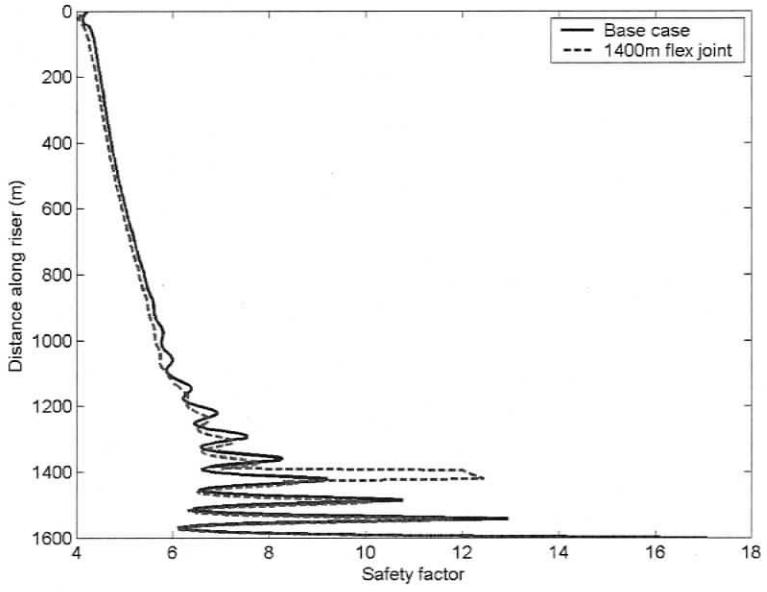

Figure 4.16: Testbed riser with flex joint at 1400 m n_s for $0.5\frac{m}{s}$ step current.

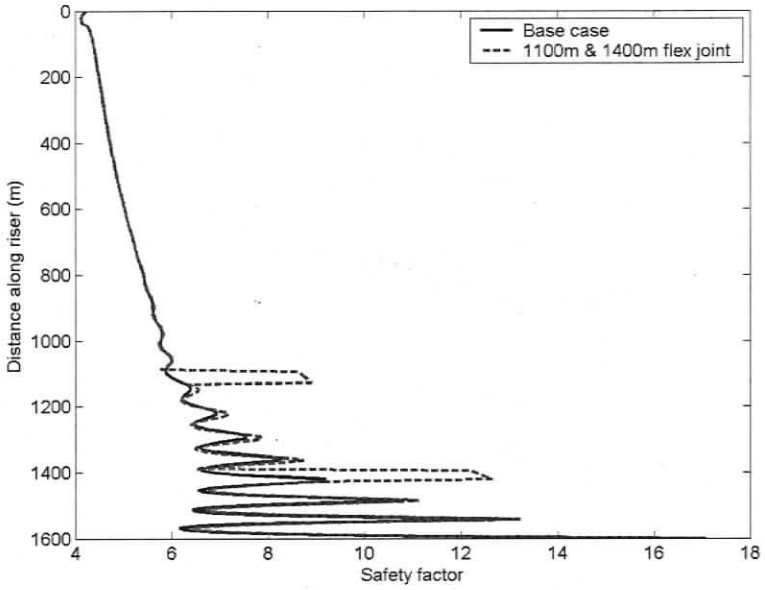

Figure 4.17: Testbed riser with flex joints at 1100 m and 1400 m n_s for $0.5\frac{m}{s}$ step current.

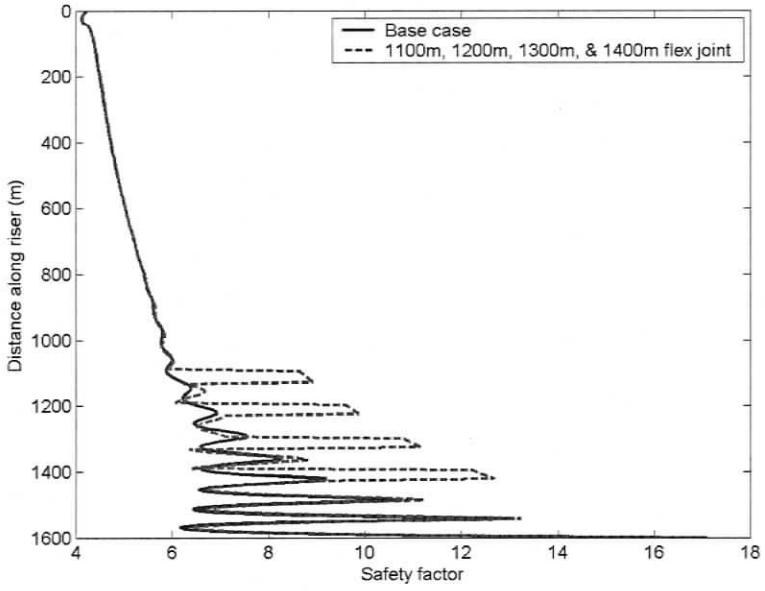

Figure 4.18: Testbed riser with flex joints at 1100 m, 1200 m, 1300 m, and 1400 m n_s for $0.5\frac{m}{s}$ step current.

4.3.3 Lower Region Flex Joints: $0.7\frac{m}{s}$ Step Current

Figures 4.19 - 4.22 illustrate the n_s profiles for the higher water current velocity. The results are similar to the $0.5\frac{m}{s}$ case in that the flex joints significantly increase n_s locally. As seen in section 4.3.1, the n_s value in the flex joints remains constant, while the remaining n_s profile decreases relatively. The remaining regions of the riser match the n_s profile of the unmodified riser, which indicates the flex joint influence is limited. The n_s profile of the testbed riser decreases because higher modes of vibration stimulate larger curvatures than in the $0.5\frac{m}{s}$ case.

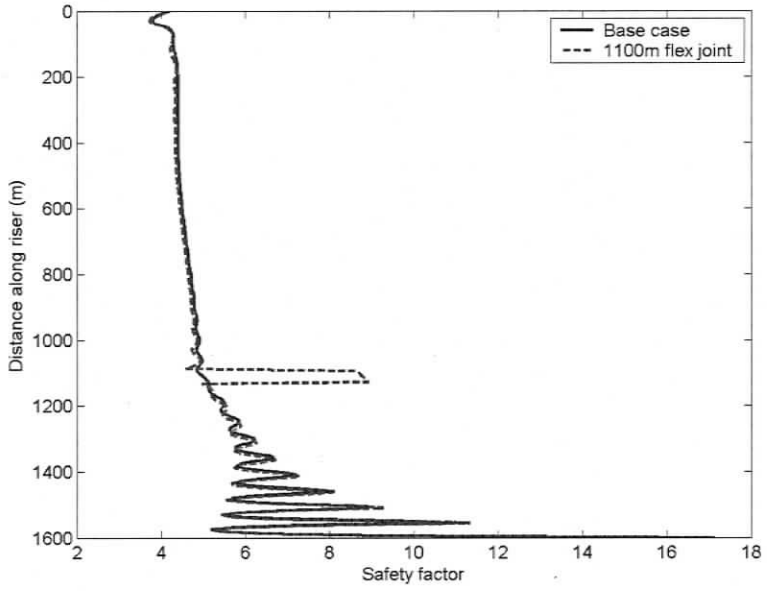

Figure 4.19: Testbed riser with flex joint at 1100 m n_s for $0.7\frac{m}{s}$ step current.

Frequency analysis of the testbed riser, compiled in Table 4.6, reveals in some cases smaller deviation from the unmodified riser than in the $0.5\frac{m}{s}$ step current case. Figure 4.21 shows significant increases in n_s in regions surrounding the flex joint. Though the vibration frequency has not significantly changed from the unmodified riser, it is possible a different mode of vibration is present in the riser. More examples of this phenomenon are presented and discussed in more detail with the higher current

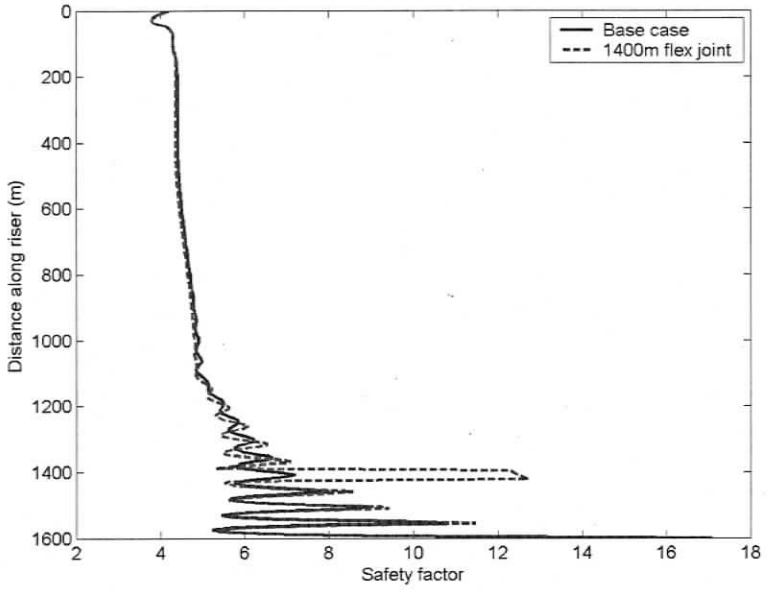

Figure 4.20: Testbed riser with flex joint at 1400 m n_s for $0.7\frac{m}{s}$ step current.

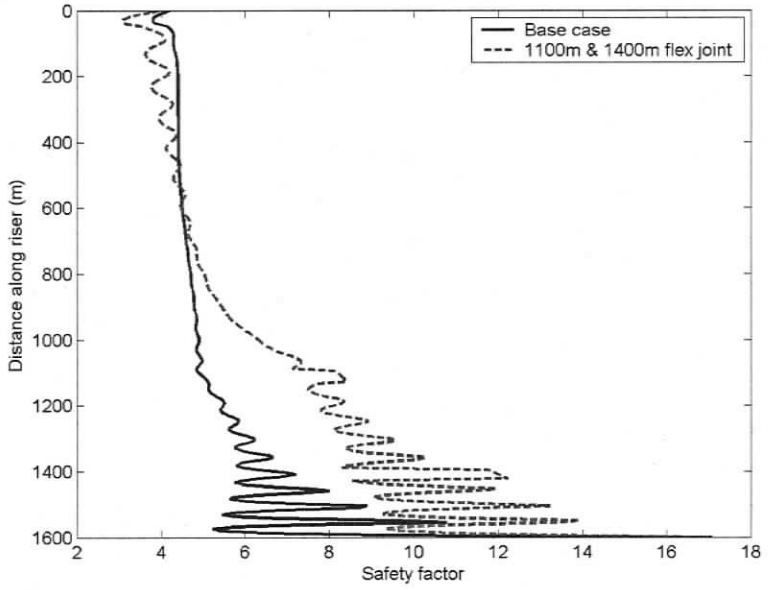

Figure 4.21: Testbed riser with flex joints at 1100 m and 1400 m n_s for $0.7\frac{m}{s}$ step current.

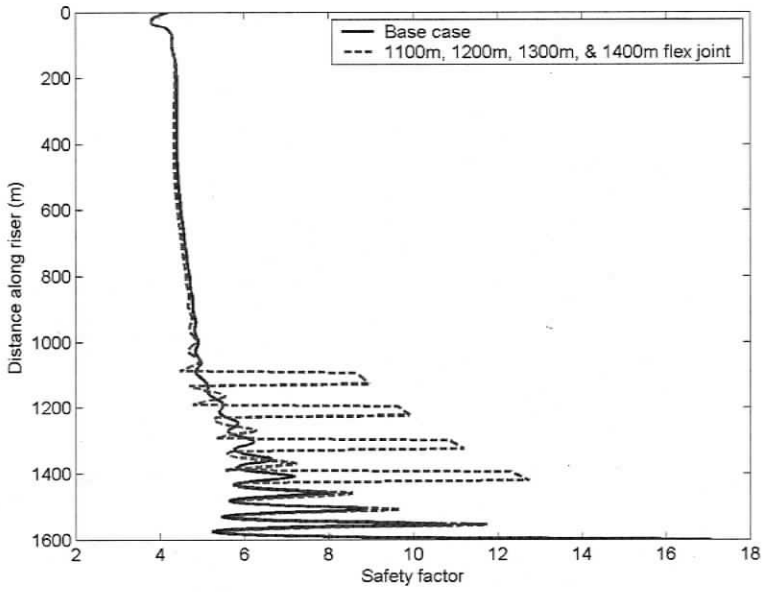

Figure 4.22: Testbed riser with flex joints at 1100 m, 1200 m, 1300 m, and 1400 m n_s for $0.7\frac{m}{s}$ step current.

velocity in section 4.3.4.

Table 4.6: Reduced velocity and difference in frequency of von Mises stress from plain testbed riser for each flex joint configuration at $0.7\frac{m}{s}$

Flex joints	V_r	f_{ex} (%)
1 (1100m)	5.6	3.7
1 (1400m)	5.7	2.2
2	6.0	3.0
4	5.8	0.73

4.3.4 Lower Region Flex Joints: $0.9\frac{m}{s}$ Step Current

Figures 4.23 - 4.28 show n_s for testbed risers with flex joints in the lower region at a current speed of $0.9\frac{m}{s}$. Once again, the flex joints have a much larger n_s locally exceeding 100% of the unmodified riser.

Figures 4.23, 4.24, and 4.27 illustrate the nonlinear behaviour of the flex joint

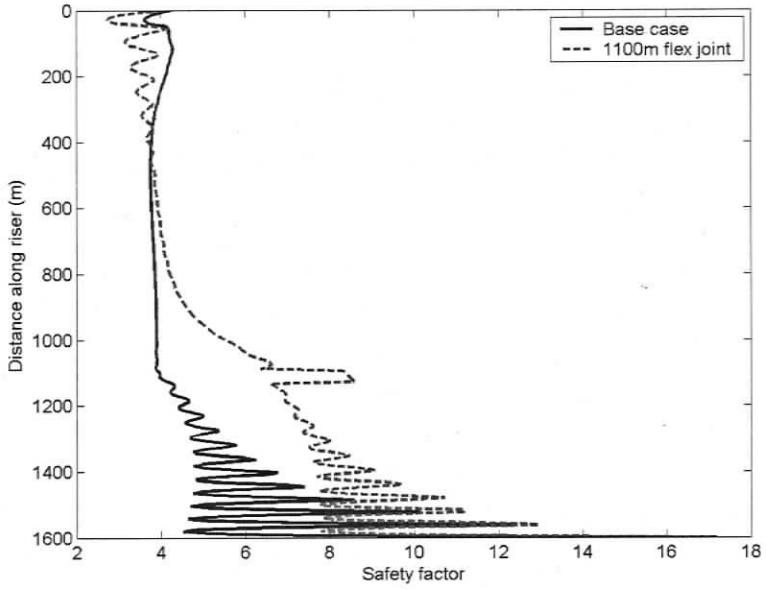

Figure 4.23: Testbed riser with flex joint at 1100 m n_s for $0.9\frac{m}{s}$ step current.

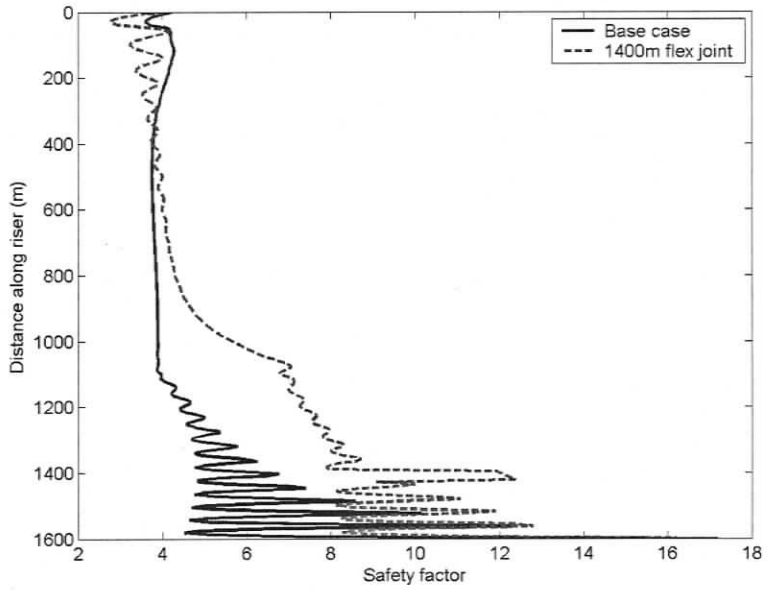

Figure 4.24: Testbed riser with flex joint at 1400 m n_s for $0.9\frac{m}{s}$ step current.

configurations. The testbed riser with a single flex joint at 1100 m and a single flex joint at 1400 m appear to drastically increase n_s across the bottom region of the riser. However, the effect is not as dramatic as the riser with 2 flex joints placed at 1100 m and 1400 m simultaneously.

Further investigation reveals that the difference in n_s in the regions away from the flex joints is caused by changes in the standard deviation of cross-flow component of curvature. Figures 4.25 and 4.26 illustrate the difference vibration envelope of the unmodified testbed riser to the testbed riser with flex joints at 1400 m and at 1100 m and 1400 m, respectively. Figure 4.25 shows significant changes in the vibration envelope, which is an indication that a modified mode of vibration is present in the testbed riser: the flex joints seem to confine the vibrations to the upper regions of the riser. The smaller envelope region corresponds to the larger n_s region, seen in Figure 4.24. In contrast, Figure 4.26 shows the vibration envelope is very similar to the unmodified riser. This complements the corresponding n_s profile seen in Figure 4.27, which is very similar to the unmodified riser.

The frequency behaviour of the different testbed riser configurations shows greater changes from the unmodified riser than at the lower V_{rel} values. In addition, the magnitude of change in frequency behaviour is very small compared to the changes induced in n_s. However, the largest changes in the frequency occur when the largest changes in n_s occur during the $0.9\frac{m}{s}$ case. A Fourier transform plot of the von Mises stress of unmodified testbed riser and testbed riser with a flex joint at 1100 m can be seen in Figures 4.29 and 4.30, respectively. Each plot illustrates the prominence of the VIV excitation frequencies. Peaks appear at different frequencies, which reinforces the idea that an alternate mode of vibration is present in the riser with flex joints. The reduced velocity, V_r, is still within nominal range for the riser in any configuration.

In all cases studied, the n_s within flex joints consistently increased relative to the unmodified testbed riser. The local n_s actually remained constant while the remaining n_s of the riser reduced with increasing V_{rel}. This is because the flex joints eliminate

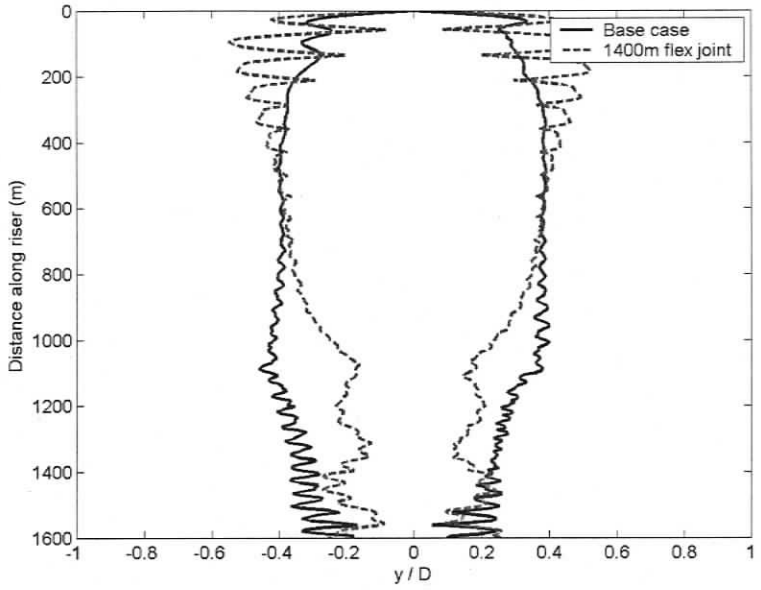

Figure 4.25: Comparison of vibration envelope of unmodified and single (1400m) flex joint testbed riser. The significant changes in vibration envelope shape, which corresponds to large n_s deviations, indicates a different mode of vibration may be present.

Table 4.7: Reduced velocity and difference in frequency of von Mises stress from plain testbed riser for each flex joint configuration at $0.9\frac{m}{s}$

Flex joints	V_r	f_{ex} (%)
1 (1100m)	6.1	7.7
1 (1400m)	6.1	6.6
2	6.1	7.2
4	6.2	9.4

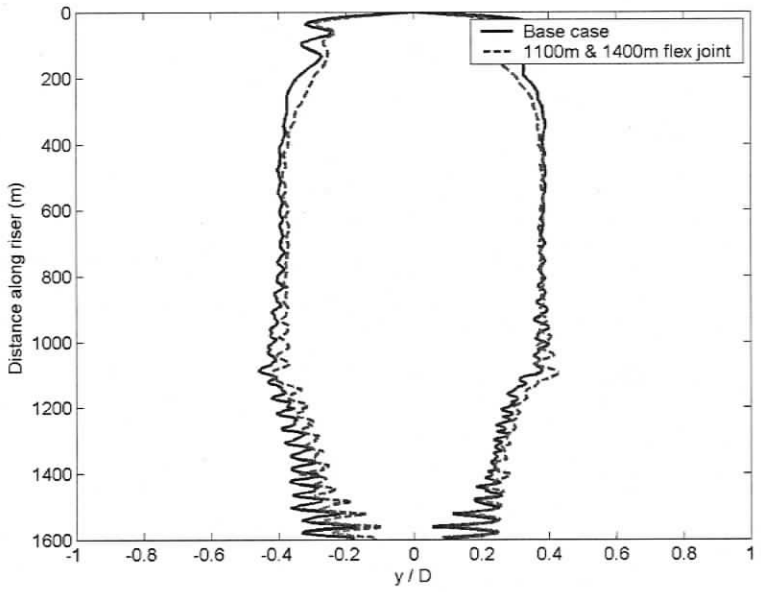

Figure 4.26: Comparison of vibration envelope of unmodified and double flex joint testbed riser. With flex joints placed at 1100m and 1400m, the vibration envelope and n_s profiles for these cases are very similar, which indicates that the same mode of vibration is present.

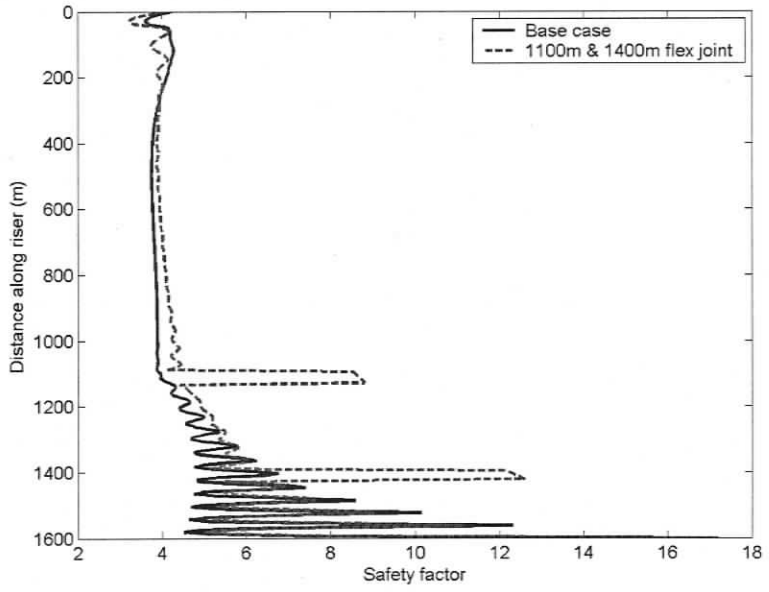

Figure 4.27: Testbed riser with flex joints at 1100 m and 1400 m n_s for $0.9\frac{m}{s}$ step current.

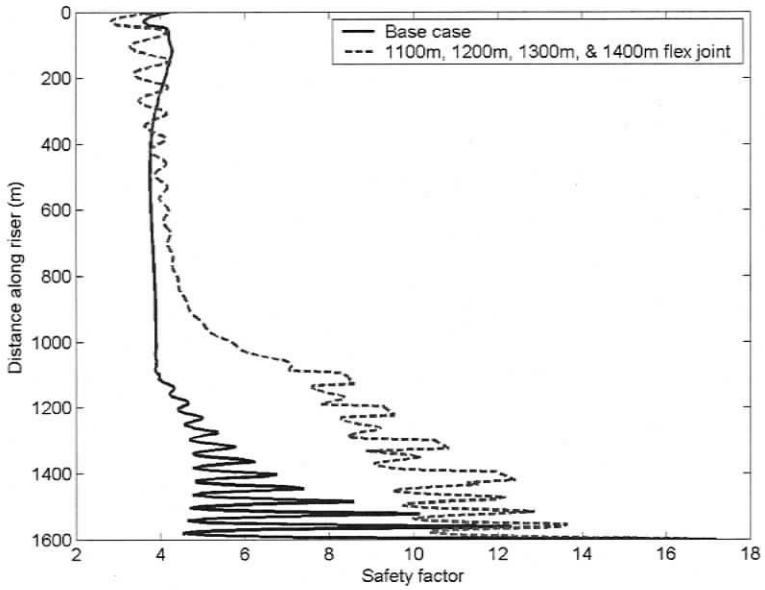

Figure 4.28: Testbed riser with flex joints at 1100 m, 1200 m, 1300 m, and 1400 m n_s for $0.9\frac{m}{s}$ step current.

the oscillating but not mean stress values. As V_{rel} increases, the oscillating stresses outside of the flex joints are amplified by larger curvatures in the riser.

Both the frequency of von Mises stress and n_s in the remaining regions of the testbed risers showed little deviation from the unmodified riser until the $0.9\frac{m}{s}$ case. When n_s increased significantly in regions surrounding flex joints, the vibration envelope was also affected and the frequency shifted by a minimum of 7%, which suggests a different mode of vibration in the riser was stimulated. However, not all testbed risers exhibited this behaviour. This indicates the placement and number of flex joints may need to be optimized for particular environment conditions.

4.4 Buoyancy Module Results

The buoyancy modules used in the simulation were comprised of syntactic foam and doubled the local diameter following the ideas presented in [23] and [22]. In the sec-

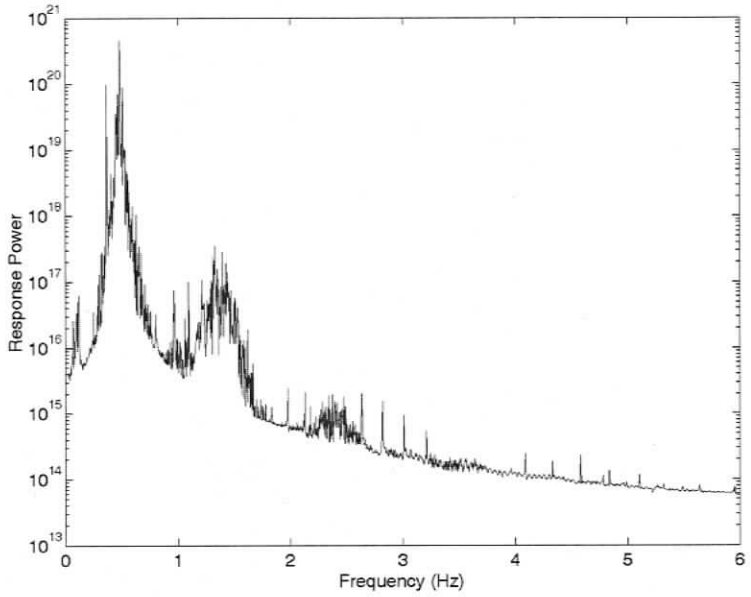

Figure 4.29: Sample frequency domain power spectrum plot from the unmodified testbed riser. The von Mises oscillation frequency was extracted by finding the frequency that corresponded to the maximum power peak. Multiple peaks indicate different modes of vibration stimulated.

tions with buoyancy modules, the only structural parameter change was the adjustment in mean testbed riser density and the overall diameter; all structural properties were the same as other nominal sections of the testbed riser.

Buoyancy modules were added to the riser in two arbitrary configurations: 5 modules of 50 m length each (16% coverage) and 8 modules of 20 m length each (10% coverage). The 16% coverage case modules were spaced 180 m apart and 90 m from the top and 110 m from the bottom of the riser. The 10% coverage case modules were spaced 250 m apart and 200 m from the top and 150 m from the bottom of the riser. The same current profiles used in the flex joint analysis were run with the module configurations.

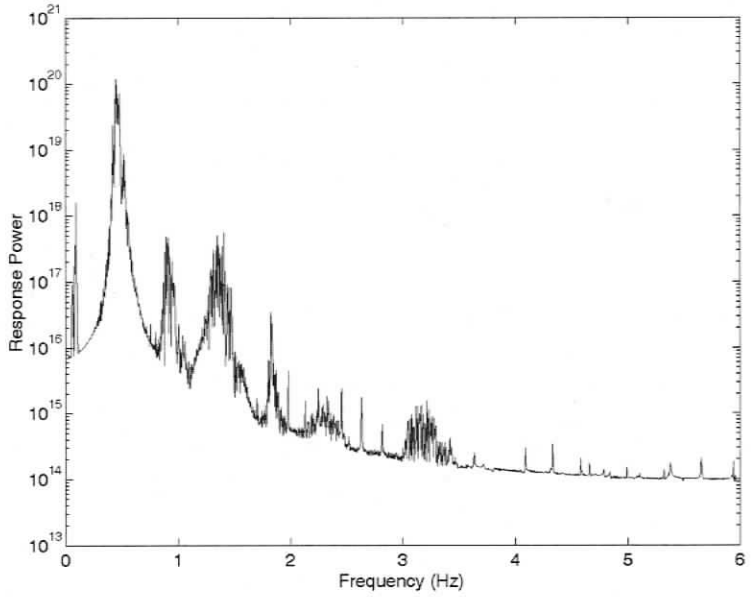

Figure 4.30: Sample frequency domain power spectrum plot from testbed riser with flex joint at 1100 m.

4.4.1 Buoyancy Module Results: $0.5\frac{m}{s}$ Step Current

Figures 4.31 and 4.32 show the buoyancy modules exhibit the opposite effect of flex joints on the safety factor, n_s, locally on the testbed riser: n_s is decreased rather than increased. However, the remainder of the riser has an n_s value that is higher than the unmodified testbed riser. The effect is more pronounced on the riser with 5 buoyancy modules because of the longer module lengths used. The larger area concentrates more hydrodynamic force, which then reduces n_s accordingly.

The qualitative comparison of Figure 4.31 and Figure 4.32 indicates that 16% coverage increases n_s over the majority of the testbed riser span more than 10% coverage. In addition, Figure 4.31 indicates n_s only decreases below the unmodified riser at the location of the buoyancy modules.

Frequency analysis compiled in Table 4.8 shows that the reduced velocity, V_r, is still within an acceptable range. The frequency of stress oscillations is about 6%

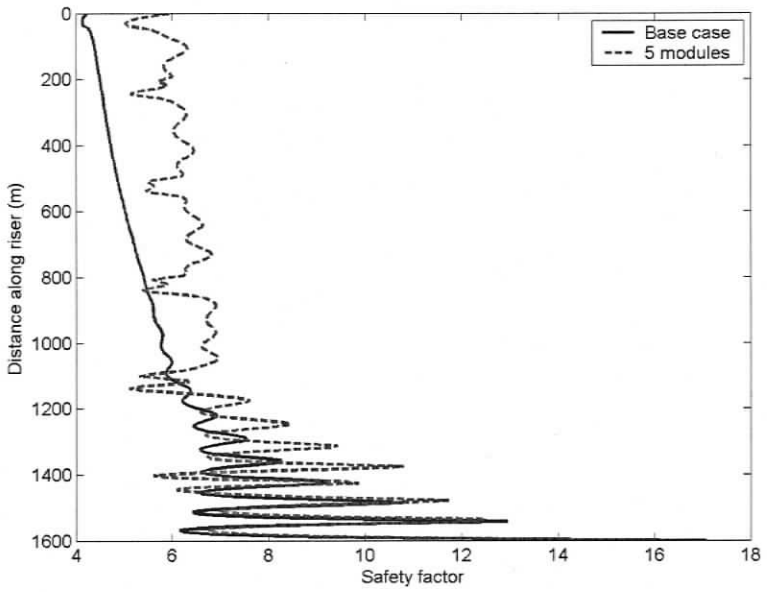

Figure 4.31: Testbed riser with 16% buoyancy modules n_s in a $0.5\frac{m}{s}$ step current

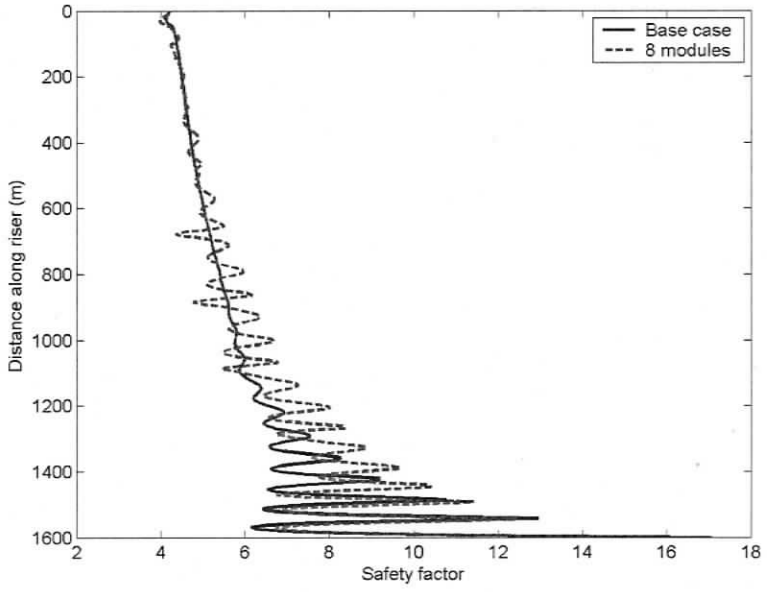

Figure 4.32: Testbed riser with 10% coverage n_s in a $0.5\frac{m}{s}$ step current

different than the unmodified testbed riser. This is significantly higher change than was observed with flex joints in the same V_{rel}.

Table 4.8: Reduced velocity and difference in frequency of von Mises stress from plain testbed riser for each buoyancy module configuration at $0.5\frac{m}{s}$

Coverage (%)	V_r	f_{ex} (%)
16%	6.0	6.0
10%	5.3	5.9

4.4.2 Buoyancy Module Results: $0.7\frac{m}{s}$ Step Current

With higher V_{rel}, similar trends in n_s are observed. Figures 4.33 and 4.34 show similar n_s profiles, though the testbed riser with 16% coverage appears to have higher n_s values near the top of the riser span. Unlike the flex joint cases, the n_s profile correlates poorly with the unmodified testbed riser. This is a sign that the buoyancy modules are significantly disrupting the modes of vibration present.

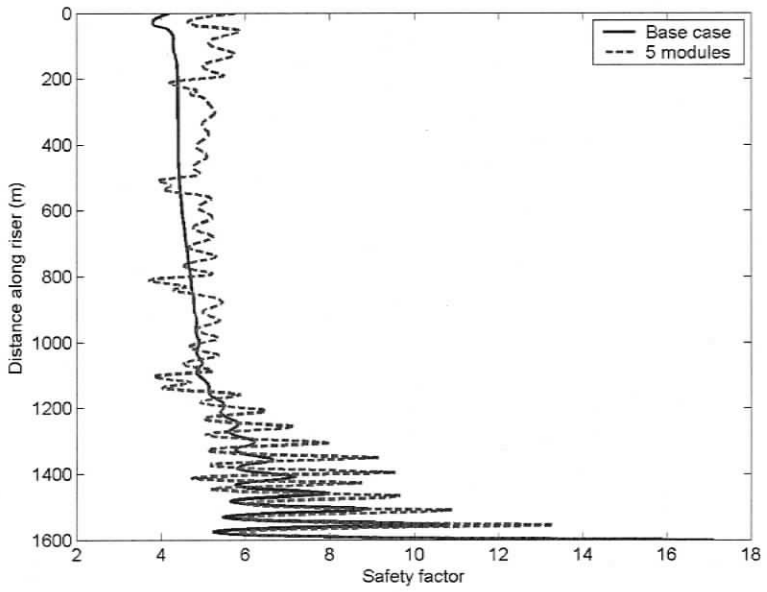

Figure 4.33: Testbed riser with 16% coverage n_s in a $0.7\frac{m}{s}$ step current

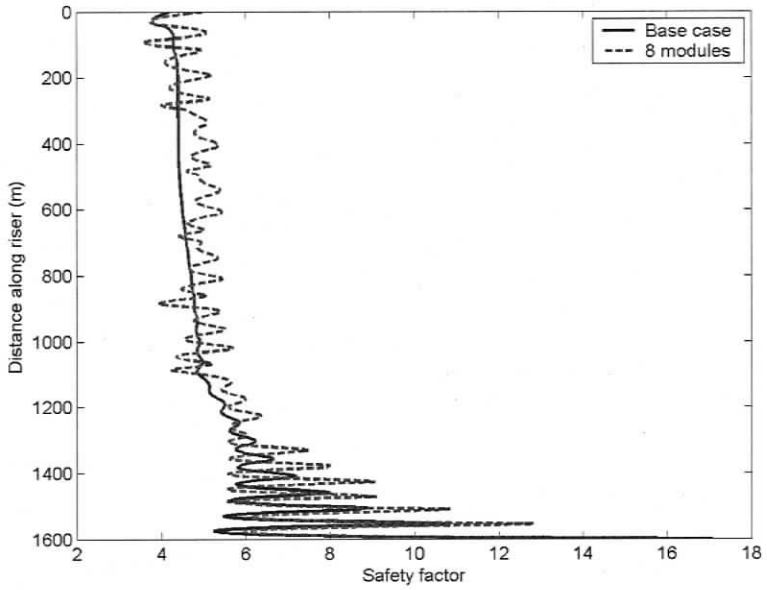

Figure 4.34: Testbed riser with 10% coverage n_s in a $0.7\frac{m}{s}$ step current

The vibration frequency of the 16% coverage riser has increased to 9.5% different than the unmodified riser, while the 10% coverage riser is only 7.3% different. These changes are higher still than the flex joint cases at the same V_{rel}.

Table 4.9: Reduced velocity and difference in frequency of von Mises stress from plain testbed riser for each buoyancy module configuration at $0.7\frac{m}{s}$

Coverage (%)	V_r	f_{ex} (%)
16	5.3	9.5
10	5.4	7.3

4.4.3 Buoyancy Module Results: $0.9\frac{m}{s}$ Step Current

Comparison of the n_s profiles in Figures 4.35 and 4.36 reveals the 16% coverage case performs more favourably than the 10% coverage case. In addition, Table 4.10 shows the 16% coverage case reduces the vibration frequency more than the 10% coverage case.

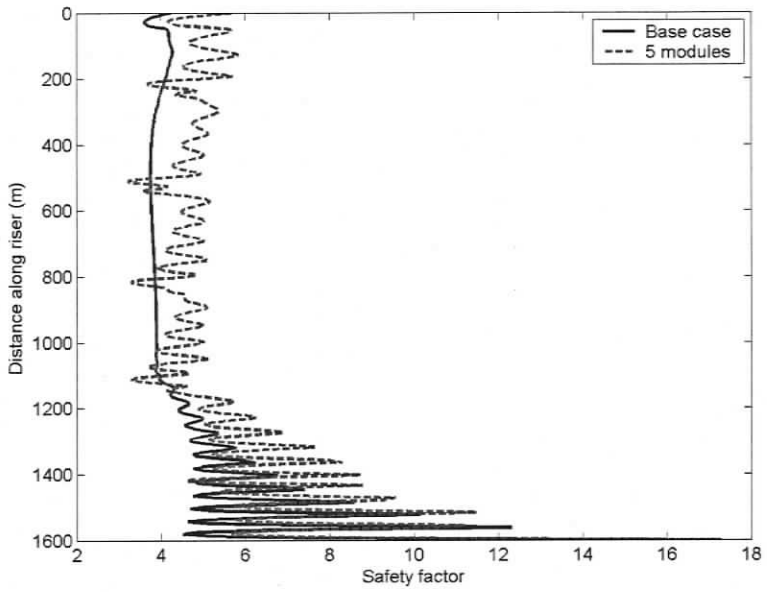

Figure 4.35: Testbed riser with 16% coverage n_s profile in a $0.9\frac{m}{s}$ step current

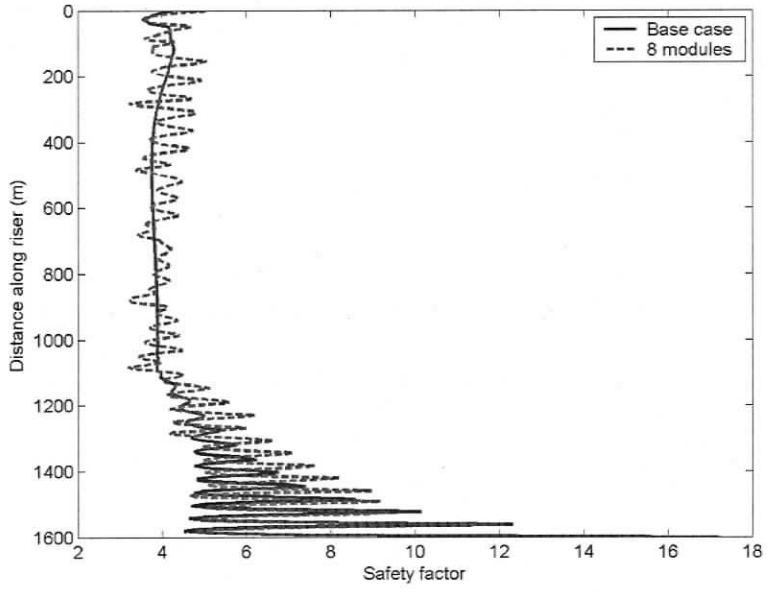

Figure 4.36: Testbed riser with 10% coverage n_s profile in a $0.9\frac{m}{s}$ step current

Table 4.10: Reduced velocity and difference in frequency of von Mises stress from plain testbed riser for each buoyancy module configuration at $0.9\frac{m}{s}$

Coverage (%)	V_r	f_{ex} (%)
16	6.4	11
10	5.2	8.3

The frequency analysis indicates further reduction in the vibration frequency from the base riser case, with the 16% coverage riser again outperforming the 10% coverage riser. This suggests that the threshold of coverage of the riser should be at least 16% to significantly impact the oscillation frequency as well as n_s of the testbed riser.

The frequency changes were expected because of the significantly different vortex shedding frequency on the buoyancy modules. Because of the nature of these devices, the minimum 15% coverage requirement may also apply to other similar VIV suppression devices such as helical strakes seen in Figure 1.10.

Chapter 5

Conclusions

The goal of the research presented was to study the effects of unorthodox VIV suppression devices. To study this problem, an effective VIV model was generated by coupling the wake oscillator model to an existing numerical cable model. To include ocean wave effects on the testbed riser VIV response, an algorithm for dynamically modelling rigid body interaction with the sea surface was created. This chapter provides an overview of the accomplishments and recommended future work based on the results.

5.1 Conclusions

Chapter 1 provided the background and motivation for the work: long and slender structures such as marine risers can be susceptible to metal fatigue damage by vibrations induced by vortex shedding in marine currents. Classic VIV suppression devices include helical strakes which cover large spans of the riser and as a result can be time-consuming to install and remove. Chapter 1 also introduces the theoretical motivation for investigating alternative methods of VIV suppression. The alternative methods disrupt the correlation of vortex shedding by introducing buoyancy modules

or alter the structural properties of the riser to mitigate higher mode response to vortex shedding. Chapter 2 presents the details of coupling the wake oscillators to the numerical cable model and the algorithm that describes the variable buoyancy module. Chapter 3 presented validation of both the variable buoyancy module as well as the completed VIV model. Though the variable buoyancy module results converged to results from static analytical theory, time constraints ruled out its use in modelling the riser system. Finally, the testbed riser system was modelled with several configurations which included the use of flex joints and buoyancy modules. In order to compare results of each configuration properly, the von Mises stress at a point on the outer surface of the riser was calculated at each node of the finite element mesh for all points in time. The time series data was then used to calculate the safety factor, n_s, guarding against fatigue failure in addition to the oscillation frequencies. Analysis of the results revealed several key results:

1. Within the flex joints, the stress oscillations are eliminated, which makes them an effective tool to combat specific regions of poor fatigue performance. However, they do not eliminate the mean stress of the riser. This is why the flex joints appeared to have a constant n_s while the remaining span decreased n_s as larger V_{rel} induced higher modes, larger curvatures and hence larger oscillation stresses.

2. In lower modes if vibration, flex joints do not affect the n_s of the remaining span of the riser. However, the frequency of oscillation deviates within 4%.

3. At higher modes of vibration, some flex joint configurations exhibited significant increases in n_s along large spans of the testbed riser. In these cases, the vibration envelope significantly changed and the oscillation frequency shifted from the unmodified riser by at least 7%. These are signs that the testbed riser can vibrate in a less damaging mode of vibration.

4. Flex joints placed in the upper region of the riser do not affect the dynamic behaviour of the testbed riser and the changes in local n_s were much smaller than when flex joints were placed in the lower regions. This was expected as the larger tensions found at the top of the riser dominate the frequency characteristics as well as the von Mises stress.

5. Buoyancy modules disrupt the n_s profile of the testbed riser. In all cases, 16% covered testbed riser n_s profile was at least equal or better than the unmodified riser, except in the sections with modules applied. The larger diameter of the modules induces hydrodynamic force amplification, which decreases n_s below the unmodified riser.

6. Judging by the n_s performance, the 10% covered riser did not perform as well as the 16% covered riser. Since both modules were equally distributed along the testbed riser, 16% coverage indicates a minimum coverage requirement for these devices to work properly.

7. The minimum coverage requirement of 16% may apply to more traditional VIV suppression devices such as helical strakes because of their similar fundamental behaviour: decorrelation of vortex shedding along the riser.

The simulations completed indicate that the flex joints are effective at locally alleviating fatigue damage. Buoyancy modules appear to alleviate some stress fluctuations though there are penalties in the form of larger mean stresses. A more detailed fatigue analysis was beyond the scope of the research presented here because more detailed information on current profiles at the site would be needed and VIV model that can accurately model noisy current profiles would be necessary.

5.2 Future Work

There are many areas to continue and enhance the research presented here:

1. Perform sensitivity analysis on environment currents and flex joint configurations to reveal the relationship between placement and distribution of flex joints and V_{rel}. Only a single ocean current profile was studied and incorporating the perturbations from surface waves may also provide additional insight.

2. Complete additional simulations to analyse the performance of buoyancy modules over a wider range of current profiles and magnitudes.

3. Perform sensitivity analysis on the combined use of buoyancy modules and flex joints. Combining the attributes of both VIV suppression devices may provide additional insight and serve to confirm the performance of each suppression mechanism in a more complex model.

4. Investigate the use of wake oscillators tuned to noisy water current profiles. In the validation phase, the wake oscillator used in this work proved to be unrealistically sensitive to shear currents. The use of a higher density mesh to model the shear or noisy currents will not be feasible due to the required execution time, so an alternate wake oscillator model or other method of modelling VIV may be needed.

5. Implement Miner's rule to blend fatigue analysis results from a variety of ocean water currents to provide a fatigue life for the riser. Once the noisy water current VIV model is complete, a fatigue analysis tool can be created in a straightforward manner. This will require many simulations to generate the response to each current profile.

6. Investigate and confirm buoyancy and flex joint results with an alternate VIV

modelling tool or with new VIV model. Confirming the buoyancy module behaviour can be completed with commercial software.

References

[1] Vaclav Smil. *Energy at the Crossroads: Global perspectives and Uncertainties.* MIT Press, 1 edition, 2005.

[2] G. Clauss, E. Lehmann, and C. Ostergaard. *Offshore Structures: Conceptual Designs and Hydromechanics.* Springer-Verlag, 1992.

[3] T. Sarpkaya. A critical review of the intrinsic nature of vortex-induced vibrations. *Journal of Fluids and Structures*, 19:389–447, 2004.

[4] website. http://www.oceansatlas.com/unatlas/about/ physicalandchemical-properties/background/oceanenvironment.html.

[5] Jr. B. C. Gerwick. *Construction of Marine and Offshore Structures.* CRC Press, second edition, 2000.

[6] website. http://en.wikipedia.org/wiki/human_hair.

[7] NASA sattellite image website. http://disc.gsfc.nasa.gov/oceancolor/scifocus/oceancolor/vonkarman_vortices.shtml.

[8] J. H. Lienhard. Synopsis of lift, drag, and vortex frequency data for rigid circular cylinders. Research division bulletin 300, Washington State University, 1966.

[9] F. M. White. *Fluid Mechanics.* McGraw-Hill, Toronto, fourth edition, 1999.

[10] T. Sarpkaya. Vortex-induced oscillations: A selective review. *Journal of Applied Mechanics*, 46:241–258, 1979.

[11] C. C. Feng. The measurements of vortex-induced effects in flow past a stationary and oscillating circular and d-section cylinders. Master's thesis, University of British Columbia, 1968.

[12] R. D. Blevins. *Flow induced vibrations.* Van Nostrand Reinhold, 2 edition, 1990.

[13] C.H.K. Williamson and R. Govardhan. Vortex induced vibrations. *Annual Review of Fluid Mechanics*, 36:413–455, 2004.

[14] R. A. Skop and S. Balasubramanian. A new twist on an old model for vortex-excited vibrations. *Journal of Fluids and Structures*, 11:395–412, 1997.

[15] J. K. Vandiver. Drag coefficients of long flexible cylinders. In *Proceedings of the Offshore Technology Conference*, pages 405–410, Houston, TX, 1983. OTC 4490.

[16] C. Evangelinos, D. Lucor, and G. E. Karniadakis. DNS-derived force distribution on flexible cylinders subject to vortex-induced vibration. *Journal of Fluids and Structures*, 14:429–440, 2000.

[17] J. R. Chaplin, P. W. Bearman, F. J. Huera Huarte, and R. J. Pattenden. Laboratory measurements of vortex-induced vibrations of a vertical tension riser in a stepped current. *Journal of Fluids and Structures*, 21:3–24, 2005.

[18] R. D. Gabbai and H. Benaroya. An overview of modelling and experiments of vortex-induced vibration of circular cylinders. *Journal of Sound and Vibration*, 282:575–616, 2005.

[19] Ch-H. Bruneau and I. Mortazavi. Control of vortex shedding around a pipe section using a porous sheath. *International Journal of Offshore and Polar Engineering*, 16(2):90–96, 2006.

[20] S. Mittal and A. Raghuvanshi. Control of vortex shedding behind circular cylinder for flows at low Reynolds numbers. *International Journal for Numerical Methods in Fluids*, 35:421–447, 2001.

[21] S. Tang and N Aubry. Suppression of vortex shedding inspired by a low-dimensional model. *Journal of Fluids and Structures*, 14:443–468, 2000.

[22] D. Walker and R. King. Vortex excited vibrations of tapered and stepped cylinders. In *Proceedings of the 7th international conference on offshore mechanics and arctic engineering*, pages 229–234, 1988.

[23] I.H. Brooks. A pragmatic approach to vortex-induced vibrations of a drilling riser. In *19th Annual offshore technology conference*, pages 327–333, 1987.

[24] Singiresu S. Rao. *Mechanical Vibrations.* Pearson Prentice Hall, 4 edition, 2004.

[25] P. W. Bearman. Vortex shedding from oscillating bluff bodies. *Annual Review of Fluid Mechanics*, 16:195–222, 1984.

[26] M. S. Pantazopoulos. Vortex-induced vibration parameters: Critical review. In *Proceedings of the International Conference on Offshore Mechanics and Arctic Engineering*, volume 1, Houston, TX, 1994.

[27] SHEAR7 website. http://web.mit.edu/shear7/shear7.html.

[28] VIVANA website. http://www.sintef.no/upload/marintek/pdf-filer/sofware/vivana%20brosjyre.pdf.

[29] Orcaflex VIV Toolbox website. http://www.orcina.com/ softwareproducts/vivtoolbox/index.php.

[30] J. R. Chaplin, P. W. Bearman, Y. Cheng, E. Fontaine, J. M. R. Graham, K. Herfjord, F. J. Huera Huarte, M. Isherwood, K. Lambrakos, C. M. Larsen, J. R. Meneghini, G. Moe, R. J. Pattenden, M. S. Triantafyllou, and R. H. J. Willden.

Blind predictions of laboratory measurements of vortex-induced vibrations of a tension riser. *Journal of Fluids and Structures*, 21:25–40, 2005.

[31] S. Balasubramanian, R. A. Skop, F. L. Haan Jr., and A. A. Szewczyk. Vortex-excited vibrations of uniform pivoted cylinders in uniform and shear flow. *Journal of Fluids and Structures*, 14:65–85, 2000.

[32] W. J. Kim and N. C. Perkins. Coupled slow and fast dynamics of flow excited elastic cable systems. *Journal of Vibration and Acoustics*, 125:155–161, 2003.

[33] M. L. Facchinetti, E. de Langre, and F. Biolley. Coupling of structure and wake oscillators in vortex-induced vibrations. *Journal of Fluids and Structures*, 19:123–140, 2004.

[34] M. L. Facchinetti, E. de Langre, and F. Biolley. Vortex-induced travelling waves along a cable. *European Journal of Mechanics B/Fluids*, 23:199–208, 2004.

[35] B. J. Buckham and M. Nahon. Formulation and validation of a lumped mass model for low-tension rov tethers. *International Journal of Offshore and Polar Engineering*, 11(4):282–289, 2001.

[36] B. J. Buckham. *Dynamics Modelling of Low-Tension Tethers for Submerged Remotely Operated Vehicles.* PhD thesis, University of Victoria, 2003.

[37] B. J. Buckham, F. R. Driscoll, and M. Nahon. Development of a finite element cable model for use in low tension dynamics simulation. *Journal of Applied Mechanics*, 71(4):476–485, 2004.

[38] B. J. Buckham, F. R. Driscoll, M. Nahon, and B. Radanovic. Torsional mechanics in dynamics simulation of low-tension marine tethers. *International Journal of Offshore and Polar Engineering*, 14(3):218–226, 2004.

[39] M. Nahon. A simplified dynamics model for autonomous underwater vehicles. In *Proceedings of the 1996 IEEE Symposium on Autonomous Underwater Vehicle Technology*, pages 373–379, 1996.

[40] D. Steinke. Design and simulation of a Kalman filter for ROV navigation. Master's thesis, University of Victoria, 2005.

[41] B. J. Hamrock, B. Jacobson, and S. R. Schmid. *Fundamentals of Machine Elements.* McGraw-Hill, Inc., 1999.

[42] J. H. Ginsberg. *Advanced Engineering Dynamics.* Cambridge University Press, New York, NY, second edition, 1998.

[43] A. E. H. Love. *A Treatise on the Mathematical Theory of Elasticity.* Cambridge University Press, 1927.

[44] M. Caccia, G. Indiveri, and G. Veruggio. Modelling and identification of open-frame variable configuration unmanned underwater vehicles. *IEEE Journal of Oceanic Engineering*, 25(2):227–240, 2000.

[45] O. M. Faltinsen. *Sea Loads on Ships and Offshore Structures.* Cambridge University Press, New York, NY, 1990.

[46] D. V. Reddy and M. Arockiasamy, editors. *Offshore Structures*, volume 1. Kreiger Publishing Co., Malabar, FL, 1991.

[47] D. J. Acheson. *Elementary Fluid Dynamics.* Clarendon Press, Oxford, 1990.

[48] D. Dalrymple. *Water Wave Mechanics for Engineers and Scientists.* World Scientific Publishing Co. Pte. Ltd., 1991.

[49] R. M. Sorensen. *Basic Wave Mechanics for Coastal and Ocean Engineers.* John Wiley and Sons, Inc., 1993.

[50] M. E. McCormick. *Ocean Engineering Wave Mechanics.* John Wiley and Sons, Inc., Toronto, 1973.

[51] G. D. Crapper. *Introduction to Water Waves.* John Wiley and Sons, Inc., Rexdale, ON, 1984.

[52] A. D. Trim, H. Braaten, H. Lie, and M. A. Tognarelli. Experimental investigation of vortex-induced vibration of long marine risers. *Journal of Fluids and Structures*, 21:335–361, 2005.

[53] C. T. Yamamoto, J. R. Meneghini, F. Saltara, R. A. Fregonesi, and J. A. Ferrari Jr. Numerical simulations of vortex-induced vibration on flexible cylinders. *Journal of Fluids and Structures*, 19:467 – 489, 2004.

[54] F. P. Beer and Jr. E. R. Johnston. *Mechanics of Materials.* McGraw-Hill, Inc., second edition, 1992.

[55] D. G. Zill. *A first course in differential equations with modelling applications.* Brooks Cole Publishing Company, sixth edition, 1997.

[56] website. http://www.crgrp.net/syntactics.htm.

Appendix A

Tensioned Beam Natural Frequency

This section reviews the derivation of equation (1.9), which is repeated here for convenience [24]:

$$\omega_n = \frac{\pi^2}{l^2}\sqrt{\frac{n^4 EI}{\rho_s A} + \frac{n^2 T l^2}{\pi^2 \rho_s A}} \tag{A.1}$$

A free body diagram of a freely vibrating differential segment of a beam can be seen in figure A.1

A Taylor series expansion is applied to approximate the forces on the end of the segment. For example, the shear force $V(x+dx)$ is:

$$V(x+dx) = V(x) + \frac{\partial V}{\partial x}dx + \frac{\partial^2 V}{\partial x^2}dx^2 + ... \tag{A.2}$$

Terms higher than the first derivative can be neglected because of increasing powers of the infinitesimal length dx. The shear force is then:

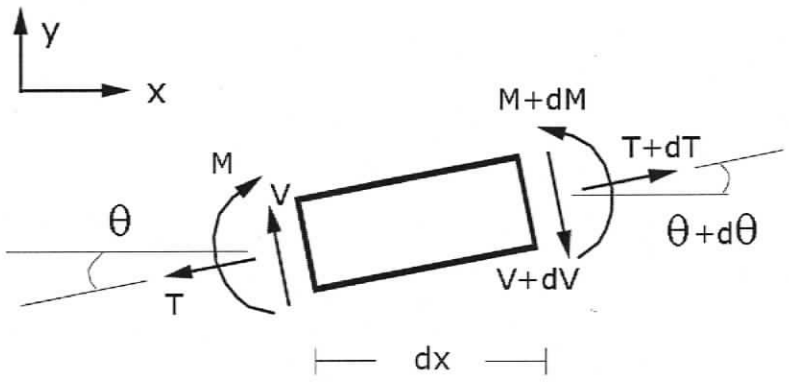

Figure A.1: Differential beam segment

$$V(x+dx) = V(x) + \frac{\partial V}{\partial x}dx = V + \frac{\partial V}{\partial x}dx \tag{A.3}$$

Applying this approximation the vertical component of the Newtonian equation of motion is:

$$V - (V+dV) + (T+dT)\sin(\theta+d\theta) - T\sin\theta = \rho_s A dx \frac{\partial^2 w}{\partial t^2} \tag{A.4}$$

with axial tension T, beam cross section area A, material density ρ_s, and vertical displacement w. The net moments about point O give:

$$M - (M+dM) + Vdx = 0 \tag{A.5}$$

where M is the internal moment. Equation (A.4) is linearised with the small angle approximation:

$$sin(\theta + d\theta) \cong \theta + d\theta = \theta + \frac{\partial \theta}{\partial x} dx \tag{A.6}$$

For small deflections, angle θ gives the spatial rate of change of deflection w:

$$\theta = \frac{\partial w}{\partial x} \tag{A.7}$$

and so equation (A.6) becomes:

$$\theta + \frac{\partial \theta}{\partial x} dx = \frac{\partial w}{\partial x} + \frac{\partial^2 w}{\partial x^2} dx \tag{A.8}$$

Applying equations (A.6,A.7,A.8) to equation (A.4) gives:

$$\begin{aligned} \rho_s A dx \frac{\partial^2 w}{\partial t^2} &= -\frac{\partial V}{\partial x} dx - T \frac{\partial w}{\partial x} + \left(T + \frac{\partial T}{\partial x} dx \right) \left(\frac{\partial w}{\partial x} + \frac{\partial^2 w}{\partial x^2} dx \right) \\ \rho_s A \frac{\partial^2 w}{\partial t^2} &= -\frac{\partial V}{\partial x} + \frac{\partial}{\partial x} \left(T \frac{\partial w}{\partial x} \right) \end{aligned} \tag{A.9}$$

Rearranging equation (A.5) and differentiating both sides by x:

$$\begin{aligned} 0 &= -dM + V dx \\ \frac{\partial M}{\partial x} &= V \\ \frac{\partial^2 M}{\partial x^2} &= \frac{\partial V}{\partial x} \end{aligned} \tag{A.10}$$

Differentiating the Euler beam relationship between displacement and bending moment [54] by x twice and substituting equation (A.10):

$$\begin{aligned} EI\frac{\partial^2 w}{\partial x^2} &= M \\ \frac{\partial^2}{\partial x^2}\left(EI\frac{\partial^2 w}{\partial x^2}\right) &= \frac{\partial^2 M}{\partial x^2} \\ \frac{\partial^2}{\partial x^2}\left(EI\frac{\partial^2 w}{\partial x^2}\right) &= \frac{\partial V}{\partial x} \end{aligned} \tag{A.11}$$

Assuming the tension and cross-section properties A and EI are constant and substituting equation (A.11) into equation (A.9) gives the governing differential equation of beam displacement:

$$\rho_s A\frac{\partial^2 w}{\partial t^2} + EI\frac{\partial^4 w}{\partial x^4} - T\frac{\partial^2 w}{\partial x^2} = 0 \tag{A.12}$$

If the method of separation of variables is used to solve equation (A.12) the solution will be in the form:

$$w(x,t) = W(x)\left(A\cos(\omega t) + B\sin(\omega t)\right) \tag{A.13}$$

where ω is the oscillation frequency of the beam, A and B are scaling coefficients, and $W(x)$ is the structure spatial displacement. Substituting equation (A.13) into (A.12):

$$EI\frac{d^4 W}{dx^4} - T\frac{d^2 W}{dx^2} - \rho_s A\omega^2 W = 0 \tag{A.14}$$

Equation (A.14) is a homogeneous linear differential equation, which allows exponential solutions [55]:

$$W(x) = Ce^{sx} \tag{A.15}$$

where C and s are coefficients. Substituting equation (A.15) into (A.14) provides the auxiliary equation:

$$s^4 - \frac{T}{EI}s^2 - \frac{\rho_s A\omega^2}{EI} = 0 \tag{A.16}$$

The roots of the auxiliary equation can be found from the quadratic formula:

$$s_1^2, s_2^2 = \frac{T}{2EI} \pm \sqrt{\left(\frac{T}{2EI}\right)^2 + \frac{\rho_s A\omega^2}{EI}} \tag{A.17}$$

And the solution can be written:

$$W(x) = C_1\cosh(s_1 x) + C_2\sinh(s_1 x) + C_3\cos(s_2 x) + C_4\sin(s_2 x) \tag{A.18}$$

where the coefficients C_i, $i = 1, 2, 3, 4$ are determined from the boundary conditions of the beam. For a pinned-pinned beam, the boundary conditions are:

$$W(0) = 0 \tag{A.19}$$

$$W(l) = 0 \tag{A.20}$$

$$\frac{d^2W}{dx^2}|_0 = 0 \tag{A.21}$$

$$\frac{d^2W}{dx^2}|_l = 0 \tag{A.22}$$

$$\tag{A.23}$$

where l is the total beam length. Differentiating equation (A.18) and applying the boundary conditions:

$$\begin{aligned} W(0) &= 0 \\ &= C_1 + C_3 \qquad \text{(A.24)} \\ \frac{d^2W}{dx^2}|_0 &= 0 \\ &= C_1 s_1^2 - C_3 s_2^2 \qquad \text{(A.25)} \end{aligned}$$

Equations (A.25) and (A.25) show $C_1 = C_3 = 0$. Evaluating the other boundary conditions:

$$\begin{aligned} W(l) &= 0 \\ &= C_2 \sinh(s_1 l) + C_4 \sin(s_2 l) \\ C_2 \sinh(s_l) &= -C_4 \sin(s_2 l) \qquad \text{(A.26)} \\ \frac{d^2W}{dx^2}|_l &= 0 \\ &= C_2 s_1^2 \sinh(s_1 l) - C_4 s_2^2 \sin(s_2 l) \\ &= s_1^2 \left(-C_4 \sin(s_2 l)\right) - C_4 s_2^2 \sin(s_2 l) \\ &= \left[C_4 \sin(s_2 l)\right] \left[-s_1^2 - s_2^2\right] \qquad \text{(A.27)} \end{aligned}$$

Setting C_4 and C_2 to zero is a trivial solution. The roots of the auxiliary equation (A.17) show that if s_1^2 and s_2^2 can not be equal for nonzero values of tension and vibration frequency. Therefore, equation (A.27) can only be zero if:

$$s_2 l = n\pi \qquad \text{(A.28)}$$

for integers $n = 0, 1, 2....$ Substituting equation (A.28) into (A.17) and solving for the natural vibration frequency ω:

$$
\begin{aligned}
s_2^2 &= \left(\frac{n\pi}{l}\right)^2 \\
&= \frac{T}{2EI} - \sqrt{\left(\frac{T}{2EI}\right)^2 + \frac{\rho_s A\omega^2}{EI}}
\end{aligned}
$$

$$
\begin{aligned}
\omega^2 &= \frac{EI}{\rho_s A}\left[\left[\left(\frac{n\pi}{l}\right)^2 - \frac{T}{2EI}\right]^2 - \left(\frac{T}{2EI}\right)^2\right] \\
\omega &= \sqrt{\frac{EI}{\rho_s A}}\left[\left(\frac{n\pi}{l}\right)^4 + 2\left(\frac{n\pi}{l}\right)^2 \frac{T}{2EI}\right]^{\frac{1}{2}} \\
\omega &= \frac{\pi^2}{l^2}\sqrt{n^4\frac{EI}{\rho_s A} + \frac{n^2 T l^2}{\pi^2 \rho_s A}} \qquad \text{(A.29)}
\end{aligned}
$$

Appendix B

Riser Fatigue Parameters

Material properties for mild forged steel are E = 200 GPa, G = 77 GPa, yield strength of 250 MPa in tension and 145 MPa in shear, and ultimate strength of 400 MPa for structural steel (ASTM-A36) [54]. Recall that fatigue equations were extracted from [41].

First, the modified ultimate strength was found. It was assumed the riser steel has no special surface finish and so the surface finish factor was resolved:

$$\begin{aligned} k_f &= 272.0(400MPa)^{-0.995} \\ k_f &= 0.7007 \end{aligned} \tag{B.1}$$

The reliability factor of 0.82 for 99% probability of survival was selected. The size factor for axial loading is 1 and the modified ultimate strength was calculated:

$$\begin{aligned} S'_u &= k_s k_r k_f (S_u) \\ S'_u &= (0.6911)(0.82)(1)(400MPa) \\ S'_u &= 230MPa \end{aligned} \tag{B.2}$$

The low and high cycle strength limits for axial loading were found:

$$\begin{aligned} S_e &= 0.45 S'_u \\ S_e &= 104MPa \end{aligned} \tag{B.3}$$

$$\begin{aligned} S_l &= 0.75 S'_u \\ S_l &= 173MPa \end{aligned} \tag{B.4}$$

The coefficients for the finite-life equation were then evaluated for each loading type.

$$\begin{aligned} a_s &= \frac{(S_l)^2}{S_e} \\ a_s &= \frac{(173MPa)^2}{104MPa} \\ a_s &= 288MPa \end{aligned} \tag{B.5}$$

$$\begin{aligned} b_s &= -\frac{1}{3}\log\left(\frac{S_l}{S_e}\right) \\ b_s &= -\frac{1}{3}\log\left(\frac{173}{104}\right) \\ b_s &= -0.0737 \end{aligned} \tag{B.6}$$

The number of cycles until failure for finite life is given by:

$$N_i = \left(\frac{S_f}{a_s}\right)^{\frac{1}{b_s}} \tag{B.7}$$

Once the damage per stress cycle due to each ocean current profile is known, a probability of occurrence of ocean profile is needed to anticipate the cycles of damage n_i incurred and thus predict the life of the riser.

Appendix C

Bisection Zero-Finding Algorithm

Figure C.1 shows how the bisection method is used to find the zero of a function.

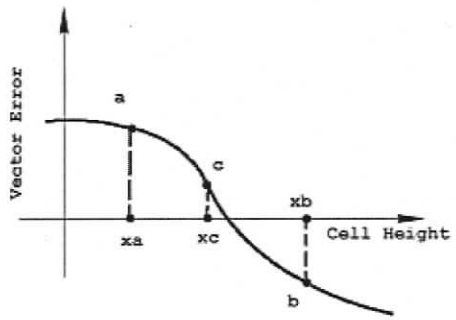

Figure C.1: Bisection optimization method

All the bisection method requires is a continuous function and two function values a and b with opposing sign and their corresponding function input parameters x_a and x_b. The average of x_a and x_b is taken to produce x_c, which is submitted to the function. The resulting function value c then replaces a if the sign of c matches that of a, otherwise it replaces b and the process continues until some adequate tolerance is reached.

Appendix D

Vibration Moving Average Filter

This section reviews the filter implemented to track the local VIV coordinate frame amplitudes. The main reason the local VIV coordinate and vibration tracking is needed is to properly implement the drag coefficient amplification equation (2.77) in section 2.3.3.

The filter detects the peaks in the signal (regardless of frequency) and removes the mean value. In this way, no specific filter frequency range needs to be specified as whatever frequency the structure vibrates at in the simulation is tracked and all low frequency drift is removed. An additional advantage of this filter is its simplicity: the low frequency drift is calculated during the dynamic simulation, so a computationally cheap method will not significantly hinder the execution speed.

Figure D.1 shows a periodic signal with an extremely low frequency drift. This signal could represent a point on a cable subject to VIV as it is towed through the water.

Figure D.2 shows a smaller section of the original signal in D.1. The filter stores the value of the signal at its peak in the variable y_{old}. As the signal moves away from the last peak value, the deflection is saved in the variable Δy.

Once Δy is a maximum, the next peak value is found and its value is saved in

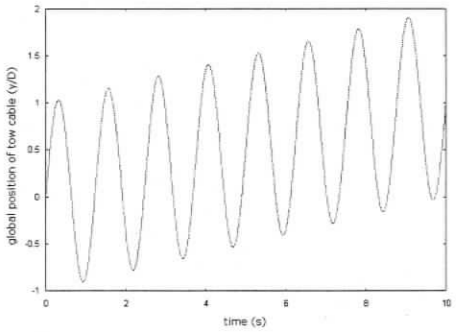

Figure D.1: Vibration signal with low frequency drift

y_{max}. At this point, the average between y_{old} and y_{max} is taken and used as the mean value to subtract from the signal to ensure there is zero mean during the next segment until a new peak is found. The value of y_{old} is updated with the current value of y_{max} and the process continues. The results of the filtering algorithm can be seen in figure D.3.

The peak-to-peak amplitude value is used to detect the local root-mean-square of amplitude measurement:

$$y_{rms} = \sqrt{\frac{\sum_i^{\chi} \left(\frac{\Delta y}{2}\right)^2}{\chi}} \tag{D.1}$$

where y_{rms} is the root-mean-square measurement of the amplitude for χ samples of the peak-to-peak amplitude Δy in time. The peak detection point also provides a convenient place to update the cross-flow axis vector direction as well as compute the updated drag coefficient with equation (2.77). If the cross-flow direction is updated at the peak of vibration, the relative velocity measurement will not be affected by the structure vibration velocity.

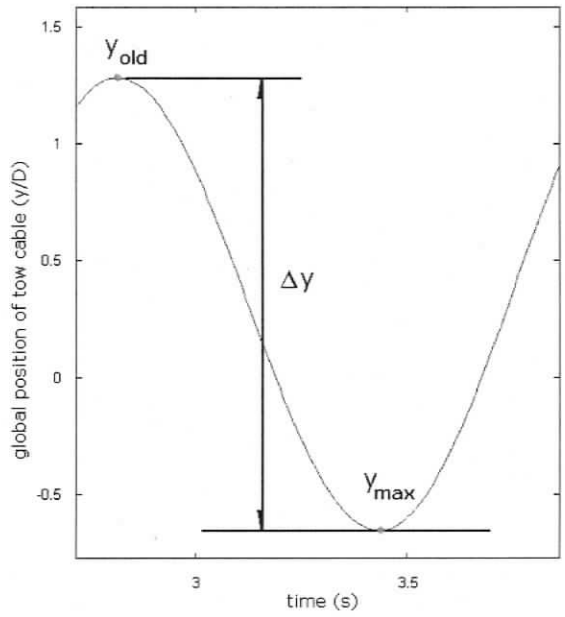

Figure D.2: Low frequency effects of signal detected

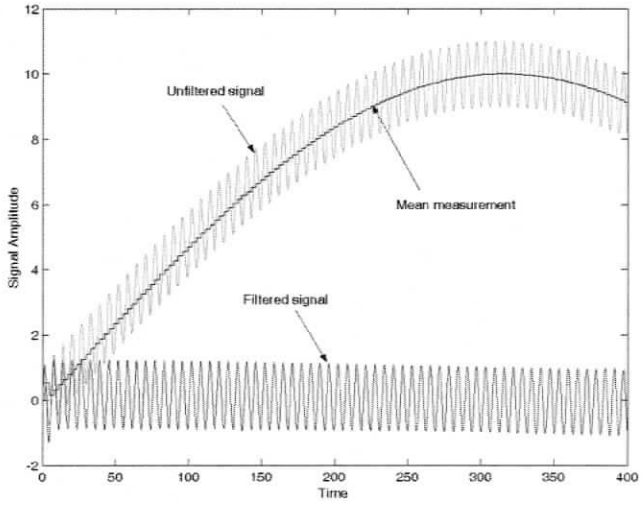

Figure D.3: Filter effects on a signal

Appendix E

Simulation Physical Properties

Interpolated structural values were made for [17, 30, 52, 53]. This was necessary since not all the same information was provided and similar values were needed to compare each system. In addition, structural values for axial (EA), flexural (EI), and torsional (GJ) rigidity were needed for the simulations. Formulas for area moment of inertias for simple shapes were taken from [54].

E.1 Uniform Current Calibration and Shear Validation Properties

[52] gives:

L = 38m, OD = 0.027 m, t = 0.003 m, E = 36.2e9 N/m^2, flooded mass ratio = 1.6. Material is fiberglass. Assuming isotropic material, flexural rigidity was calculated:

$$\begin{aligned} 10xy^2 + 15x^2y - 5xy &= 5\left(2xy^2 + 3x^2y - xy\right) \\ &= 5x\left(2y^2 + 3xy - y\right) \\ &= 5xy\left(2y + 3x - 1\right) \end{aligned} \tag{E.1}$$

$$\begin{aligned} I &= \frac{\pi}{4}\left(r_{out}^4 - r_{in}^4\right) \\ &= 1.65e - 8m^4 \end{aligned} \tag{E.2}$$

$$\begin{aligned} EI &= (36.2e9Nm^2)(1.65e - 8m^4) \\ &= 5.99e2Nm^2 \end{aligned} \tag{E.3}$$

mass per unit length was also found, assuming salt water density of 1025 $\frac{kg}{m^3}$:

$$\begin{aligned} \rho_r &= 1.6\left(\rho_w\right) \\ &= 1640\frac{kg}{m^3} \end{aligned} \tag{E.4}$$

Cross section area:

$$A = \frac{\pi}{4}\left(0.027m\right)^2 \tag{E.5}$$

Mass per unit length:

$$\begin{aligned} m_l &= \rho_r A \\ &= 0.939\frac{kg}{m} \end{aligned} \tag{E.6}$$

Since the shear modulus G was not measured, a value was obtained from using one third of the value of Young's modulus. This is usually a safe assumption for ductile materials, and though it may be crass to extend this use with a composite like fiberglass, there was little alternative since the material was not available for further analysis.

$$\begin{aligned} EA &= 36.2GPa\frac{\pi}{4}\left([0.027m]^2 - [0.021m]^2\right) \\ &= 8.19e6N \end{aligned} \tag{E.7}$$

$$\begin{aligned} EI &= 36.2GPa\frac{\pi}{4}\left(\left[\frac{0.027m}{2}\right]^4 - \left[\frac{0.021m}{2}\right]^4\right) \\ &= 5.99e2Nm^2 \end{aligned} \tag{E.8}$$

$$\begin{aligned} GJ &= 12GPa\frac{\pi}{2}\left(\left[\frac{0.027m}{2}\right]^4 - \left[\frac{0.021m}{2}\right]^4\right) \\ &= 3.97e2Nm^2 \end{aligned} \tag{E.9}$$

E.2 Uniform Current Validation Properties

[53] gives: OD = 0.25m, ID = 0.2116 m, E = 210 GPa, $\rho_{bore} = 800\ \frac{kg}{m^3}$, $\rho_{wall} = 7700\ \frac{kg}{m^3}$. Material is steel, so shear modulus was found from [54] using structural steel (ASTM-A36): G = 77 GPa.

Mass per unit length was calculated based on section mass conservation:

$$\begin{aligned} m_l &= \rho_{wall}A_{wall} + \rho_{bore}A_{bore} \\ &= \left(7700\frac{kg}{m^3}\frac{\pi}{4}\left[0.25m^2 - 0.2116m^2\right]\right) + \left(800\frac{kg}{m^3}\frac{\pi}{4}\left[0.2116m^2\right]\right) \\ &= 135\frac{kg}{m} \end{aligned} \tag{E.10}$$

Mass per unit length was used to find average riser density:

$$\begin{aligned} \rho_r &= \frac{m_l}{A_{section}} \\ &= \frac{135\frac{kg}{m^3}}{\frac{\pi}{4}(0.25m^2)} \\ &= 2760\frac{kg}{m^3} \end{aligned} \tag{E.11}$$

Axial, flexural, and torsional rigidity was found, assuming that the riser fluid bore does not contribute to the mechanical properties:

$$\begin{aligned} EA &= 210GPa\frac{\pi}{4}\left(0.25m^2 - 0.2116m^2\right) \\ &= 2.92e9N \end{aligned} \tag{E.12}$$

$$\begin{aligned} EI &= 210GPa\frac{\pi}{4}\left(\left[\frac{0.25m}{2}\right]^4 - \left[\frac{0.2116m}{2}\right]^4\right) \\ &= 1.96e7Nm^2 \end{aligned} \tag{E.13}$$

$$\begin{aligned} GJ &= 77GPa\frac{\pi}{2}\left(\left[\frac{0.25m}{2}\right]^4 - \left[\frac{0.2116m}{2}\right]^4\right) \\ &= 1.44e7Nm^2 \end{aligned} \tag{E.14}$$

E.3 Testbed Riser System Properties

For the riser application: OD = 0.3302 m, t = 0.0127 m, L = 2000 m, $\rho_{bore} = 1.23\rho_w$. Using steel structural properties from [54]: E = 200 GPa, G = 77 GPa, $\rho_{wall} = 7860$ $\frac{kg}{m^3}$.

Average riser density was calculated based on section mass conservation:

$$\begin{aligned} m_l &= \left(7860\frac{kg}{m^3}\frac{\pi}{4}\left[0.3302m^2 - 0.3048m^2\right]\right) + \left(1260\frac{kg}{m^3}\frac{\pi}{4}\left[0.3048m^2\right]\right) \\ &= 192\frac{kg}{m} \end{aligned} \tag{E.15}$$

Mass per unit length was used to find average riser density:

$$\begin{aligned} \rho_r &= \frac{192\frac{kg}{m^3}}{\frac{\pi}{4}(0.3302m^2)} \\ &= 2236\frac{kg}{m^3} \end{aligned} \tag{E.16}$$

During the airlift section (1200m to surface) the riser mass per unit length and average riser density were found. The difference was through the riser bore slurry density: the lighter version was selected with $\rho_{bore} = 0.44\rho_w$:

$$\begin{aligned} m_l &= \left(7860\frac{kg}{m^3}\frac{\pi}{4}\left[0.3302m^2 - 0.3048m^2\right]\right) + \left(451\frac{kg}{m^3}\frac{\pi}{4}\left[0.3048m^2\right]\right) \\ &= 132\frac{kg}{m} \end{aligned} \tag{E.17}$$

$$\begin{aligned} \rho_r &= \frac{132\frac{kg}{m}}{\frac{\pi}{4}(0.3302m)^2} \\ &= 1550\frac{kg}{m^3} \end{aligned} \tag{E.18}$$

Axial, flexural, and torsional rigidity was found, assuming that the riser fluid bore does not contribute to the mechanical properties:

$$\begin{aligned} EA &= 200GPa\frac{\pi}{4}\left(0.3302m^2 - 0.3048m^2\right) \\ &= 2.53e9N \end{aligned} \tag{E.19}$$

$$\begin{aligned} EI &= 200GPa\frac{\pi}{4}\left(\left[\frac{0.3302m}{2}\right]^4 - \left[\frac{0.3048m}{2}\right]^4\right) \\ &= 3.20e7Nm^2 \end{aligned} \tag{E.20}$$

$$\begin{aligned} GJ &= 77GPa\frac{\pi}{2}\left(\left[\frac{0.3302m}{2}\right]^4 - \left[\frac{0.3048m}{2}\right]^4\right) \\ &= 2.46e7Nm^2 \end{aligned} \tag{E.21}$$

Buoyancy module diameter was set at 2D diameters and a density value of 550 $\frac{kg}{m^3}$ was used from a manufacturer website [56]. The buoyancy module, of inner diameter $2D$ and inner diameter D modifies the riser mass per unit length:

$$\begin{aligned} m_l &= 132\frac{kg}{m} + \left(550\frac{kg}{m^3}\frac{\pi}{4}\left[(2 * 0.3302m)^2 - (0.3302m)^2\right]\right) \\ &= 273\frac{kg}{m} \end{aligned} \tag{E.22}$$

It is assumed that the buoyancy module only applies the buoyancy load on the riser but does not bear any of the loadings of the riser or affect the riser stiffness. The difference in riser equivalent density is:

$$\begin{aligned} \rho_r &= \frac{253\frac{kg}{m^3}}{\frac{\pi}{4}(2 * 0.3302m)^2} \\ &= 798\frac{kg}{m^3} \end{aligned} \tag{E.23}$$

Appendix F

Maximum von Mises Stress

One method of detecting structural failure is the von Mises criterion [54]. The von Mises stress indicates the maximum stress in a single point in a structure and is calculated from knowledge of the principal stresses at that location. If the von Mises stress exceeds the tensile yield stress of the material, structural failure will follow.

Since the normal stress due to bending is maximum at the outer surface of the riser, the maximum von Mises stress was calculated on the outer surface. A unit cell under loading can be seen in figure F.1. Both bending, σ_{be}, and axial stresses due to riser tension, σ_{te}, act on the same face. Hydrostatic pressure stress, σ_p, and the resulting induced circumferential stress, σ_θ, are also applied.

Hydrostatic internal and external pressures were assumed. For a thick-walled pressure vessel, the radial and angular stress values are merely the applied hydrostatic pressure load in compression anywhere in the cross-sectional surface [41]. The stress tensor is therefore:

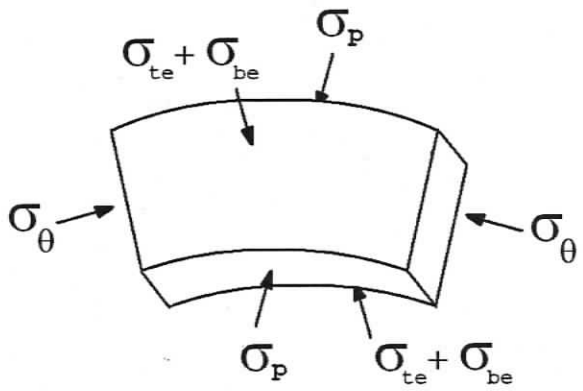

Figure F.1: Unit cell at outer rim of riser. Stresses applied are tension, σ_{te}, bending, σ_{be}, hydrostatic pressure, σ_p, and the resulting induced circumferential stress, σ_θ.

$$\sigma = \begin{bmatrix} \sigma_{be} + \sigma_{te} & 0 & 0 \\ 0 & -\sigma_p & 0 \\ 0 & 0 & -\sigma_\theta \end{bmatrix} \tag{F.1}$$

where ν is Poisson's ratio. Since no torsional loadings are present, the principal stresses, σ_a, σ_b, σ_c, are merely the diagonal terms of the stress tensor. The von Mises stress can then be evaluated from these principal stress values:

$$\sigma_{vm} = \sqrt{(\frac{1}{2}\left[(\sigma_a^2 - \sigma_b)^2 + (\sigma_b - \sigma_c)^2 + (\sigma_c - \sigma_a)^2\right])} \tag{F.2}$$